ADER-DG

-

Analysis, further Development and Applications

Dissertation
zur Erlangung des akademischen Grades
Doktor der Naturwissenschaften

der Fakultät für Geowissenschaften
der Ludwig-Maximilians-Universität München

vorgelegt von
Verena Hermann

am 14.09.2010

1. Gutachter: Prof. Dr. Heiner Igel
2. Gutachter: Prof. Dr. Valerian Bachtadse

Tag der Disputation: 12.01.2011

Abstract

After introducing the Discontinuous Galerkin (DG) method a detailed misfit analysis on its numerical approximation is performed. We investigate the accuracy of the scheme, the element type (tetrahedrons and hexahedrons), the spatial sampling of the computational domain and the number of propagated wavelengths. As the error norm we chose a time-frequency representation, which illustrates the time evolution of the spectral content. The results of this analysis are confirmed by a multi-institutional code validation project.

In order to improve efficiency, we expand the computer code to non-conforming, hybrid meshes. In 2 dimensions, triangulars and quadrilaterals can be combined within one computational domain. Several convergence tests are carried out and the newly invented scheme is applied to different test cases including thin layers and variable material.

Furthermore, as absorbing boundaries suffer from spurious reflections at artificial boundaries of the computational domain, we introduce a convolutional perfectly matched layer (CPML) to the scheme. Due to the loss of definite stability, we accomplish several test cases in order to examine the scheme's behavior. A switch-off criterion for the CPML is suggested.

Considering topographic effects on seismic waves, we perform a systematic study of different parameterizations involving the wave type and frequency of the input signal, the dataset resolution and various amplification factors of real topography in the region of Grenoble, France. Special events are simulated at Mt. Hochstaufen, Southern Bavaria, and compared to real recordings.

i

Contents

iv

Introduction

Earthquakes compose the major georisk in many parts of the world. Being not predictable to this day, they can cause large numbers of fatalities and severe economic loss every year. During the Great Sichuan Earthquake in China, e.g., which had a magnitude of $M_w = 8.0$, more than 65000 people died on 12 May 2008. Not even one year later, the 2009 L'Aquila earthquake that occurred in the region of Abruzzo, in central Italy, killed more than 300 people. The main shock happened on 6 April 2009, and was rated 6.3 on the moment magnitude scale. The probably most catastrophic earthquake during the last three years was the Haiti earthquake. With a magnitude of $M_w = 7.0$ it appeared west of Port-au-Prince, Haiti's capital, on 12 January 2010 and cost 230000 lives.

It is still impossible to forecast the point in time, when an earthquake will occur. However, the predominant locations of earthquakes, at plate boundaries, are quite clear. Hence, researchers try to estimate the effects of earthquakes as accurate as possible. The locations predicted to be most shaking should obtain earthquake resistant buildings at least if not remain unoccupied. In this field, computational seismology has become an increasingly important discipline and might become even more relevant with increasing computational resources as more realistic scenarios can be modeled. Within the last few decades a number of different numerical methods has been developed. Madariaga and Virieux [1, 2, 3] introduced the early staggered finite-difference (FD) schemes in seismology. A recent review of the developments in FD modeling is given by Moczo *et al.* [4, 5]. Furthermore, the Fourier pseudospectral (PS) methods [6, 7, 8], finite-element (FE) approaches [4, 9, 10, 11, 12], spectral element methods (SEM) [13, 14, 15, 16, 17], boundary integral equation and boundary element methods (BIEM and BEM) [18] have been developed. Rather recently, the Discontinuous Galerkin (DG) Finite-Element method has been introduced into numerical seismology [19, 20].

As each method has its advantages and disadvantages that often depend on the particular application, it is difficult, if not impossible, to decide which method is best with respect to its performance. However, it is clear that today the interpretation of synthetic seismograms typically requires a high level of confidence

and therefore numerical accuracy, where the numerical errors or artifacts do not affect true features in the seismogram due to the Earth's structure or the source properties. Therefore, the study of the accuracy of a numerical scheme is essential to evaluate its performance as well as its limits.

In this work, we perform a misfit analysis for the DG method combined with a time integration scheme using Arbitrary high-order DERivatives (ADER) as introduced recently for the simulation of seismic waves [19]. This scheme achieves high approximation orders in space and time on tetrahedral and hexahedral meshes and is based on the finite-element approach. We investigate the accuracy of the ADER-DG scheme in a way to facilitate the decisions that a modeler has to make when solving a practical problem: the desired accuracy of the synthetic seismograms, the spatial sampling of the computational domain, (i.e., the mesh spacing), the maximum propagation distance of the waves and the required approximation order of the method. The chosen error norm describes the accuracy of a synthetic seismogram quantitatively and separates amplitude and phase misfits as shown by Kristeková *et al.* [21]. We then apply the ADER-DG method to problems given online through the *Seismic wave Propagation and Imaging in Complex media: a European network* (SPICE) code validation website (www.nuquake.eu/SPICECVal).

Having analyzed the results from a misfit study the endeavor to enhance efficiency is self-evident. As the implementation of the ADER-DG method on hexahedral meshes performs faster than the one on tetrahedrons, one might conclude to use only hexahedrons in future simulations. However, the use of tetrahedrons is indispensable whenever complex geometries are included in the model. Tetrahedrons are much more flexible in discretizing complicated structures allowing us to use a coarser spatial sampling compared to hexahedrons, which in turn saves memory and runtime. Therefore, we achieve the combination of different mesh types called hybrid meshes in a similar way as it has been introduced for certain FE methods [22, 23].

Another result form the misfit analysis is, that part of the errors results from reflections at artificial boundaries. This is a well-known problem in computational seismology and many efforts have been made to overcome this inadequacy. Besides the improvement of absorbing boundary conditions, the idea of a damping layer surrounding the computational domain came up [24]. The concept of a Convolutional Perfectly Matched Layer (CPML) as we use it, was introduced by Roden and Gedney [25]. Inside the CPML, the waves decay exponentially due to a frequency-dependent damping profile in terms of a complex coordinate

stretching. Theoretically, there occur no unwanted reflections into the computational domain. However, after discretization, the CPML does not work perfectly any more. This remains an unsolved problem. Within our method, we insert an energy criterion which recognizes emerging instabilities. In such a case, we switch off the CPML and continue the computation using conventional absorbing boundary conditions.

The progression of seismic waves, starting at the hypocenter of an earthquake, propagating through the earth and finally shaking the earth's surface, depends on many parameters. For instance the material properties strongly influence the velocity and attenuation of the waves. A further topic concerning the parameterization of a simulation is the effect of topography on seismic waves. In this field many applications have been accomplished. For example Bouchon [26], Griffiths and Bollinger [27], Ma et al. [28] and Lee et al. [29] analyze areas of characteristic surface topography and find out that ground motion is highly affected by it. Amplification arises at mountain tops and ridges, whereas below steep slopes deamplification of peak ground motion prevails. In this work, we perform a systematic parameter study on topography effects for the region of Grenoble, France. We focus on frequency, dataset resolution, strength of the topographic relief and wave-type. In order to relate our results to real measurements as well, we additionally examine amplification factors of peak ground velocities in the area of Mt. Hochstaufen, Southern Bavaria, where several stations offer a number of real seismograms. Furthermore, we investigate different source mechanisms and orientations.

The work is organized as follows: First, we introduce the ADER-DG method for the 3-dimensional, elastic, homogeneous, isotropic case in Chapter 1. Chapter 2 includes the systematic error analysis as well as some applications to test cases of the code validation project suggested by SPICE. In Chapter 3 the implementation of non-conforming, hybrid meshes is performed in 2 dimensions. Here, we combine triangular with quadrangular meshes and meshes of the same type but different mesh spacing. Chapter 4 includes the theory of a CPML applied to the ADER-DG method and illustrates its advantages and disadvantages. On the one hand, we achieve great improvement for the absorption of waves at artificial boundaries for some test cases, on the other hand, we sometimes face instability problems. Last but not least, we study topographic effects on seismic waves in Chapter 5. After a systematic study for the region of Grenoble we compare simulated data for the area of Mt. Hochstaufen to real measurements. The Appendix contains

the orthogonal basis functions for all element types and the required coordinate transformations used in the ADER-DG scheme. Additionally, the equivalence of different formulations of the CPML is proven.

Chapter 1

The ADER-DG Method

1.1 Numerical Schemes for Seismic Wave Propagation

Simulations of seismic wave propagation have become a more and more appreciated tool in the recent years as modern seismology heavily relies on numerical computations. Many efforts have been made to produce highly accurate synthetic results, e.g. seismograms. Finite Difference (FD) schemes for the simulation on regular, staggered grids were introduced by Madariaga [1] and Virieux [2, 3] and further extended to higher orders ([30]), three dimensions ([31, 32]) and anisotropic material ([33, 34]). Another approach is the Pseudo-Spectral (PS) method developed by Carcione [7]. Here, the space dependent quantities are expanded in a set of orthogonal basis functions, which are known exactly and assure the computation of derivatives. Both the FD and the PS method are only convenient for Cartesian geometries. Classical Finite Element (FE) methods [35] overcome this problem as they can handle many different cell types but for real applications they need a large amount of elements and their accuracy is still limited. The Spectral Element Method (SEM) was invented by Patera (1984) for fluid mechanics, but is now also used in numerical seismology [14, 36, 37]. As this method is well suited for parallelization, it is applicable for very large-scale problems. Based on hexahedral meshes it allows for quite complex geometries but nevertheless it is still less flexible than tetrahedral discretizations.

In general, all these abovementioned methods usually have a rather low-order scheme for the time integration (second-order Newmark-type or at most fourth-

order Runge-Kutta scheme), which, of course, restricts the overall accuracy. An alternative out of this limitation is a Discontinuous Galerkin (DG) FE method using Arbitrary high-order DERivatives (ADER). It allows for very high accuracy in space and time ([38, 39, 40, 41]). Dumbser and Munz [42, 43] first developed ADER-DG schemes for linear hyperbolic systems with constant coefficients or for linear systems with variable coefficients in conservative form.

The scheme is entirely local, which means, that no large matrix inversions have to be performed and it is easy to parallelize the computational algorithms. The solutions are approximated by a polynomial within each element and updated in time. Apart from using structured meshes like quadrilaterals in 2D and hexahedrons in 3D it is possible to built the mesh with triangular or tetrahedral elements. Therefore, the meshing process can be simplified and complex geometries can easily be discretized. In contrast to FE methods discontinuities at element interfaces are allowed. This property causes the use of numerical fluxes as established in the Finite Volume (FV) framework. In this chapter, following [19, 20, 44], we first introduce the ADER-DG method for the elastic homogeneous isotropic case in order to derive and explain the scheme. We refer to tetrahedrons and hexahedrons as well and distinguish between the different element types when there arise differences. However, here we assume the discretization of the whole computational domain consisting of only one single element type.

1.2   Elastic Wave Equations - 3D

The propagation of seismic waves is governed by the theory of linear elasticity as long as linear relationships between the components of stress and strain are valid ([45, 46]). The explicit expression of the first-order elastic wave equations is a combination of Hooke's law and Newton's laws of motion. Best suited for the concept of numerical fluxes and the Cauchy-Kovalewski procedure, which are main constituents of the solving procedure, is the velocity-stress formulation of

the partial differential equation (PDE), describing elastic waves:

$$\frac{\partial}{\partial t}\sigma_{xx} - (\lambda + 2\mu)\frac{\partial}{\partial x}u - \lambda\frac{\partial}{\partial y}v - \lambda\frac{\partial}{\partial z}w = S_1,$$

$$\frac{\partial}{\partial t}\sigma_{yy} - \lambda\frac{\partial}{\partial x}u - (\lambda + 2\mu)\frac{\partial}{\partial y}v - \lambda\frac{\partial}{\partial z}w = S_2,$$

$$\frac{\partial}{\partial t}\sigma_{zz} - \lambda\frac{\partial}{\partial x}u - \lambda\frac{\partial}{\partial y}v - (\lambda + 2\mu)\frac{\partial}{\partial z}w = S_3,$$

$$\frac{\partial}{\partial t}\sigma_{xy} - \mu(\frac{\partial}{\partial x}v + \frac{\partial}{\partial y}u) = S_4,$$

$$\frac{\partial}{\partial t}\sigma_{yz} - \mu(\frac{\partial}{\partial z}v + \frac{\partial}{\partial y}w) = S_5,$$

$$\frac{\partial}{\partial t}\sigma_{xz} - \mu(\frac{\partial}{\partial x}w + \frac{\partial}{\partial z}u) = S_6,$$

$$\rho\frac{\partial}{\partial t}u - \frac{\partial}{\partial x}\sigma_{xx} - \frac{\partial}{\partial y}\sigma_{xy} - \frac{\partial}{\partial z}\sigma_{xz} = \rho S_7,$$

$$\rho\frac{\partial}{\partial t}v - \frac{\partial}{\partial x}\sigma_{xy} - \frac{\partial}{\partial y}\sigma_{yy} - \frac{\partial}{\partial z}\sigma_{yz} = \rho S_8,$$

$$\rho\frac{\partial}{\partial t}w - \frac{\partial}{\partial x}\sigma_{yz} - \frac{\partial}{\partial y}\sigma_{yz} - \frac{\partial}{\partial z}\sigma_{zz} = \rho S_9. \tag{1.1}$$

Here, the normal stress components are given by σ_{xx}, σ_{yy} and σ_{zz}, the shear stresses are expressed by σ_{ij}, with $i, j \in [x, y, z]$ and $i \neq j$. The components of the particle velocities in $x-$, $y-$ and $z-$direction are denoted by u, v and w, respectively. The space dependent material constants are ρ, μ and λ, where ρ is the density and μ and λ are the *Lamé constants*. S_i, $i = 1 \ldots 9$, describes the components of the source term with arbitrary shape in space and time.

This linear hyperbolic system of differential equations can be rewritten in matrix-vector notation,

$$\frac{\partial Q_p}{\partial t} + A_{pq}\frac{\partial Q_q}{\partial x} + B_{pq}\frac{\partial Q_q}{\partial y} + C_{pq}\frac{\partial Q_q}{\partial z} = S_p, \tag{1.2}$$

where $\mathbf{Q}$ is the vector of the p unknown variables

$$\mathbf{Q} = \{\sigma_{xx}, \sigma_{yy}, \sigma_{zz}, \sigma_{xy}, \sigma_{yz}, \sigma_{xz}, u, v, w\}^T. \tag{1.3}$$

Note, that for tensors we use bold face variable notation. Defining $\mathbf{x} = \{x, y, z\}^T$, $S_p = S_p(\mathbf{x}, t)$ is the source vector. The matrices $A_{pq} = A_{pq}(\mathbf{x})$, $B_{pq} = B_{pq}(\mathbf{x})$ and

$C_{pq} = C_{pq}(\mathbf{x})$, with $p, q = 1, \ldots, 9$, are space dependent Jacobian matrices of size 9×9, as given by

$$
\mathbf{A} = \begin{pmatrix}
0 & 0 & 0 & 0 & 0 & 0 & -(\lambda + 2\mu) & 0 & 0 \\
0 & 0 & 0 & 0 & 0 & 0 & -\lambda & 0 & 0 \\
0 & 0 & 0 & 0 & 0 & 0 & -\lambda & 0 & 0 \\
0 & 0 & 0 & 0 & 0 & 0 & 0 & -\mu & 0 \\
0 & 0 & 0 & 0 & 0 & 0 & 0 & 0 & 0 \\
0 & 0 & 0 & 0 & 0 & 0 & 0 & 0 & -\mu \\
-\frac{1}{\rho} & 0 & 0 & 0 & 0 & 0 & 0 & 0 & 0 \\
0 & 0 & 0 & -\frac{1}{\rho} & 0 & 0 & 0 & 0 & 0 \\
0 & 0 & 0 & 0 & 0 & -\frac{1}{\rho} & 0 & 0 & 0
\end{pmatrix}, \tag{1.4}
$$

$$
\mathbf{B} = \begin{pmatrix}
0 & 0 & 0 & 0 & 0 & 0 & 0 & -\lambda & 0 \\
0 & 0 & 0 & 0 & 0 & 0 & 0 & -(\lambda + 2\mu) & 0 \\
0 & 0 & 0 & 0 & 0 & 0 & 0 & -\lambda & 0 \\
0 & 0 & 0 & 0 & 0 & -\mu & 0 & 0 & 0 \\
0 & 0 & 0 & 0 & 0 & 0 & 0 & 0 & -\mu \\
0 & 0 & 0 & 0 & 0 & 0 & 0 & 0 & 0 \\
0 & 0 & 0 & -\frac{1}{\rho} & 0 & 0 & 0 & 0 & 0 \\
0 & -\frac{1}{\rho} & 0 & 0 & 0 & 0 & 0 & 0 & 0 \\
0 & 0 & 0 & 0 & -\frac{1}{\rho} & 0 & 0 & 0 & 0
\end{pmatrix}, \tag{1.5}
$$

$$
\mathbf{C} = \begin{pmatrix}
0 & 0 & 0 & 0 & 0 & 0 & 0 & 0 & -\lambda \\
0 & 0 & 0 & 0 & 0 & 0 & 0 & 0 & -\lambda \\
0 & 0 & 0 & 0 & 0 & 0 & 0 & 0 & -(\lambda + 2\mu) \\
0 & 0 & 0 & 0 & 0 & 0 & 0 & 0 & 0 \\
0 & 0 & 0 & 0 & 0 & 0 & 0 & -\mu & 0 \\
0 & 0 & 0 & 0 & 0 & 0 & -\mu & 0 & 0 \\
0 & 0 & 0 & 0 & 0 & -\frac{1}{\rho} & 0 & 0 & 0 \\
0 & 0 & 0 & 0 & -\frac{1}{\rho} & 0 & 0 & 0 & 0 \\
0 & 0 & -\frac{1}{\rho} & 0 & 0 & 0 & 0 & 0 & 0
\end{pmatrix}. \tag{1.6}
$$

Note, that we are using classical tensor notation, which implies summation over each index appearing twice within one term.

As the PDE (1.2) is hyperbolic, the matrices all have real eigenvalues,

$$
\begin{aligned}
\alpha_1 &= -c_p, & \alpha_2 &= -c_s, & \alpha_3 &= -c_s, \\
\alpha_4 &= 0, & \alpha_5 &= 0, & \alpha_6 &= 0, \\
\alpha_7 &= c_s, & \alpha_8 &= c_s, & \alpha_9 &= c_p,
\end{aligned} \tag{1.7}
$$

with

$$c_p = \sqrt{\frac{\lambda + 2\mu}{\rho}} \quad \text{and} \quad c_s = \sqrt{\frac{\mu}{\rho}}. \tag{1.8}$$

The eigenvalues reflect the wave velocities of the wave propagation which are given by the eigenvectors $R_{p1}^A \dots R_{p9}^A$ (here computed for matrix A)

$$\mathbf{R}^A = \begin{pmatrix} \lambda + 2\mu & 0 & 0 & 0 & 0 & 0 & 0 & 0 & \lambda + 2\mu \\ \lambda & 0 & 0 & 0 & 1 & 0 & 0 & 0 & \lambda \\ \lambda & 0 & 0 & 0 & 0 & 1 & 0 & 0 & \lambda \\ 0 & \mu & 0 & 0 & 0 & 0 & 0 & \mu & 0 \\ 0 & 0 & 0 & 1 & 0 & 0 & 0 & 0 & 0 \\ 0 & 0 & \mu & 0 & 0 & 0 & \mu & 0 & 0 \\ c_p & 0 & 0 & 0 & 0 & 0 & 0 & 0 & -c_p \\ 0 & c_s & 0 & 0 & 0 & 0 & 0 & -c_s & 0 \\ 0 & 0 & c_s & 0 & 0 & 0 & -c_s & 0 & 0 \end{pmatrix}. \tag{1.9}$$

c_p is called the P-wave velocity and c_s the S-wave velocity.

1.3 The Numerical Scheme of the ADER-DG Method

For the construction of the numerical scheme of the ADER-DG method we divide the computational domain $\Omega \in \mathbb{R}^3$ into conforming elements being addressed by the superscript (m). Each element $\mathcal{E}^{(m)}$ is specified uniquely by its n vertices $\mathbf{x}_1, \dots, \mathbf{x}_n$, with $\mathbf{x}_i = (x_i, y_i, z_i)$ and $i = 1, \dots, n$. For tetrahedrons $n = 4$ whereas for hexahedrons $n = 8$ vertices depict one element. The reference tetrahedron $\mathcal{E}_{ref}$ is defined by the points $\mathbf{x}_1 = (0,0,0)$, $\mathbf{x}_2 = (1,0,0)$, $\mathbf{x}_3 = (0,1,0)$ and $\mathbf{x}_4 = (0,0,1)$ in a local coordinate system denoted by ξ, η and ζ. For hexahedrons the reference element (here also called $\mathcal{E}_{ref}$) is built up by the vertices $\mathbf{x}_1 = (0,0,0)$, $\mathbf{x}_2 = (1,0,0)$, $\mathbf{x}_3 = (0,1,0)$, $\mathbf{x}_4 = (1,1,0)$, $\mathbf{x}_5 = (0,0,1)$, $\mathbf{x}_6 = (1,0,1)$, $\mathbf{x}_7 = (0,1,1)$ and $\mathbf{x}_8 = (1,1,1)$.

In the following, we derive the numerical solution of the elastic wave equation using the ADER-DG method. First we will generate the spatial approach (Discontinuous Galerkin method) and afterwards we will go into the details of the ADER time-discretization according to [20].
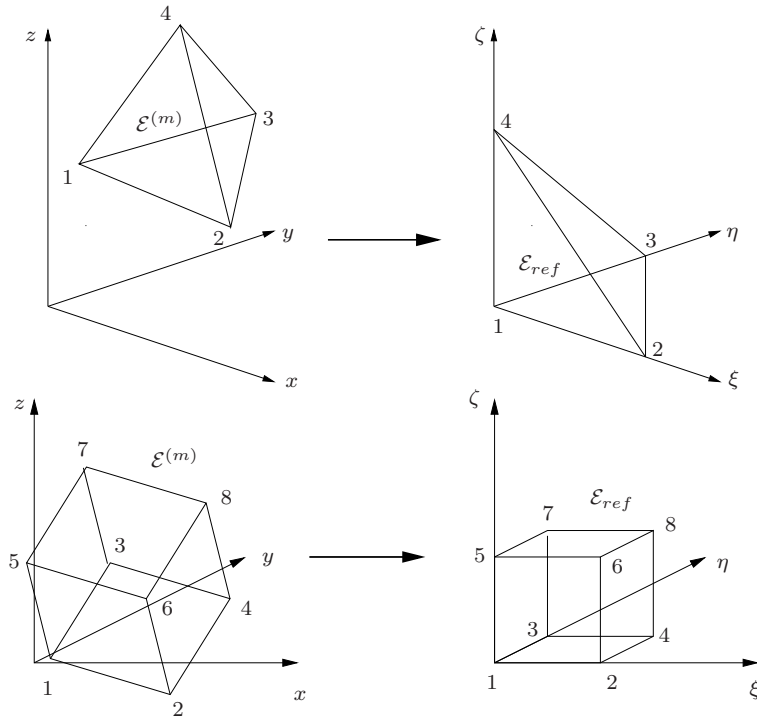
Figure 1.1: *Transformation of an element in the global coordinate system to the reference element in the local coordinate system.*

1.3.1   Basis Functions

Inside each element the solution of Eq. (1.2) is approximated numerically by $\mathbf{Q}_h$ which is a linear combination of purely space-dependent polynomial basis functions $\Phi_l(\xi, \eta, \zeta)$ of degree N and purely time-dependent degrees of freedom $\hat{Q}_{pl}^{(m)}(t)$:

$$\left(Q_h^{(m)}\right)_p (\xi, \eta, \zeta, t) = \hat{Q}_{pl}^{(m)}(t)\,\Phi_l(\xi, \eta, \zeta)\,. \tag{1.10}$$

For the ADER-DG scheme we exploit the *Dubiner's basis functions* presented in [47]. For a fixed polynomial degree N the required number of orthogonal basis functions is $L = (N+1)(N+2)(N+3)/6$. A more detailed discussion of this basis is given in App. A.

The basis functions are supported by the reference element $\mathcal{E}_{ref}$ with the local $\xi\eta\zeta$-coordinate system. Any point inside each element can be mapped to this Cartesian coordinate system via the transformation given in App. B (see also Fig. 1.1).

Momentarily, we use the same notation for tetrahedrons and hexahedrons although the basis functions are not equal. As soon as it becomes decisive to distinguish between the element types we will introduce new variables.

As an example, Figs. 1.2 and 1.3 show the first 6 Dubiner's basis functions for triangles and quadrilaterals in two dimensions, where the number of basis functions is given by $L = (N + 1)(N + 2)/2$. Therefore, we achieve a polynomial approximation of degree $N = 2$ with this set of basis functions.

In general, the approximated scalar function f_h of any arbitrary exact function f can be represented as the linear combination

$$f_h = \hat{f}_i \Phi_i, \tag{1.11}$$

with the coefficients $\hat{f}_i$ obtained from the projection

$$\hat{f}_i = \frac{\int\limits_{\mathcal{E}_{ref}} f\, \Phi_j \mathrm{d}V}{\int\limits_{\mathcal{E}_{ref}} \Phi_i \Phi_j \mathrm{d}V}. \tag{1.12}$$

1.3.2 Godunov Fluxes

The first step in solving the elastic wave equation is multiplying the differential equation (1.2) by a testfunction Φ_k and integrating over one element $\mathcal{E}^{(m)}$:

$$\int\limits_{\mathcal{E}^{(m)}} \Phi_k \frac{\partial Q_p}{\partial t}\, \mathrm{d}V + \int\limits_{\mathcal{E}^{(m)}} \Phi_k \left(A_{pq} \frac{\partial Q_q}{\partial x} + B_{pq} \frac{\partial Q_q}{\partial y} + C_{pq} \frac{\partial Q_q}{\partial z} \right) \mathrm{d}V = \int\limits_{\mathcal{E}^{(m)}} \Phi_k S_p\, \mathrm{d}V. \tag{1.13}$$

The second term of Eq. (1.13) can be integrated by parts:

$$\int\limits_{\mathcal{E}^{(m)}} \Phi_k \left(A_{pq} \frac{\partial Q_q}{\partial x} + B_{pq} \frac{\partial Q_q}{\partial y} + C_{pq} \frac{\partial Q_q}{\partial z} \right) \mathrm{d}V = \tag{1.14}$$

$$\int\limits_{\mathcal{E}^{(m)}} \nabla \left[\Phi_k \left(A_{pq} \hat{x} + B_{pq} \hat{y} + C_{pq} \hat{z} \right) \right] Q_q\, \mathrm{d}V - \int\limits_{\mathcal{E}^{(m)}} \left(\nabla \Phi_k \right) \left(A_{pq} \hat{x} + B_{pq} \hat{y} + C_{pq} \hat{z} \right) Q_q\, \mathrm{d}V,$$

where $\hat{x}, \hat{y}, \hat{z}$ denote the normal vectors in $x-, y-$ and $z-$direction. Now, the first part of Eq. (1.14) can be reformulated using Gauss' theorem

$$\int\limits_{\mathcal{E}^{(m)}} \nabla \left[\Phi_k \left(A_{pq} \hat{x} + B_{pq} \hat{y} + C_{pq} \hat{z} \right) \right] Q_q\, \mathrm{d}V = \int\limits_{\partial \mathcal{E}^{(m)}} \Phi_k F_p^h\, \mathrm{d}S, \tag{1.15}$$
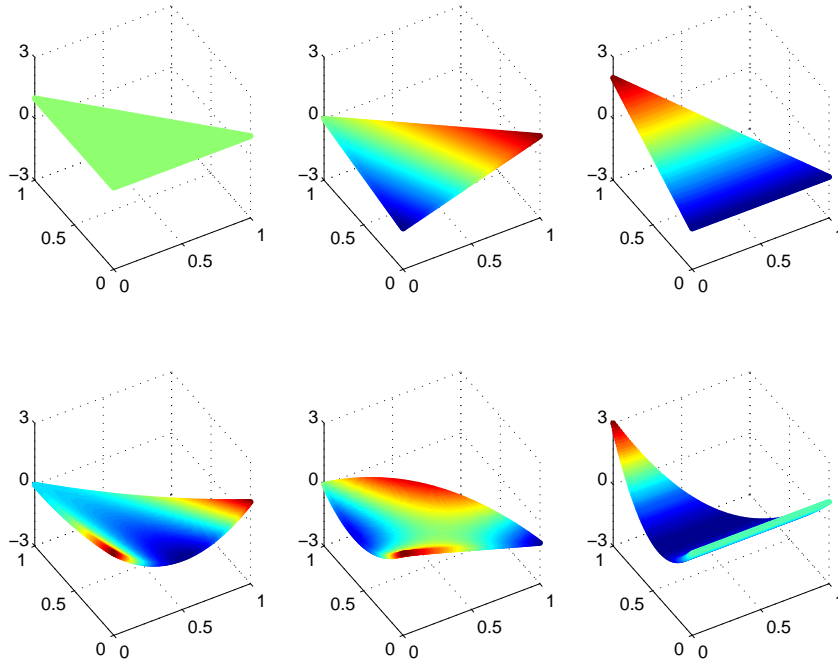
Figure 1.2: *The Dubiner's basis functions ($N = 2$) for triangles in two dimensions.*
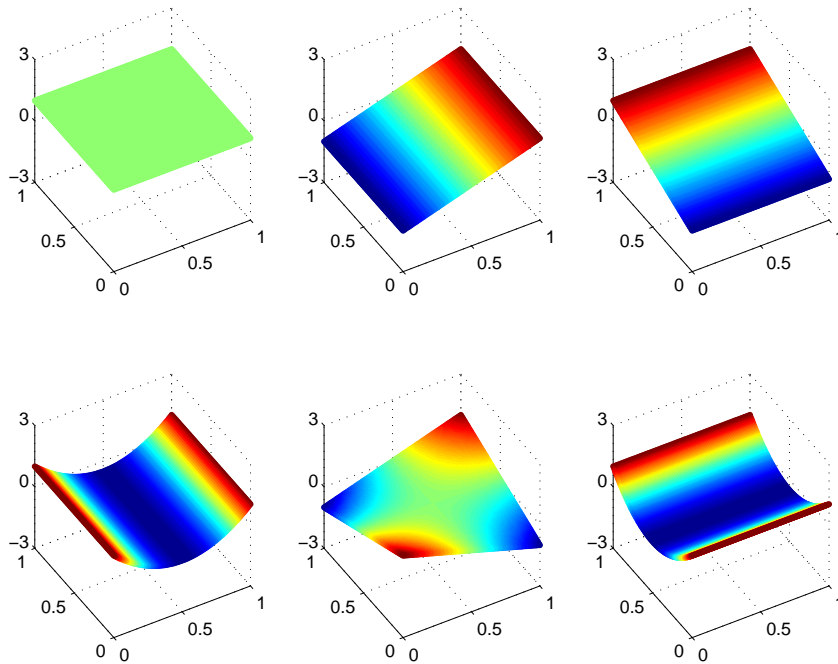

Figure 1.3: *The Dubiner's basis functions ($N = 2$) for quadrilaterals in two dimensions.*
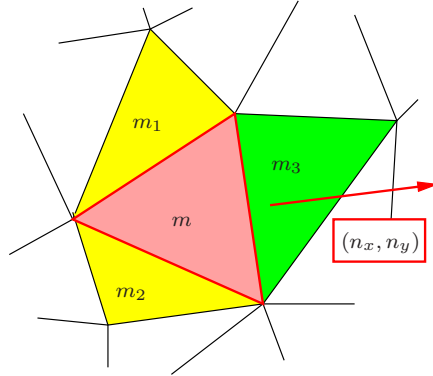
Figure 1.4: *Illustration for the flux computation in 2D. The element m only communicates with its direct neighbors m_1, m_2 and m_3. The flux integral can be decomposed into a sum of integrals over the edges of the elements. For an edge-aligned coordinate system, where (n_x, n_y) denotes the normal vector, the flux terms can be computed easily.*

with the numerical flux $F_p^h = (A_{pq}\hat{x} + B_{pq}\hat{y} + C_{pq}\hat{z}) Q_q \, \mathbf{n}$, which has to be computed perpendicular to the surface. The surface integral can be decomposed into a sum of integrals over the element faces like it is illustrated in Fig. 1.4. Therewith, F_p^h for one interface between element (m) and its neighbor element (m_j) can be written as

$$
\begin{aligned}
F_p^h &= \frac{1}{2} T_{pq} \left(A_{qr}^{(m)} + |A_{qr}^{(m)}| \right) (T_{rs})^{-1} Q_s^{(m)} \\
&+ \frac{1}{2} T_{pq} \left(A_{qr}^{(m)} - |A_{qr}^{(m)}| \right) (T_{rs})^{-1} Q_s^{(m_j)} .
\end{aligned}
\tag{1.16}
$$

Here, T_{pq} denotes the transformation matrix which allows for the rotation from the global Cartesian coordinate system to a face-aligned, local normal one. With $\mathbf{n} = (n_x, n_y, n_z)^T$ being the normal vector and $\mathbf{s} = (s_x, s_y, s_z)^T$ and $\mathbf{t} = (t_x, t_y, t_z)^T$ representing the two tangential vectors with respect to one face of the element, $\mathbf{T}$ reads

$$
\mathbf{T} = \begin{pmatrix} \mathbf{T}^{(1)} & \mathbf{0} \\ \mathbf{0} & \mathbf{T}^{(2)} \end{pmatrix} ,
\tag{1.17}
$$

with

$$\mathbf{T}^{(1)} = \begin{pmatrix} n_x^2 & s_x^2 & t_x^2 & 2n_x s_x & 2s_x t_x & 2t_x n_x \\ n_y^2 & s_y^2 & t_y^2 & 2n_y s_y & 2s_y t_y & 2t_y n_y \\ n_z^2 & s_z^2 & t_z^2 & 2n_z s_z & 2s_z t_z & 2t_z n_z \\ n_x n_y & s_x s_y & t_x t_y & n_x s_y + n_y s_x & s_x t_y + s_y t_x & t_x n_y + t_y n_x \\ n_y n_z & s_y s_z & t_y t_z & n_y s_z + n_z s_y & s_y t_z + s_z t_y & t_y n_z + t_z n_y \\ n_z n_x & s_z s_x & t_z t_x & n_z s_x + n_x s_z & s_z t_x + s_x t_z & t_z n_x + t_x n_z \end{pmatrix} \qquad (1.18)$$

and

$$\mathbf{T}^{(2)} = \begin{pmatrix} n_x & s_x & t_x \\ n_y & s_y & t_y \\ n_z & s_z & t_z \end{pmatrix} . \qquad (1.19)$$

The numerical flux F_p^h has been introduced in the surface integral because the solution Q_h may be discontinuous at element boundaries. It should be mentioned that both boundary values of the two elements adjacent to the interface contribute. From the theory of numerical fluxes [48] we know that if any discontinuity exists at a surface, it will generate a number of waves given by the amount of eigenvectors and eigenvalues associated with the Jacobian matrix A of the system (presented in Sec. 1.2). To summarize, for every boundary face of any element we need to consider the outgoing as well as the incoming flux at which we have to make sure that only those waves contribute which have the right direction of travel (positive normal direction for outgoing and resp. negative direction for incoming fluxes). To accommodate this feature we define the absolute value of the Jacobian matrix $\mathbf{A}$ as

$$|A_{qr}| = R_{qp}^A |\Lambda_{ps}| (R_{sr}^A)^{-1}, \quad \text{with} \quad |\Lambda_{ps}| = \text{diag}(|\alpha_1|, |\alpha_2|, \dots). \qquad (1.20)$$

Therewith, the correct outgoing flux is given by the first term of Eq. (1.16) and the incoming flux is given by its second term. This flux type, where the eigen-decomposition of the system is used to solve the fluxes, is called the upwinding exact Riemann solver or *Godunov* flux.

Going back to Eq. (1.13), we can comprise Eq. (1.10) and represent the source-term S_p in a space-time dependent basis which is given by the already introduced spatial basis functions $\Phi_l(\xi, \eta, \zeta)$ and some new temporal basis functions $\Psi_m(t)$ which are classical Legendre polynomials in the interval of one timestep. Thus, the time-dependent degrees of freedom can be extracted from the integrals.

The semi-discrete DG formulation of Eq. (1.13) reads

$$
\frac{\partial}{\partial t}\hat{Q}_{pl}^{(m)} \int_{\mathcal{E}^{(m)}} \Phi_k \Phi_l \, \mathrm{d}V
$$

$$
+ \sum_{j=1}^{s} \frac{1}{2} T_{pq}^{(j)} \left(A_{qr}^{(m)} + |A_{qr}^{(m)}| \right) (T_{rs}^{(j)})^{-1} \hat{Q}_{sl}^{(m)} \int_{\partial \mathcal{E}_j^{(m)}} \Phi_k^{(m)} \Phi_l^{(m)} \, \mathrm{d}S
$$

$$
+ \sum_{j=1}^{s} \frac{1}{2} T_{pq}^{(j)} \left(A_{qr}^{(m)} - |A_{qr}^{(m)}| \right) (T_{rs}^{(j)})^{-1} \hat{Q}_{sl}^{(m_j)} \int_{\partial \mathcal{E}_j^{(m)}} \Phi_k^{(m)} \Phi_l^{(m_j)} \, \mathrm{d}S
$$

$$
- A_{pq}\hat{Q}_{ql}^{(m)} \int_{\mathcal{E}^{(m)}} \frac{\partial \Phi_k}{\partial x}\Phi_l \, \mathrm{d}V - B_{pq}\hat{Q}_{ql}^{(m)} \int_{\mathcal{E}^{(m)}} \frac{\partial \Phi_k}{\partial y}\Phi_l \, \mathrm{d}V - C_{pq}\hat{Q}_{ql}^{(m)} \int_{\mathcal{E}^{(m)}} \frac{\partial \Phi_k}{\partial z}\Phi_l \, \mathrm{d}V
$$

$$
= \hat{S}_{plm}\Psi_m \int_{\mathcal{E}^{(m)}} \Phi_k \Phi_l \, \mathrm{d}V \, . \tag{1.21}
$$

As already announced, the surface integral over the fluxes is split into s parts referring to the s sides of the element ($s = 4$ for tetrahedrons, $s = 6$ for hexahedrons). Every part appears once for the element $\mathcal{E}^{(m)}$ itself and once for the corresponding face of its neighbor element $\mathcal{E}^{(m_j)}$ to also allow for the incoming flux.

Note, that we still integrate over the volume of one physical element $\mathcal{E}^{(m)}$ and build the derivatives in the global coordinate system, whereas the basis functions live in the reference system. Hence, we have to decide in which system we want to do the integration and transform the according variables.

1.3.3 Coordinate Transformation

In oder to keep the computational cost as low as possible, it is helpful to use tabulated values in spite of recomputing terms. Therefore, we perform a transformation of each element to the reference element (see Sec. 1.3.1 and App. B). In this way, many integrals can be precomputed and the method is implemented more efficiently.

The transformation affects the integration variables

$$
\mathrm{d}x\mathrm{d}y\mathrm{d}z = |\mathbf{J}|\mathrm{d}\xi\mathrm{d}\eta\mathrm{d}\zeta \, , \tag{1.22}
$$

where $|\mathbf{J}|$ is the determinant of the Jacobian matrix of the transformation given in App. B, Eq. (B.8) and (B.11), and the gradients comply with

$$
\begin{pmatrix} \frac{\partial}{\partial x} \\ \frac{\partial}{\partial y} \\ \frac{\partial}{\partial z} \end{pmatrix} = \begin{pmatrix} \frac{\partial \xi}{\partial x} & \frac{\partial \eta}{\partial x} & \frac{\partial \zeta}{\partial x} \\ \frac{\partial \xi}{\partial y} & \frac{\partial \eta}{\partial y} & \frac{\partial \zeta}{\partial y} \\ \frac{\partial \xi}{\partial z} & \frac{\partial \eta}{\partial z} & \frac{\partial \zeta}{\partial z} \end{pmatrix} \begin{pmatrix} \frac{\partial}{\partial \xi} \\ \frac{\partial}{\partial \eta} \\ \frac{\partial}{\partial \zeta} \end{pmatrix} .
\tag{1.23}
$$

Before we accomplish the transformation of Eq. (1.21), we define:

$$
A^*_{pq} = A_{pq} \frac{\partial \xi}{\partial x} + B_{pq} \frac{\partial \xi}{\partial y} + C_{pq} \frac{\partial \xi}{\partial z} ,
$$

$$
B^*_{pq} = A_{pq} \frac{\partial \eta}{\partial x} + B_{pq} \frac{\partial \eta}{\partial y} + C_{pq} \frac{\partial \eta}{\partial z} ,
$$

$$
C^*_{pq} = A_{pq} \frac{\partial \zeta}{\partial x} + B_{pq} \frac{\partial \zeta}{\partial y} + C_{pq} \frac{\partial \zeta}{\partial z} .
\tag{1.24}
$$

Therewith, the semi-discrete DG formulation of Eq. (1.21) transforms to

$$
\frac{\partial}{\partial t} \hat{Q}^{(m)}_{pl} |\mathbf{J}| \int_{\mathcal{E}_{ref}} \Phi_k \Phi_l \, \mathrm{d}\xi \, \mathrm{d}\eta \, \mathrm{d}\zeta
$$

$$
+ \quad \sum_{j=1}^{s} \frac{1}{2} T^{(j)}_{pq} \left(A^{(m)}_{qr} + |A^{(m)}_{qr}| \right) (T^{(j)}_{rs})^{-1} \hat{Q}^{(m)}_{sl} \int_{\partial \mathcal{E}^{(m)}_j} \Phi^{(m)}_k \Phi^{(m)}_l \, \mathrm{d}S
$$

$$
+ \quad \sum_{j=1}^{s} \frac{1}{2} T^{(j)}_{pq} \left(A^{(m)}_{qr} - |A^{(m)}_{qr}| \right) (T^{(j)}_{rs})^{-1} \hat{Q}^{(m_j)}_{sl} \int_{\partial \mathcal{E}^{(m)}_j} \Phi^{(m)}_k \Phi^{(m_j)}_l \, \mathrm{d}S
$$

$$
- \quad A^*_{pq} \hat{Q}^{(m)}_{ql} |\mathbf{J}| \int_{\mathcal{E}_{ref}} \frac{\partial \Phi_k}{\partial \xi} \Phi_l \, \mathrm{d}\xi \, \mathrm{d}\eta \, \mathrm{d}\zeta
$$

$$
- \quad B^*_{pq} \hat{Q}^{(m)}_{ql} |\mathbf{J}| \int_{\mathcal{E}_{ref}} \frac{\partial \Phi_k}{\partial \eta} \Phi_l \, \mathrm{d}\xi \, \mathrm{d}\eta \, \mathrm{d}\zeta
$$

$$
- \quad C^*_{pq} \hat{Q}^{(m)}_{ql} |\mathbf{J}| \int_{\mathcal{E}_{ref}} \frac{\partial \Phi_k}{\partial \zeta} \Phi_l \, \mathrm{d}\xi \, \mathrm{d}\eta \, \mathrm{d}\zeta
$$

$$
= \quad \hat{S}_{plm} \Psi_m |\mathbf{J}| \int_{\mathcal{E}_{ref}} \Phi_k \Phi_l \, \mathrm{d}\xi \, \mathrm{d}\eta \, \mathrm{d}\zeta .
\tag{1.25}
$$

Obviously, the integrals

$$M_{kl} = \int_{\mathcal{E}_{ref}} \Phi_k \Phi_l \, \mathrm{d}\xi \, \mathrm{d}\eta \, \mathrm{d}\zeta \,,$$

$$K_{kl}^{\xi} = \int_{\mathcal{E}_{ref}} \frac{\partial \Phi_k}{\partial \xi} \Phi_l \, \mathrm{d}\xi \, \mathrm{d}\eta \, \mathrm{d}\zeta \,,$$

$$K_{kl}^{\eta} = \int_{\mathcal{E}_{ref}} \frac{\partial \Phi_k}{\partial \eta} \Phi_l \, \mathrm{d}\xi \, \mathrm{d}\eta \, \mathrm{d}\zeta \,,$$

$$K_{kl}^{\zeta} = \int_{\mathcal{E}_{ref}} \frac{\partial \Phi_k}{\partial \zeta} \Phi_l \, \mathrm{d}\xi \, \mathrm{d}\eta \, \mathrm{d}\zeta \,, \tag{1.26}$$

can be precomputed and tabulated. Only the surface integrals still refer to physical space. Denoting $|\mathbf{S}^{(j)}|$ the Jacobian of side j, the integrals appearing in the flux terms reduce to

$$\int_{\partial \mathcal{E}_j^{(m)}} \Phi_k^{(m)} \Phi_l^{(m)} \, \mathrm{d}S = |\mathbf{S}^{(j)}| F_{kl}^{-,(j)} \quad \text{and} \quad \int_{\partial \mathcal{E}_j^{(m)}} \Phi_k^{(m)} \Phi_l^{(m_j)} \, \mathrm{d}S = |\mathbf{S}^{(j)}| F_{kl}^{+,(j,i,h)} \,.$$

$$\tag{1.27}$$

Now, the flux matrices $F_{kl}^{-,(j)}$ and $F_{kl}^{+,(j,i,h)}$ can be calculated analytically once on the reference element and then be stored.

In the following, we give the details of evaluating these flux matrices on tetrahedrons and hexahedrons. First, we define the local faces with their local vertex ordering according to Tab. 1.1, where the vertex numbering is strictly counter-clockwise (see Fig. 1.1). The vector of volume coordinates $\boldsymbol{\xi}$ is then given on the faces via mapping functions from the face parameters χ and τ, as shown in Tab. 1.2.

Last but not least, for the flux computation over the face, we have to integrate along the face inside the element itself as well as inside the adjacent element. The latter is obtained by the transformation from the face parameters χ and τ inside the element to the corresponding face parameters $\tilde{\chi}$ and $\tilde{\tau}$ of the neighbor's face. Whereas in two space dimensions this transformation is always $\tilde{\chi} = 1 - \chi$, in three space dimensions the transformation depends on the orientation of the neighbor's face with respect to the local face of the considered

Face	Vertices			
1	1	2	6	5
2	2	4	8	6
3	4	3	7	8
4	3	1	5	7
5	2	1	3	4
6	5	6	8	7

(a)

Face	Vertices		
1	1	3	2
2	1	2	4
3	1	4	3
4	2	3	4

(b)

Table 1.1: *Face definition on (a) hexahedrons and (b) tetrahedrons.*

element $\mathcal{E}^{(m)}$, since via rotation of the quadrilateral faces there may be four and via rotation of the triangular faces there may be three possible orientations. The mappings are given in Tab. 1.3.

All possible flux matrices are given by

$$
F_{kl}^{+,(j,i,h)} = \int_{\partial(\mathcal{E}_{ref})_j} \Phi_k\left(\boldsymbol{\xi}^{(j)}(\chi,\tau)\right) \Phi_l\left(\boldsymbol{\xi}^{(i)}\left(\tilde{\chi}^{(h)}(\chi,\tau), \tilde{\tau}^{(h)}(\chi,\tau)\right)\right) \mathrm{d}\chi\,\mathrm{d}\tau\,,
$$

$$
F_{kl}^{-,(j)} = \int_{\partial(\mathcal{E}_{ref})_j} \Phi_k\left(\boldsymbol{\xi}^{(j)}(\chi,\tau)\right) \Phi_l\left(\boldsymbol{\xi}^{(j)}(\chi,\tau)\right) \mathrm{d}\chi\,\mathrm{d}\tau\,, \tag{1.28}
$$

for $1 \leqq j \leqq s$, $1 \leqq i \leqq s$, $1 \leqq h \leqq v$. Index i indicates the local number of the common face as it is seen from the neighbor (m_j) and depends on the mesh generator. Index h denotes the number of the local node in the neighbors face ($v = 3$ for tetrahedrons, $v = 4$ for hexahedrons) which lies on the local vertex 1 of face j in tetrahedron number (m). It also depends on the mesh generator. On a given mesh, where indices i and h are known, only s of the $s \cdot s \cdot v$ considered matrices $F_{kl}^{+,(j,i,h)}$ are used per element.

j	1	2	3	4
$\xi^{(j)}(\chi,\tau)$	τ	χ	0	$1-\chi-\tau$
$\eta^{(j)}(\chi,\tau)$	χ	0	τ	χ
$\zeta^{(j)}(\chi,\tau)$	0	τ	χ	τ

(a)

j	1	2	3	4	5	6
$\xi^{(j)}(\chi,\tau)$	χ	0	τ	0	τ	χ
$\eta^{(j)}(\chi,\tau)$	0	χ	0	τ	χ	τ
$\zeta^{(j)}(\chi,\tau)$	τ	τ	χ	χ	0	0

(b)

Table 1.2: *3-D volume coordinates $\boldsymbol{\xi}^{(j)}$ as a function of the face parameters χ and τ for the faces j of tetrahedrons (a) and hexahedrons (b).*

Concluding, we can rewrite the semi-discrete equation

$$\frac{\partial}{\partial t}\hat{Q}_{pl}^{(m)}|\mathbf{J}|M_{kl}$$

$$+ \quad \sum_{j=1}^{s}\frac{1}{2}T_{qp}^{(j)}\left(A_{qr}^{(m)}+|A_{qr}^{(m)}|\right)(T_{rs}^{(j)})^{-1}\hat{Q}_{sl}^{(m)}|\mathbf{S}^{(j)}|F_{kl}^{-,(j)}$$

$$+ \quad \sum_{j=1}^{s}\frac{1}{2}T_{qp}^{(j)}\left(A_{qr}^{(m)}-|A_{qr}^{(m)}|\right)(T_{rs}^{(j)})^{-1}\hat{Q}_{sl}^{(m_j)}|\mathbf{S}^{(j)}|F_{kl}^{+,(j,i,h)}$$

$$- \quad \hat{Q}_{ql}^{(m)}|\mathbf{J}|\left(A_{pq}^{*}K_{kl}^{\xi}+B_{pq}^{*}K_{kl}^{\eta}+C_{pq}^{*}K_{kl}^{\zeta}\right)$$

$$= \quad \hat{S}_{plm}\Psi_m|\mathbf{J}|M_{kl}\,, \tag{1.29}$$

which can be integrated in time.

1.3.4   The ADER Time-Discretization

The great benefit of the ADER approach is that it achieves the same accuracy for the time-discretization as for the space-discretization. The main ingredients of

h	1	2	3
$\tilde{\chi}^{(h)}(\chi, \tau)$	τ	$1 - \chi - \tau$	χ
$\tilde{\tau}^{(h)}(\chi, \tau)$	χ	τ	$1 - \chi - \tau$

(a)

h	1	2	3	4
$\tilde{\chi}^{(h)}(\chi, \tau)$	τ	χ	τ	χ
$\tilde{\tau}^{(h)}(\chi, \tau)$	χ	τ	χ	τ

(b)

Table 1.3: *Transformation of the face parameters $\tilde{\chi}$ and $\tilde{\tau}$ in the neighbor element according to the possible orientations h of the neighbor's face for tetrahedrons (a) and hexahedrons (b).*

its derivation are a Taylor expansion in time, the solution of Derivative Riemann Problems [49] to approximate the space derivatives at element interfaces and the Cauchy-Kovalewski procedure which will be discussed in detail below.

To obtain the complete solution of Eq. (1.2) we still need to integrate Q_p, the vector of unknown variables, in time. Regarding Eq. (1.10), it is sufficient to only comprise the degrees of freedom $\hat{Q}_{pl}(t)$. Numerically, the time-integral is decomposed into small timesteps of size Δt and then accomplished piecewise from step t_n to $t_{n+1} = t_n + \Delta t$.
First, $\hat{Q}_{pl}$ is Taylor expanded in time, which reads

$$\hat{Q}_{pl}(t_n + \tau) = \hat{Q}_{pl}(t_n) + \frac{\partial}{\partial t}\hat{Q}_{pl}(t_n)\,\tau + \frac{1}{2}\frac{\partial^2}{\partial t^2}\hat{Q}_{pl}(t_n)\,\tau^2 + \dots \qquad (1.30)$$

and therewith the polynomial of degree N is given by

$$\hat{Q}_{pl}(t_n + \tau) = \sum_{k=0}^{N} \frac{\tau^k}{k!}\frac{\partial^k}{\partial t^k}\hat{Q}_{pl}(t_n)\,. \qquad (1.31)$$

Integrating over one timestep Δt leads to

$$
\int_{t_n}^{t_n+\Delta t} \hat{Q}_{pl}(t_n + \tau)\mathrm{d}\tau = \left[\sum_{k=0}^{N} \frac{\tau^{k+1}}{(k+1)!} \frac{\partial^k}{\partial t^k} \hat{Q}_{pl}(t_n) \right]_{t_n}^{t_n+\Delta t}
$$

$$
= \sum_{k=0}^{N} \frac{\Delta t^{k+1}}{(k+1)!} \frac{\partial^k}{\partial t^k} \hat{Q}_{pl}(t_n) \,. \tag{1.32}
$$

Note, that this integration can be accomplished comprising an Arbitrary high order of DERivatives and thus it is called the ADER-approach. The ADER time-integration follows the technique of Lax-Wendroff, where the time-derivative is replaced by pure space derivatives from the governing PDE (1.2). Extended to a recursive formula for higher-order derivatives this procedure is often referred to as the Cauchy-Kovalewski procedure. Since the basis functions are given in the reference element, we use the $\xi\eta\zeta$-reference system. Thus, we transform the governing equation to

$$
\frac{\partial Q_p}{\partial t} + A_{pq} \left(\frac{\partial \xi}{\partial x} \frac{\partial Q_q}{\partial \xi} + \frac{\partial \eta}{\partial x} \frac{\partial Q_q}{\partial \eta} + \frac{\partial \zeta}{\partial x} \frac{\partial Q_q}{\partial \zeta} \right)
$$

$$
+ B_{pq} \left(\frac{\partial \xi}{\partial y} \frac{\partial Q_q}{\partial \xi} + \frac{\partial \eta}{\partial y} \frac{\partial Q_q}{\partial \eta} + \frac{\partial \zeta}{\partial y} \frac{\partial Q_q}{\partial \zeta} \right)
$$

$$
+ C_{pq} \left(\frac{\partial \xi}{\partial z} \frac{\partial Q_q}{\partial \xi} + \frac{\partial \eta}{\partial z} \frac{\partial Q_q}{\partial \eta} + \frac{\partial \zeta}{\partial z} \frac{\partial Q_q}{\partial \zeta} \right) = S_p \,, \tag{1.33}
$$

using the transformation directive given in Eq. (1.23). We rearrange the terms of this equation and use the definition of Eq. (1.24) to get

$$
\frac{\partial Q_p}{\partial t} = S_p - A_{pq}^* \frac{\partial Q_q}{\partial \xi} - B_{pq}^* \frac{\partial Q_q}{\partial \eta} - C_{pq}^* \frac{\partial Q_q}{\partial \zeta} \,. \tag{1.34}
$$

Multiplying Eq. (1.34) by a test function Φ_k, integrating over the reference ele-

ment and introducing the polynomial approximation of Eq. (1.10), we obtain

$$
\frac{\partial \hat{Q}_{pl}}{\partial t} \int_{\mathcal{E}_{ref}} \Phi_k \Phi_l \, \mathrm{d}\xi \, \mathrm{d}\eta \, \mathrm{d}\zeta = \hat{S}_{plm} \Psi_m \int_{\mathcal{E}_{ref}} \Phi_k \Phi_l \, \mathrm{d}\xi \, \mathrm{d}\eta \, \mathrm{d}\zeta
$$

$$
- A^*_{pq} \hat{Q}_{ql} \int_{\mathcal{E}_{ref}} \frac{\partial \Phi_l}{\partial \xi} \Phi_k \, \mathrm{d}\xi \, \mathrm{d}\eta \, \mathrm{d}\zeta
$$

$$
- B^*_{pq} \hat{Q}_{ql} \int_{\mathcal{E}_{ref}} \frac{\partial \Phi_l}{\partial \eta} \Phi_k \, \mathrm{d}\xi \, \mathrm{d}\eta \, \mathrm{d}\zeta
$$

$$
- C^*_{pq} \hat{Q}_{ql} \int_{\mathcal{E}_{ref}} \frac{\partial \Phi_l}{\partial \zeta} \Phi_k \, \mathrm{d}\xi \, \mathrm{d}\eta \, \mathrm{d}\zeta . \qquad (1.35)
$$

To simplify this equation we can again apply the predefined integrals of Eq. (1.26) and arrive at

$$
\frac{\partial \hat{Q}_{pl}}{\partial t} M_{kl} = \hat{S}_{plm} \Psi_m M_{kl} - A^*_{pq} \hat{Q}_{ql} K^\xi_{kl}
$$

$$
- B^*_{pq} \hat{Q}_{ql} K^\eta_{kl} - C^*_{pq} \hat{Q}_{ql} K^\zeta_{kl} . \qquad (1.36)
$$

Therewith, the kth time derivative of the Taylor expansion as a function of space derivatives can be written in a recursive form

$$
\frac{\partial^k \hat{Q}_p}{\partial t^k} M_{kl} = \frac{\partial^{k-1} \Psi_m}{\partial t^{k-1}} \hat{S}_{plm} M_{kl} - \left(A^*_{pq} K^\xi_{kl} + B^*_{pq} K^\eta_{kl} + C^*_{pq} K^\zeta_{kl} \right) \frac{\partial^{k-1} \hat{Q}_{ql}}{\partial t^{k-1}} . \quad (1.37)
$$

With this expression, the right side of Eq. (1.32) is fully given and we can compute the time-integrated degrees of freedom.

Finally, we are prepared to complete the semi-discrete DG formulation of Eq. (1.25) comprising the time-integrated degrees of freedom and obtain the fully

discrete ADER-DG scheme, which reads

$$\left[\left(\hat{Q}_{pl}^{(m)} \right)^{n+1} - \left(\hat{Q}_{pl}^{(m)} \right)^n \right] |\mathbf{J}| M_{kl}$$

$$= |\mathbf{J}| M_{kl} \hat{S}_{plm} \int_{t^n}^{t^{n+1}} \Psi_m \, \mathrm{d}\tau \tag{1.38}$$

$$- \sum_{j=1}^{s} \frac{1}{2} T_{pq}^{(j)} \left(A_{qr}^{(m)} + |A_{qr}^{(m)}| \right) (T_{rs}^{(j)})^{-1} |\mathbf{S}^{(j)}| F_{kl}^{-,(j)} \int_{t^n}^{t^{n+1}} \hat{Q}_{sl}^{(m)}(\tau) \, \mathrm{d}\tau$$

$$- \sum_{j=1}^{s} \frac{1}{2} T_{pq}^{(j)} \left(A_{qr}^{(m)} - |A_{qr}^{(m)}| \right) (T_{rs}^{(j)})^{-1} |\mathbf{S}^{(j)}| F_{kl}^{+,(j,i,h)} \int_{t^n}^{t^{n+1}} \hat{Q}_{sl}^{(m_j)} \, \mathrm{d}\tau$$

$$+ A_{pq}^* |\mathbf{J}| K_{kl}^{\xi} \int_{t^n}^{t^{n+1}} \hat{Q}_{sl}^{(m)} \, \mathrm{d}\tau + B_{pq}^* |\mathbf{J}| K_{kl}^{\eta} \int_{t^n}^{t^{n+1}} \hat{Q}_{sl}^{(m)} \, \mathrm{d}\tau$$

$$+ C_{pq}^* |\mathbf{J}| K_{kl}^{\zeta} \int_{t^n}^{t^{n+1}} \hat{Q}_{sl}^{(m)} \, \mathrm{d}\tau . \tag{1.39}$$

This scheme is quadrature-free and performs the high-oder time-integration from time level t_n to t_{n+1} in one single step. Thus only the amount of memory of a first-order explicit Euler time stepping scheme is needed. It is performed completely local (only next neighbor information is required) but keeps globally high-order so that superior convergence properties [19, 20] are possessed. The stability of the explicit ADER time stepping scheme is controlled by the CFL number, introduced by Courant, Friedrichs and Lewy [50]. For our scheme, the condition for the maximum timestep of element (m) is given by

$$\Delta t^{(m)} \leq C \frac{1}{2N+1} \frac{l^{(m)}}{c_{max}^{(m)}}, \tag{1.40}$$

where c_{max} is the maximum wave speed supported by the element's material properties. l is a quantity for the size of the element gauged as double the minimum distance between barycenter and surface of the element (which is the diameter of the inscribed sphere for tetrahedrons and cubes). The coefficient C has a maximum value of 0.7 [51] and it is often recommended to set $C = 0.5$.

In order to keep the whole scheme stable, the global timestep has to respect the minimum value

$$\Delta t \leq \min\left(\Delta t^{(m)}\right) \quad \forall\, \mathcal{E}^{(m)} \in \Omega\,. \tag{1.41}$$

For a closer look at the stability criterion of the ADER-DG method via a Von-Neumann analysis see [51].

1.4   Source Terms

Within the ADER-DG scheme it is possible to take any individual source time function $S_p = S_p(\mathbf{x}, t)$ as an input signal. The most general case is referred to as the Finite Source Rupture Model (FSRM) which, e.g., is used to describe point sources via the seismic moment tensor. As in this work we mostly apply the Ricker wavelet as single force or the explosive point source as input term only these standard source types are explained in more detail.

Single Force Point Source
The single force point source acts as a vector at one location.
The Ricker wavelet in time is the second derivative of a Gauss pulse and has the form

$$R(\tau) = R_0 \left(1 - 2(\pi f \tau)^2\right) \exp^{-(\pi f \tau)^2}, \tag{1.42}$$

with the vector components of the single force acting on the three velocity components of direction x, y and z, respectively. R_0 is the amplitude of the signal, f is the dominant frequency and τ denotes the time dependency deferred by the offset. This way a single force can be defined via

$$S_p(\mathbf{x}, t) = \begin{cases} R(\tau)\,, & \text{for } p = 7, 8, 9\,, \\ 0\,, & \text{for } p = 1, 2, \ldots, 6\,. \end{cases} \tag{1.43}$$

The Ricker wavelet is commonly used as it creates P-waves in the direction of propagation and also S-waves perpendicular to it.

Explosive Point Source
The explosive point source is constructed by applying a Ricker or Gauss pulse on each normal stress component. Therewith the input signal acts like an explosion where a compressional wave is travelling radially from the source location

outwards. Using the Ricker pulse $R(\tau)$ (Eq. 1.42) it reads

$$S_p(\mathbf{x}, t) = \begin{cases} R(\tau), & \text{for } p = 1, 2, 3, \\ 0, & \text{for } p = 4, 5, \dots, 9. \end{cases} \tag{1.44}$$

1.5 Boundary Conditions

So far, we have solved the PDE stepwise in time. For one timestep the solution is approximated as a polynomial inside each element, where the elements communicate with their next neighbors. If a side of an element doesn't have any neighbor, we have to apply boundary conditions on it.

Absorbing Boundaries
In general, numerical simulations are performed on an artificially bounded domain. In this case one usually uses absorbing boundaries. We want the waves to go out of the domain without artificial reflections and incoming waves are not allowed. Looking at the flux terms this can easily be achieved. As already announced, the flux term of one side of an element consists of an outgoing and an incoming part, where the incoming part is governed by the neighbor element. Regarding absorbing boundaries we just set the incoming part of the flux to zero and thus, the boundaries should behave absorbent. However, with this approach, there still arise some reflections from the boundaries if the wave does not hit the boundary perpendicularly. Therefore, it is suitable to enlarge the computational domain with coarse elements, to delay this unwanted feature. There have been many attempts to overcome this problem more elegantly and less costly, for example by introducing a special damping profile applied to a buffering layer around the domain, the so-called Convolutional Perfectly Matched Layer (CPML). A detailed study which yields the effectiveness of CPML is presented in Chap. 4.

Free-Surface Boundaries
The free-surface boundary condition represents the contact of an elastic material with air or void. This condition is fullfilled quite naturally by imposing the value of the bulk and shear stresses normal to the free surface to be zero. Within our scheme this can be achieved by creating ghost elements which would theoretically connect to the boundary elements. Then we assign values to the ghost elements

which mirror the above mentioned stresses in normal direction. Hence, the flux
term is zero for those variables at a free surface. The remaining variables of the
ghost elements are the same as for the boundary elements. As a consequence, the
flux term for a side of an element lying at a free surface can be formulated like

$$
\begin{aligned}
F_p^{\text{free}} \;=\;& \frac{1}{2}T_{pq}\left(A_{qr}^{(m)}+|A_{qr}^{(m)}|\right)(T_{rs})^{-1}Q_s^{(m)} \\[2mm]
+\;& \frac{1}{2}T_{pq}\left(A_{qr}^{(m)}-|A_{qr}^{(m)}|\right)\Lambda_{rs}(T_{st})^{-1}Q_t^{(m)}\,.
\end{aligned}
\tag{1.45}
$$

The matrix $\Lambda_{rs} = \text{diag}(-1,1,1,-1,1,-1,1,1,1)$ accounts for the mirroring of
bulk and shear stresses with respect to the face-normal direction.

Inflow Boundaries
The effects of a wave entering the computational domain from the outside can be
handled within the DG method. Suppose that the function $u_s(x,y,z,t)$ describes
the incoming wave for each component s. It can be integrated in space at the
inflow boundary of an element via Gaussian integration. We obtain

$$
U_s^{\text{inflow},(m)} = \sum_{i=1}^{nGP}\omega_i u_s(\xi_i,\eta_i,\zeta_i,t)\,,
\tag{1.46}
$$

where nGP is the number of Gaussian integration points required to exactly
integrate functions up to the desired accuracy order of the scheme and ω_i are
the corresponding integration weights. Therewith, the flux term for an inflow
boundary has the form

$$
\begin{aligned}
F_p^{\text{inflow}} \;=\;& \frac{1}{2}T_{pq}\left(A_{qr}^{(m)}+|A_{qr}^{(m)}|\right)(T_{rs})^{-1}Q_s^{(m)} \\[2mm]
+\;& \frac{1}{2}T_{pq}\left(A_{qr}^{(m)}-|A_{qr}^{(m)}|\right)(T_{rs})^{-1}U_s^{\text{inflow},(m)}\,.
\end{aligned}
\tag{1.47}
$$

As a consequence, this flux term additionally works like an absorbing boundary
for outgoing waves.

Periodic Boundaries
Periodic boundaries are mostly needed for convergence tests and systematic syn-
thetic studies. Provided, that the edges of the boundary elements fit to the edges
of the boundary elements on the opposing face of the computational domain, we
only need to address the corresponding neighbors correctly.

1.6 Mesh Generation and Parallelization

As already announced in Sec. 1.3, the computational domain has to be divided into conforming elements, which we call mesh, in order to apply the numerical scheme. The size of an element strongly depends on the parameterization, i.e., the material properties, the frequency of the signal and the desired level of accuracy (see Chap. 2). Therewith a number of a few million elements is quite usual for common simulations. Thus, we use a mesh generator, e.g. the software GAMBIT or ICEM CFD, which only needs the geometry and several meshing parameters like the element type, edge length or boundary conditions. Then, the mesh is generated automatically.

Solving more and more sophisticated problems nowadays it is indispensable to use high performance computing if we want to obtain the results within an acceptable period of time. Hence, parallelization is another key issue for large scale problems. The partitioning of the mesh into a number of subdomains, which are handled by the single processors, is performed by the free software METIS [52]. Only the elements at a surface of such a subdomain have to participate in message passing as the ADER-DG scheme is completely local (only next neighbor communication). The data transfer between processors is achieved using Message Passing Interface (MPI) libraries.

Chapter 2

A Quantitative Accuracy Analysis

As earthquakes can cause enormous damages which are often focused very locally, it is important to do the simulations enough precisely to resolve all interesting effects. Hence, the question is, which factors influence the quality of a numerical simulation. We distinguish between 3 possible sources of defect, schematically depicted in Fig. 2.1:

First, there exists the uncertainty that the used mathematical model describes the physical problem correctly. Seismic waves are assumed to propagate in an elastic medium, following the theory of linear elasticity [45]. This has turned out to be valid as long as the strain does not exceed an upper limit of 10^{-5} [53].

The second question is if the parameterization is correct. This is a great issue in seismology and lots of efforts are made to learn more about Earth's structure, regional and local material distributions. In the field of seismic tomography it is ongoing work to obtain and better resolve velocity models for geological structures below the surface.

And last but not least one has to control the errors due to the numerical approximation of the solution. To ensure that the accuracy of the simulation is set sufficiently high and to simultaneously keep the computing processor unit (CPU) time as low as possible, a detailed error analysis is required. Several parameters are responsible for the accuracy of the numerical method, such as the error norm, the spatial discretization, i.e., the number of elements per wavelength, the chosen approximation order of the scheme, and the propagation distance of the waves due to numerical dispersion and dissipation.
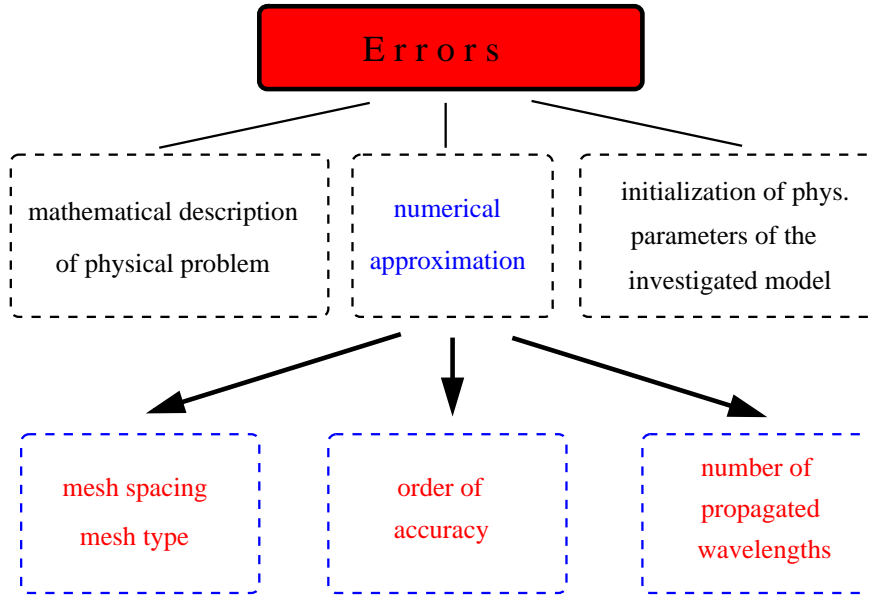
Figure 2.1: *Schematic listing of possible errors which influence the quality of a numerical simulation.*

A sound error analysis for three types of the FD method is carried out by Kristek & Moczo [54] for the 1 D case and a maximum propagation distance of 20 dominant wavelengths. They also include the optimally accurate scheme of Geller & Takeuchi [55] in their analysis. Similarly, Fornberg [56] shows an accuracy analysis for the PS method using a phase error estimator as error norm. Furthermore, Seriani & Priolo [13] study the accuracy of the SEM showing the relative evolution of the numerical error depending on approximation order, spatial sampling and propagation distance. A more recent work on the SEM is presented by Ampuero & Nissen-Meyer [57], who study the dispersion error of the SEM analytically and replace the typically used low-order Newmark time integration scheme with higher-order symplectic schemes. They prescribe an expected (i.e., data-driven) error tolerance and then extract optimal simulation parameters for that accuracy, such as the approximation order in space and time, to minimize the computational cost. Moreover, they also define errors for phase and amplitude separately. To this end they use cross-correlation to determine the phase error and the root mean square (RMS) to obtain the amplitude misfit after shifting the seismogram by the phase error. It should be mentioned that these are alternative error measures of numerical seismograms since they also separate phase and amplitude misfits. However, the frequency dependence of the misfit cannot

be estimated this way, which might be the main drawback. We remark, that in some cases it can be extremely useful to capture the frequency band, where a numerical method loses or produces energy, even though the initial source signal might have a different frequency band.

Therefore, we claim that the error norms suggested by Kristeková *et al.* [21] should be mainly used in the future as they are based on the time-frequency representation of the seismogram misfit. The time-frequency representation provides the time evolution of the spectral content and allows for the clear separation of amplitude and phase errors obtained by the numerical method. We perform such a misfit analysis for a systematic study including the abovementioned parameters, different mesh types and mesh spacings. Our results can be directly used to set up the necessary modeling parameters for practical applications, such as the minimum approximation order for a given mesh spacing to reach a desired accuracy. Finally, we apply our results to the WP2_LOH1 and WP2_LOH3 problems of the *Seismic wave Propagation and Imaging in Complex media: a European network* (SPICE) code validation project (www.nuquake.eu/SPICECVal) including heterogeneous material and the free surface boundary condition. Note that the original ideas of such a benchmarking exercise have been suggested by the Southern California Earthquake Center (SCEC) code validation project [58], however, the SPICE project extended and considerably improved these ideas by (a) covering systematically important categories of different problem configurations, (b) applying newest quantitative misfit criteria to compare the obtained solutions, and (c) establishing and providing a long-term interactive database for uploading and comparing numerical solutions with analytical or reference solutions. Therefore, we use the SPICE Code Validation website to confirm the validity of our error analysis and to compare our simulation results with those obtained by other methods. The results of these other methods (so far only FD and FE results are available!) are shown in detail by Kristeková *et al.* [21].

2.1 The Time-Frequency Representation

In numerical seismology a simple and often used error norm is the difference seismogram between the numerical solution and a reliable reference solution which visually provides a good first comparison, but is only a very qualitative measure. Furthermore, a simple integral criterion is the RMS misfit. However, both measures quantify the difference between seismograms without distinguishing prop-

erly between amplitude or phase errors. In particular, the RMS usually considerably overestimates the misfit as it wrongly attributes amplitude errors due to phase shifts. Therefore, Seriani & Priolo [13] propose a frequency error index which is a complex function given by the ratio of the Fourier transform of the numerical solution and the analytic solution. This way, they determine the minimum wavelength for which a numerical method is sufficiently accurate. By considering the real and imaginary parts of their frequency error index separately, they can distinguish between errors due to amplitude variations or velocity dispersion, i.e., phase errors, respectively.

Recently, Kristeková *et al.* [21] introduced new misfit criteria for quantitative comparisons of seismograms which are based on the time-frequency representation (TFR) using the continuous wavelet transform. With the TFR of the misfit, they can extract the time evolution of the spectral content. Therefore, they define a local time-frequency envelope difference

$$\Delta E(t, f) = |W(t, f)| - |W_{\text{ref}}(t, f)| \tag{2.1}$$

and a time-frequency phase difference

$$\Delta P(t, f) = \frac{1}{\pi} |W_{\text{ref}}(t, f)| \left(\arg[W(t, f)] - \arg[W_{\text{ref}}(t, f)] \right) , \tag{2.2}$$

where $W(t, f)$ (resp. $W_{\text{ref}}(t, f)$) is the numerical (resp. reference) wavelet in the time frequency representation obtained by the continuous wavelet transform. The continuous wavelet transform (CWT) of the signal is defined by

$$CWT\{s(t)\} \sim \int_{-\infty}^{\infty} s(t) \Psi^*(t - b) \, \mathrm{d}t , \tag{2.3}$$

where b is the translational parameter and Ψ^* is the complex conjugate of the analyzing wavelet Ψ. In our case the latter is the Morlet wavelet ([59]), given by

$$\Psi(t) = \pi^{-1/4} \exp(i\omega_0 t) \exp(-t^2/2) , \tag{2.4}$$

with $\omega_0 = 6$. By setting $b = t$ we get the time-frequency representation of the signal:

$$W(t, f) = CWT_{t=b}\{s(t)\} . \tag{2.5}$$

For a detailed description of the continuous wavelet transform the reader is referred to the book of Holschneider [60]. The free software package TF-MISFITS for signal analysis is available at www.nuquake.eu/Computer_Codes.

Now we are prepared to compute the time-frequency envelope misfit (TFEM) and
the time-frequency phase misfit (TFPM), given by

$$
\text{TFEM}(t, f) \;=\; \frac{\Delta E(t, f)}{\max_{t,f}(|W_{\text{ref}}(t, f)|)} \,,
$$

$$
\text{TFPM}(t, f) \;=\; \frac{\Delta P(t, f)}{\max_{t,f}(|W_{\text{ref}}(t, f)|)} \,. \tag{2.6}
$$

Both differences are functions of time and frequency and they are normalized
with respect to the maximum absolute TFR value of the reference signal.
Kristeková *et al.* [21] also obtain purely time- or frequency-dependent quantities
of the misfits by the projection onto one of the two domains. Projection on the
time domain yields the time-dependent envelope and phase misfits (TEM and
TPM), given by

$$
\text{TEM}(t) = \frac{\langle \Delta E(t, f) \rangle_f}{\max_t \left(\langle |W_{\text{ref}}(t, f)| \rangle_f \right)} \,, \quad
\text{TPM}(t) = \frac{\langle \Delta P(t, f) \rangle_f}{\max_t \left(\langle |W_{\text{ref}}(t, f)| \rangle_f \right)} \,, \tag{2.7}
$$

where $\langle \rangle_f$ means the average value referring to frequency. Respectively project-
ing on the frequency domain offers the frequency-dependent envelope and phase
misfits (FEM and FPM), which read

$$
\text{FEM}(f) = \frac{\langle \Delta E(t, f) \rangle_t}{\max_f \left(\langle |W_{\text{ref}}(t, f)| \rangle_t \right)} \,, \quad
\text{FPM}(f) = \frac{\langle \Delta P(t, f) \rangle_t}{\max_f \left(\langle |W_{\text{ref}}(t, f)| \rangle_t \right)} \,, \tag{2.8}
$$

with $\langle \rangle_t$ denoting the average value referring to time. To be able to compare all
these results with the single valued measures we also compute the averaged value
of the envelope and phase misfits (EM and PM), defined as

$$
\text{EM} = \sqrt{\frac{\sum_f \sum_t |\Delta E(t, f)|^2}{\sum_f \sum_t |W_{\text{ref}}(t, f)|^2}} \quad \text{and} \quad \text{PM} = \sqrt{\frac{\sum_f \sum_t |\Delta P(t, f)|^2}{\sum_f \sum_t |W_{\text{ref}}(t, f)|^2}} \,. \tag{2.9}
$$

In the following, we apply these new misfit criteria to separate amplitude and
phase errors to quantitatively analyze the performance of the ADER-DG scheme
with respect to the approximation order, the mesh type and spacing and the
propagation distance of the waves.

2.2   Model Setup

In this section the computational setup for the numerical accuracy analysis in
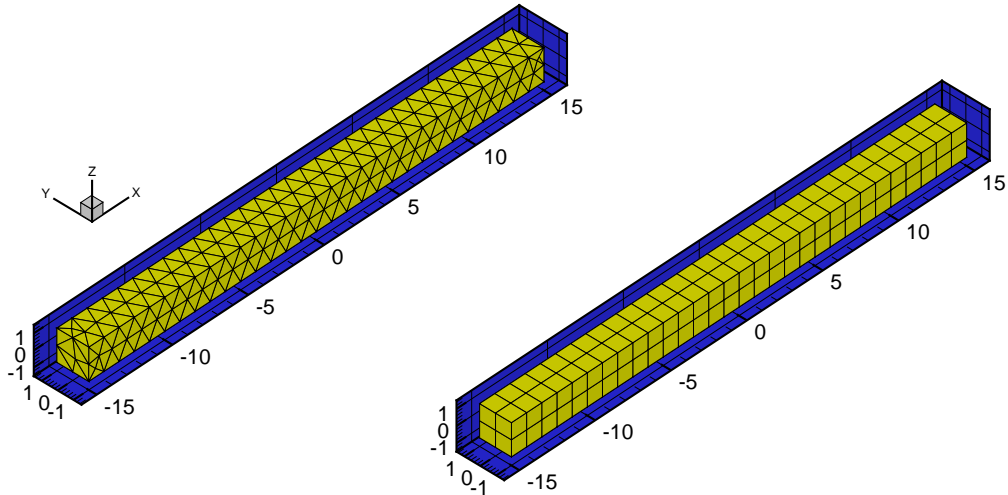3-D is described in detail. We use eleven different unstructured tetrahedral and

Figure 2.2: *Computational domain discretized by tetrahedral (left) and hexahedral (right) Mesh 2 with periodic boundary conditions in the x-, y-, and z-direction applied to simulate the propagation of the Ricker-type plane wave in the x-direction for 120 wavelengths.*

eleven hexahedral meshes discretizing a cuboid specified by

$$\Omega = [-15, 15] \times [-1, 1] \times [-1, 1] \,\mathrm{m}^3 \ \in \mathbb{R}^3 \tag{2.10}$$

elongated in x-direction as shown in Fig. 2.2. The meshes are generated in a way that periodic boundary conditions in x-, y-, and z-direction can be applied. The mesh spacing Δh_k is represented by the average edge length of each of the meshes indicated by "Mesh k", where $\Delta h_k = \frac{2}{k}\,\mathrm{m}$, for $k \in [2, 3, 4, 5, 6, 8, 10, 12, 14, 16, 18]$. As initial condition, we use a plane wave with a Ricker-type amplitude distribution

$$A(x) = \left(1 - 2(\pi f x)^2\right) \exp^{-(\pi f x)^2}, \tag{2.11}$$

with $f = 1.25\,\mathrm{Hz}$, and propagate it with wave velocity $c = 1\,\mathrm{ms}^{-1}$ in the positive x-direction. Therefore, an analytical seismogram is given by the same Ricker wavelet in time, as shown in Fig. 2.3(a), with a dominant frequency $f_d = 1.25\,\mathrm{Hz}$ and hence a dominant wavelength $\lambda_d = 0.8\,\mathrm{m}$. The TFR of the used Ricker wavelet is shown in Fig. 2.3(b). We remark, that we use a plane compressional wave in a homogeneous elastic medium. However, the wave could also represent a pure pressure wave in an acoustic medium or a pure shear wave in an elastic medium. Due to this generality, we will not refer to one particular type of planar wave here, but want to emphasize that always the slowest wave, i.e., the shortest wavelength, has to be considered, when transforming these results to more complicated cases with different types of waves. The abovementioned parameters
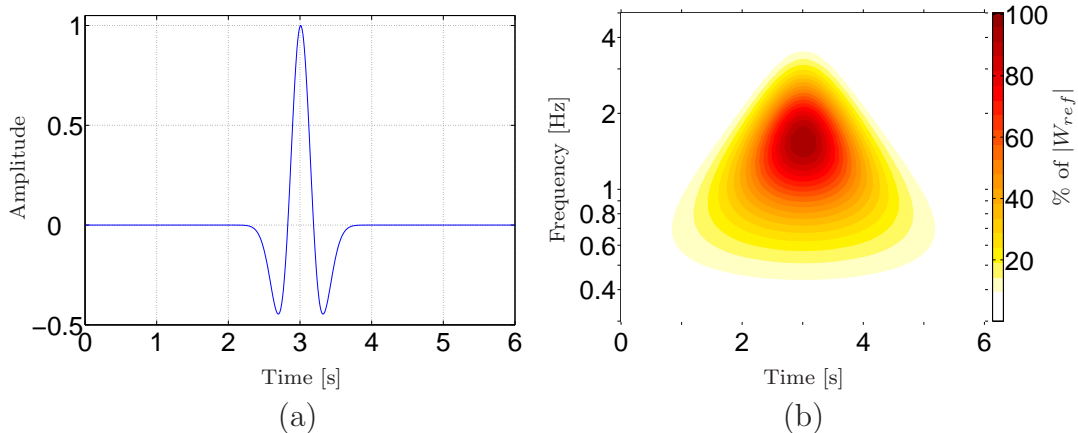
Figure 2.3: *(a) Ricker-type pulse in the time domain used for the accuracy study in the elongated computational domain Ω. (b) The time-frequency representation of the Ricker signal obtained as the absolute value of the continuous wavelet transform.*

determine the number of elements per dominant wavelength $N_k = \lambda_d/\Delta h_k = 0.4\,k$ that each Mesh k provides for the wave propagation simulation. We solve the test problem with ADER-DG schemes of order 2 to order 7, indicated by ADER-DG $\mathcal{O}2$ to ADER-DG $\mathcal{O}7$, respectively.

The synthetic seismograms are recorded at 30 receivers equidistantly distributed along the x-axis at $\mathbf{x}_r = (r-15.5, 0, 0)\,\text{m}$, for $r = 1, ..., 30$, up to a total simulation time $T = 120\,\text{s}$ at a sampling rate of $0.01\,\text{s}$. This means that the Ricker pulse propagates through the domain Ω four times along the x-direction. Note that in principle we solve a 1D wave propagation problem, however, we compute it in a fully 3-D elastic volume discretized by different meshes. For the tetrahedral meshes the orientations of the single elements and their interfaces are different and never aligned to one of the coordinate axes, which represents the same case as in a real application as unstructured meshes can never be aligned to any space direction.

The analytical solution for the test cases is obtained by simply shifting the given Ricker wavelet in time with respect to the corresponding receiver position and its theoretical arrival time, which is known exactly. The synthetic seismograms contain the propagating Ricker pulse periodically every $30\,\text{s}$ due to the periodicity of the domain Ω. Therefore, we cut out seismogram intervals of 2000 time samples, i.e., $20\,\text{s}$, centered around the theoretical arrival time of the peak amplitude to analyze the misfits. This ensures that the seismograms well include the wavelet and numerical dispersion effects but avoids contaminating effects due to the pe-
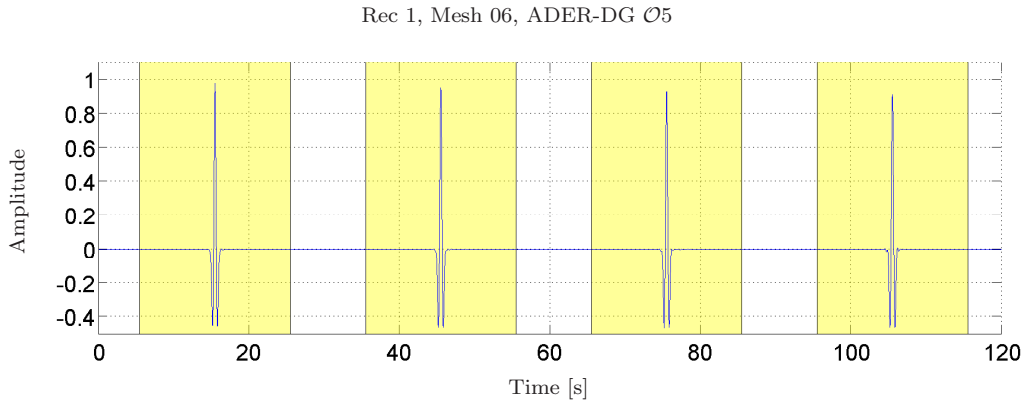
Figure 2.4: *Seismogram computed using tetrahedral Mesh 6 with an ADER-DG O5 scheme at receiver 1 at $(-14.5, 0, 0)$ m where the maximum of the Ricker pulse passes for the first time at 15.5 s and then periodically in intervals of 30 s. Note the decrease in the maximum amplitude and the increase of numerical dispersion effects. The analysis intervals of the lengths of 20 s are shown as yellow shaded regions.*
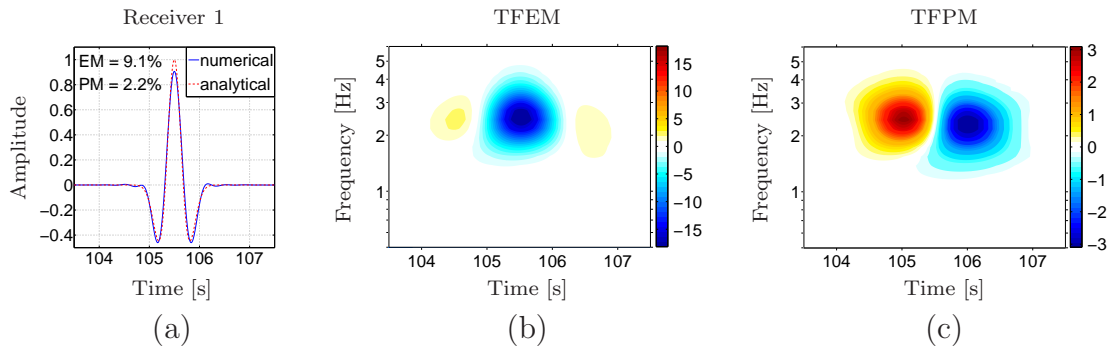

Figure 2.5: *(a) A zoomed view of the numerical solution (solid) of Fig. 2.4 at the last passage of the Ricker pulse at receiver 1 at 105.5 s in comparison to the analytical solution (dashed) together with the EM and PM values. (b) Color-coded time-frequency representation of the EM given in % from 0.5 to 6 Hz and in the same time interval as (a). (c) Color-coded time-frequency representation of the according PM.*

riodicity of the signal. An example seismogram computed using the tetrahedral Mesh 6 with an ADER-DG $\mathcal{O}5$ scheme is shown in Fig. 2.4 for receiver 1, where the Ricker pulse passes four times while continuously losing amplitude and producing slightly more dispersion errors. An enlarged comparison to the analytical solution after the fourth passage is shown in Fig. 2.5(a). This plot also shows the single-valued EM and PM values for this comparison and confirms that the size of the analysis interval of 20 s for each pulse is large enough to avoid the influence of the periodic signal. We remark that this also holds true for seismograms computed with ADER-DG $\mathcal{O}2$ schemes on the coarsest Mesh 2 for both element types. Figs. 2.5(b) and (c) show the TFEM and the TFPM, respectively, in a frequency range from 0.5 to 6 Hz and in the same time interval from 103.5 to 107.5 s as chosen for Fig. 2.5(a). Considering also the different scaling of the colorbars, we observe, that the amplitude error attributed to the EM is about four times larger than the phase error given by the PM. In particular, Fig. 2.5(b) nicely shows a strong minimum in blue around the theoretical arrival time 105.5 s of the peak amplitude. There, most of the amplitude is lost, while towards both sides of this minimum, light red maxima highlight the spurious oscillations. Fig. 2.5(c) instead shows a positive and a negative local extremum indicating that the first numerical phase arrives slightly too fast, and then disappears too late, after the peak of the pulse has passed. However, at the peak passage time at 105.5 s the TFPM is almost zero throughout the whole frequency band. These plots also help to get a *feeling* about the size of the EM and PM values obtained by integrating over the time and frequency axes, and their relation to the visual seismogram difference. For a presentation of a systematic study of the TFR of amplitude- and phase-modified simple wavelets, we refer to the work of Kristeková *et al.* [21].

2.3   Results

We present the accuracy results for the different simulations in order to show the dependence on element type, approximation order, mesh spacing and propagation distance. To this end, we first consider the EM between the numerical and analytical seismograms as given in Eq. (2.9).

In Fig. 2.6 we plot the results obtained on nine of the eleven different tetrahedral meshes indicated by Mesh k leading to a spatial sampling of $N_k \in [0.8, 1.2, 1.6, 2.0, 2.4, 3.2, 4.0, 4.8, 7.2]$, respectively. Each plot shows how the EM increases with the propagation distance. The symbols indicate the EM at the
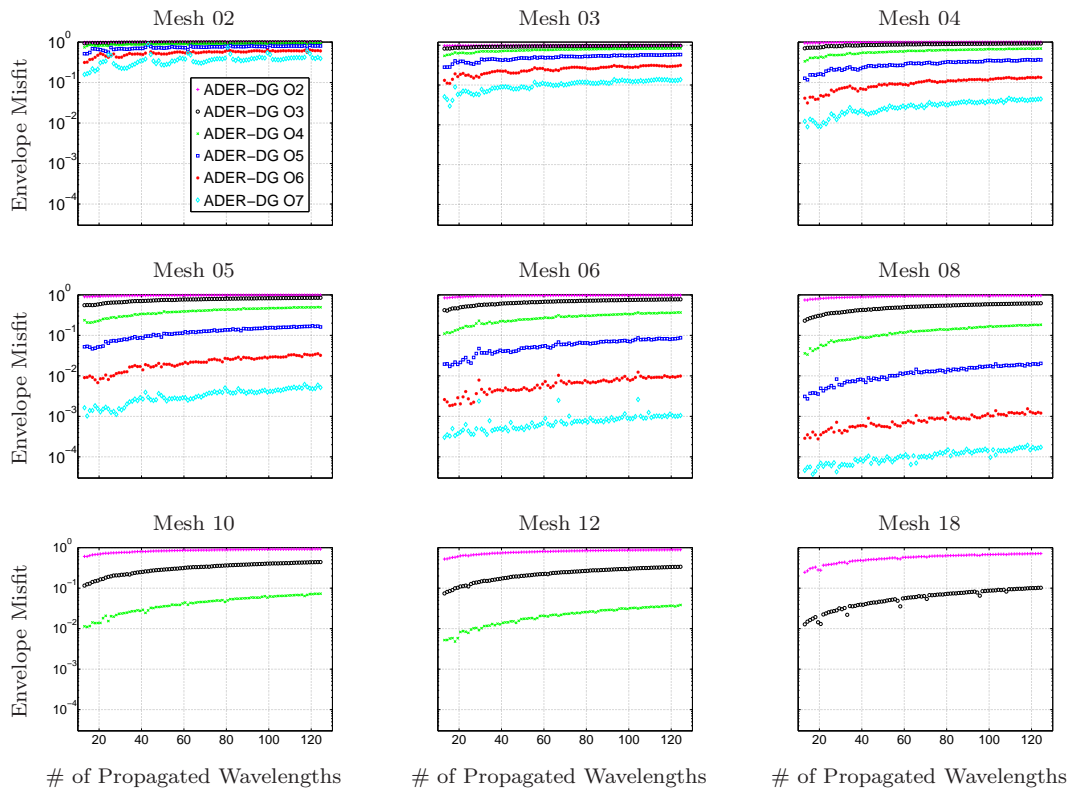
Figure 2.6: *Envelope misfit depending on the propagation distance, given as the number of propagated dominant wavelengths λ_d, and different orders of accuracy computed on tetrahedral meshes. Each of the different meshes indicated by Mesh k provides a spatial sampling of $N_k = 0.4\,k$ elements per dominant wavelength.*

receiver positions and the different symbol types denote the different orders of approximation of the used ADER-DG scheme as given in the legend. Further-more, we observe that some of the lines contain data points that deviate from the general trend especially visible in the results using Mesh 06, Mesh 08 and Mesh 18. Analyzing our results with respect to such outliers shows that they correlate to very particular or even extreme positions of a receiver within a tetrahedral element. This means that for a receiver position very close to the element edge or, especially, to an element vertex, i.e., in the corner of a tetrahedral element, the accuracy might be decreased or increased due to the behavior of the ap-proximation polynomial. We remark that in contrast to many other nodal-based numerical schemes (e.g. SEM) with nodes at the element edges and corners, the DG approach uses a modal basis which is not connected to particular integration

points inside an element. Therefore, it is difficult to control or predict the behavior of very high-order polynomials at such special positions. Furthermore, due to the logarithmic scale of the EM in Fig. 2.6, the variation of the misfits for higher approximation orders are visually enhanced. Nevertheless, this location effect always remains relatively small and the error variation due to different locations is much less than the error difference between two subsequent orders.

Let us define the limit of an acceptable EM, represented in the plots of Fig. 2.6 as the constant line at $EM = 10^{-2} = 1\%$. This is of course an arbitrary choice for our synthetic study here. In practical applications the acceptable accuracy limit should always be one order of magnitude below the accuracy of the modeling parameters (e.g. velocity structure, attenuation properties, etc.) as suggested by Ampuero & Nissen-Meyer [57] to make sure that the numerical error does not dominate. We observe that Mesh 02 and 03 are definitely too coarse to obtain reasonably accurate results, even with the ADER-DG $\mathcal{O}7$ scheme. For Mesh 04 the ADER-DG $\mathcal{O}7$ scheme reaches the desired accuracy just for propagation distances of less than 20 wavelengths. On finer meshes the misfits gradually decrease for each scheme as expected, however, for the lower-order ADER-DG $\mathcal{O}2$ and ADER-DG $\mathcal{O}3$ schemes, even the finest Mesh 18 is still too coarse to reach $EM = 1\%$. Due to the increasing computational costs of the higher-order schemes we show only the results for the orders below $\mathcal{O}5$ for Mesh 10 and 12 and only results for orders below $\mathcal{O}4$ for the finest Mesh 18 in order to keep the central processor unit (CPU) time reasonable. However, this trend continues to machine precision as shown in previous work [19, 20]. A further observation is, that for a chosen mesh and approximation order the misfits increase continuously but rather slowly with longer propagation distances. Over the range of propagation distances investigated in this study the misfits of two schemes of subsequent approximation orders can differ by one order of magnitude and this difference remains quite stable.

Fig. 2.7 shows similar results for hexahedrons as already discussed for tetrahedrons. In general, we can detect, that the lines for each of the data sets are much smoother than those computed on tetrahedrons. The reason for this is, that the hexahedral meshes are completely regular. There arise no acute angles at the vertices of an element and the receiver location with respect to its position inside an element can be controlled quite easily. Another observation is the magnitude of the misfits being higher for hexahedrons than for tetrahedrons using the same element edge length. In our study we examine tetrahedral and hexahedral meshes of the same spatial sampling which corresponds to a one dimensional quantity. However, simulating a three dimensional problem, the polynomial approxima-
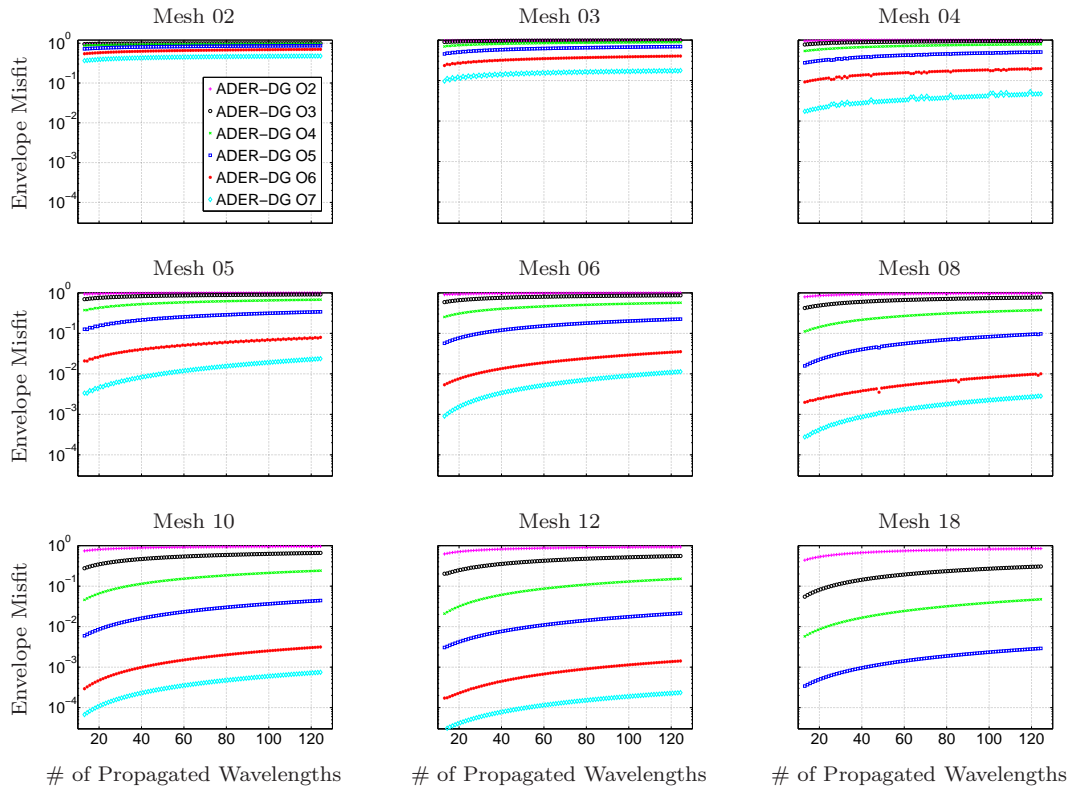
Figure 2.7: *Envelope misfit depending on the propagation distance, given as the number of propagated dominant wavelengths λ_d, and different orders of accuracy computed on hexahedral meshes. Each of the different meshes indicated by Mesh k provides a spatial sampling of $N_k = 0.4\,k$ elements per dominant wavelength.*

tion of the solution is related to the full volume of the elements. Therefore, the above-mentioned difference in the misfits becomes perspicuous comprising that the volume of a regular tetrahedron is $\frac{\sqrt{2}}{12}\Delta h^3$ whereas the volume of a hexahedron is Δh^3.

   Considering the PM as given in Eq. (2.9), the results shown in Fig. 2.8 for tetrahedrons and in Fig. 2.9 for hexahedrons have the same shape as the accordant results of the EM study. However, when comparing the plots of the EM and PM we see systematically smaller values for the PM, which means that the numerical dispersion is less than numerical dissipation obtained by ADER-DG schemes and confirms the result shown explicitly in Fig. 2.5. This fact allows us to conclude that, if correct amplitudes are less important than phases, coarser meshes could be used. Nevertheless, the previous statements made for the EM in Figs. 2.6 and
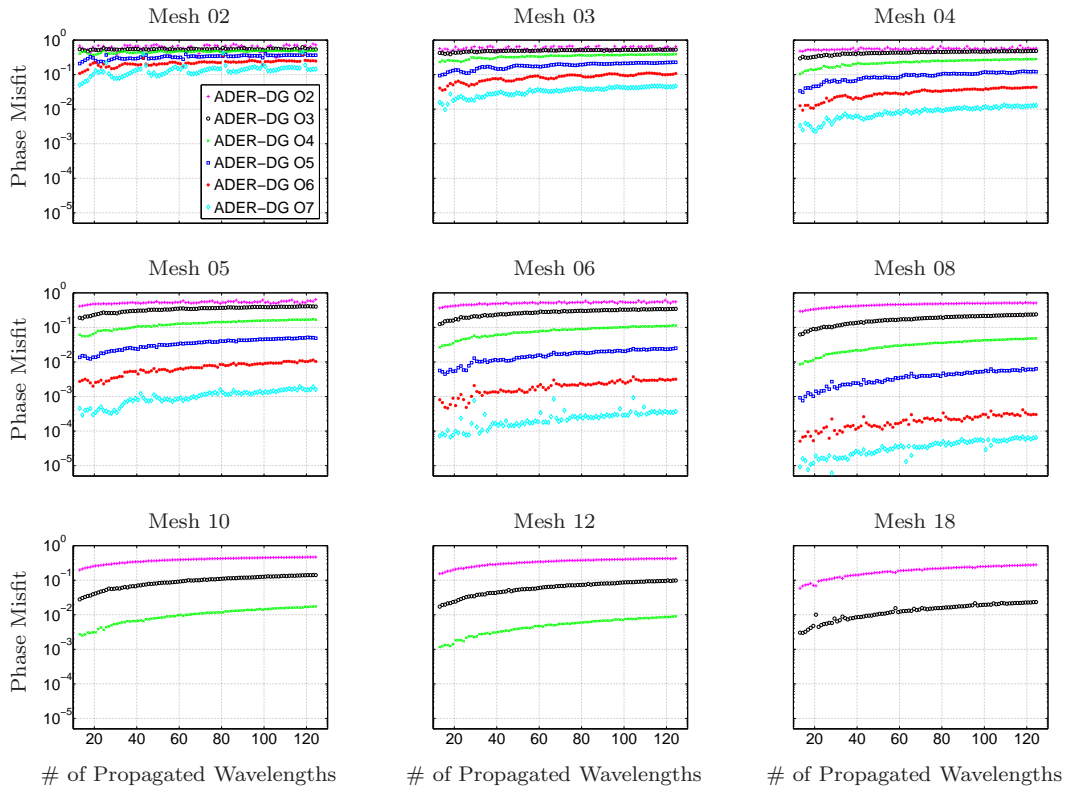
Figure 2.8: *Phase misfit depending on the propagation distance, given as the number of propagated dominant wavelengths λ_d, and different orders of accuracy computed on tetrahedral meshes. Each of the different meshes indicated by Mesh k provides a spatial sampling of $N_k = 0.4 \, k$ elements per dominant wavelength.*

2.7, do also apply for the PM in Figs. 2.8 and 2.9.

Now, let us look at our results from a different perspective. In Fig. 2.10 we plot the EM and PM versus the number N_k of elements per wavelength for different orders of accuracy and for different propagation distances computed on tetrahedral and hexahedral meshes. The symbols again indicate the approximation order as before, whereas the differently colored lines represent different propagation distances of 20 (black), 40 (green), 80 (red) and 120 (blue) dominant wavelengths λ_d. We remark, that only the ADER-DG $\mathcal{O}2$ and ADER-DG $\mathcal{O}3$ schemes have been applied to all eleven tetrahedral meshes, whereas the scheme ADER-DG $\mathcal{O}4$ was applied only to the first eight tetrahedral meshes and the high-order schemes ADER-DG $\mathcal{O}5$ to ADER-DG $\mathcal{O}7$ to the first six tetrahedral meshes. As the computations on hexahedral meshes were less costly in terms of
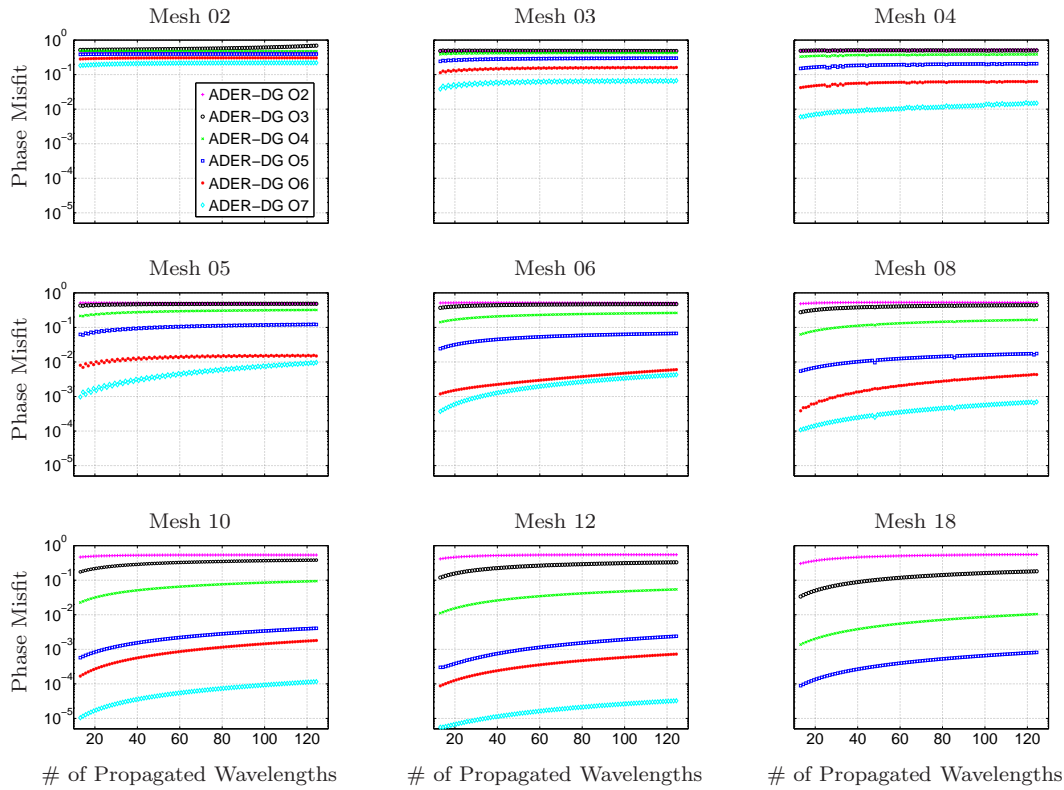
Figure 2.9: *Phase misfit depending on the propagation distance, given as the number of propagated dominant wavelengths λ_d, and different orders of accuracy computed on hexahedral meshes. Each of the different meshes indicated by Mesh k provides a spatial sampling of $N_k = 0.4\,k$ elements per dominant wavelength.*

time we could also comprise all eleven hexahedral meshes up to the ADER-DG $\mathcal{O}5$ scheme, the scheme ADER-DG $\mathcal{O}6$ was applied to the first 10 hexahedral meshes and the scheme ADER-DG $\mathcal{O}7$ even to the first 9 hexahedral meshes. This explains the different numbers of data points of the graphs in Fig. 2.10. All four plots in Fig. 2.10 clearly show the faster decrease of misfits for the higher-order methods with the increasing spatial sampling rate N_k, i.e., for decreasing mesh spacing Δh_k. For the ADER-DG $\mathcal{O}2$ and ADER-DG $\mathcal{O}3$ schemes there is little improvement from 0.8 to 7.2 elements per wavelength and a much higher spatial sampling rate would be necessary to reach the desired error level of $EM = 1\%$. We show that especially for lower-order schemes the number of elements per wavelength for a scheme of order n always has to be increased considerably in order to reach the accuracy of a scheme of order $n+1$. Furthermore, we now observe
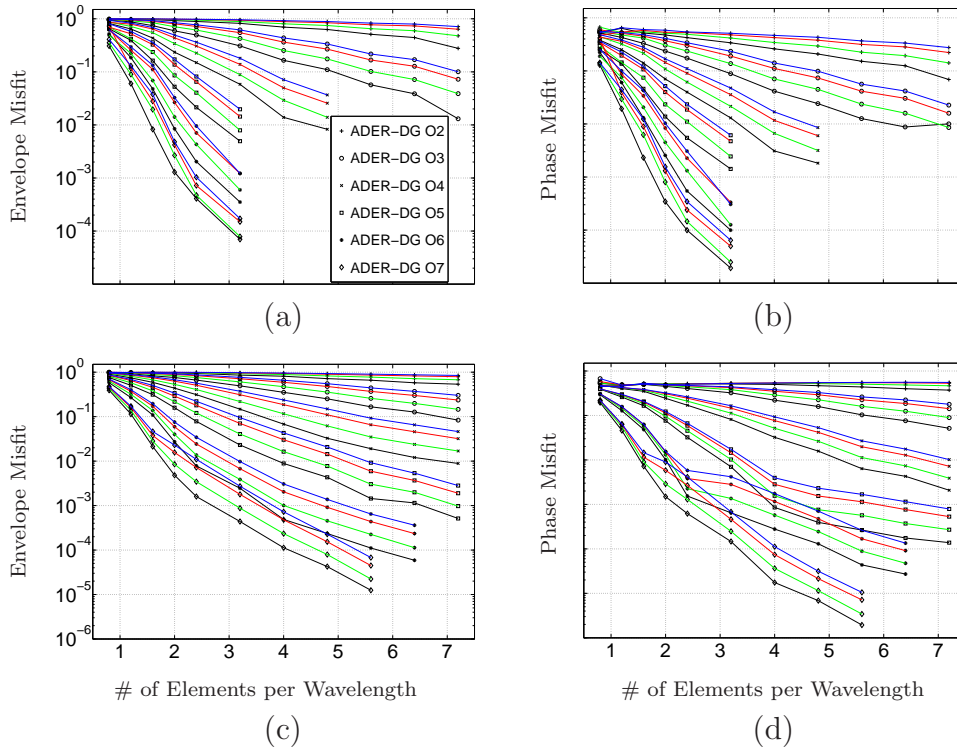
Figure 2.10: *Envelope and phase misfits depending on the spatial sampling for different orders of accuracy and varying propagation distances, i.e., for 20 (black), 40 (green), 80 (red) and 120 (blue) propagated wavelengths: (a) EM computed on tetrahedral meshes, (b) PM computed on tetrahedral meshes, (c) EM computed on hexahedral meshes and (d) PM computed on hexahedral meshes.*

more clearly that in general the misfit obtained by a scheme of order n for only 20 propagated wavelengths is larger than the misfit obtained by a scheme of order $n+1$ even for 120 propagated wavelengths. Note that this statement is valid for both EM and PM computed on tetrahedral meshes, whereas the values of the PM are systematically smaller than those of the EM. Looking at the hexahedron study it still holds for lower orders of accuracy. Within the EM the only exception appears for a mesh spacing of more than 2 elements per wavelength and below an error level of 2%. Here, the misfit obtained by a scheme of order 6 for 20 propagated wavelengths is larger than the misfit obtained by the scheme of order 7 up to 80 propagated wavelengths. Regarding the PM, we also have to diminish our statement. For adjacent orders of accuracy above $\mathcal{O}5$, at a mesh spacing exceeding 2 elements per wavelength, where we already reach error levels below 1%,

we only achieve lower errors with the higher order scheme up to 80 propagated wavelengths (which still means a feasible 4 times longer propagation distance). We can still conclude, that higher-order schemes should always be preferred even when propagating only short distances, as the propagation distance obviously has a smaller influence on the accuracy than the chosen order.

However, even if these results strongly recommend the use of the higher-order ADER-DG schemes regarding the high accuracy of results, the most important issue is to analyze the schemes also with respect to their computational cost. The cost per element clearly increases for higher orders of approximation and the time step length decreases according to the stability criterion (see Eq. (1.40)). However, as observed before, with higher-order schemes we can use coarser meshes and therefore reduce the total number of elements. The first question therefore is whether the reduction in the number of elements can compensate for the increase in cost per element and the more restrictive time step criterion Eq. (1.40). The second question arises by considering different element types. On the one hand, Eq. (1.40) includes the diameter of the element's inscribed sphere in the nominator, which restricts tetrahedrons to a smaller time step compared to hexahedrons of the same mesh spacing. On the other hand, as we have seen in Figs. 2.6 - 2.9, tetrahedrons reach the higher accuracy, provided that we use the same order of the scheme and the same mesh spacing for both mesh types. Therefore, the crux is, which mesh type needs the lower CPU time to attain a desired error level.

In Fig. 2.11 (a), we show the obtained EM (for tetrahedrons in black and for hexahedrons in red) versus the required CPU time to reach the final simulation time $T = 120\,\text{s}$ for a parallel computation on 8 Intel Itanium2 Montecito 1.6 GHz cores. Like in Fig. 2.10, the number of data points for each line depends on how many meshes contributed to the order of accuracy in this respect. Recalling our desired accuracy limit EM $= 1\%$, the plot shows that this accuracy is achieved with the ADER-DG $\mathcal{O}7$ scheme on a hexahedral mesh in the least computational time of about 1.4 h. In general, Fig. 2.11 (a) gives a clear answer to both the questions posed above. Firstly, if we consider the results for computations on the different mesh types separately, i.e., either tetrahedral or hexahedral meshes, the figure demonstrates that the use of a scheme of order n usually requires less CPU time to reach a desired accuracy than a scheme of order $n - 1$. Therefore, the increased cost per element and the more restrictive time step criterion can even be overcompensated by the use of a coarser mesh consisting of less and larger elements. Secondly, it is obvious and universal, that for a given order of the scheme
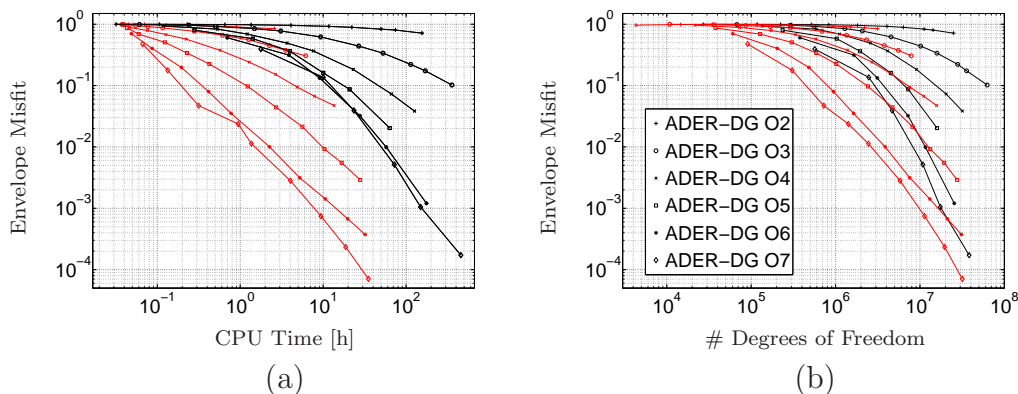
Figure 2.11: *Envelope misfit depending on the required CPU time (a) to reach the final simulation time of $T = 120$ s for a parallel computation on 8 Intel Itanium2 Montecito Dual Core 1.6 GHz cores and (b) depending on the required total number of degrees of freedom, which is proportional to the memory required. The black data sets refer to the tetrahedral study whereas the red ones refer to the hexahedral study.*

it is always faster to accomplish the simulation on a hexahedral mesh. E.g., to reach the desired error level of EM = 1%, the fastest computation on tetrahedrons requires about 50 h which is approximately 36 times longer than simulating 120 s of wave propagation on a hexahedral mesh with the same accuracy.

Fig. 2.11 (b) shows the obtained EM versus the total number of degrees of freedom, which are a measure of the memory used during the computations. Again, the data sets in black (resp. red) refer to tetrahedral (resp. hexahedral) meshes. Memory requirements are typically very low for our implementation of the ADER-DG scheme and therefore are not considered in detail in this study. However, the number of degrees of freedom per element and variable is

$$L = \frac{(N + 1)(N + 2)(N + 3)}{6} , \qquad (2.12)$$

where N is again the degree of the approximation polynomial (see also Sec. 1.3.1). For details we refer to previous work [20]. Nevertheless, we see that also concerning the memory requirements, it seems to be beneficial to use high-order schemes, as the enormous reduction in mesh elements in 3-D overcompensates the additional memory needed by each single element. Moreover, the difference between tetrahedral and hexahedral meshes seems not so formidable as regarding the CPU time, but it is still evident, that we reduce the memory requirement on hexahedral meshes.

In the following, we use the results of the accuracy study on tetrahedral meshes to check if they can be used reliably for more complex modeling setups, where heterogeneous material, P- and S-waves, and free surface waves are present. Note, that of course the results of the previous accuracy analysis have to be applied considering the shortest wave length expected.

2.4   Application to SPICE Code Validation Problems

In order to validate our results of the accuracy analysis, we use the obtained information in the application of the ADER-DG schemes to two test problems published in the final report of the LIFELINES PROGRAM TASK 1A01 [58] of the Pacific Earthquake Engineering Research Center. The two test cases, called Wave Propagation 2 - Layer Over Halfspace 1 and 3 (WP2_LOH1 and WP2_LOH3), are part of the multi-institutional *Seismic wave Propagation and Imaging in Complex media: a European network* (SPICE) code validation project. The quasi-analytic solutions of the problems are computed by the reflectivity method and are compared to all numerical solutions to evaluate their accuracy. To this end, we chose a desired seismogram error level that should be obtained by the simulation and discretize the model using a tetrahedral mesh spacing according to the expected wavelengths, the propagation distance and the selected approximation order.

2.4.1   WP2_LOH1

The first test case we want to examine, Wave Propagation 2 - Layer Over Halfspace 1 (WP2_LOH1), has the purpose of assessing the precision of modeling a planar free surface and planar internal interface, which constitutes a layer over homogeneous halfspace as the computational domain. The geometry of this problem is illustrated in Fig. 2.12. Only one of 4 symmetric quarters is shown here. The computational domain $\Omega = [-15, 15] \times [-15, 15] \times [0, 17]\,\text{km}^3$ contains a surface layer of $1\,\text{km}$ height, which has a minimum S-wave velocity of $c_s = 2000\,\text{m/s}$, the P-wave velocity is $c_p = 4000\,\text{m/s}$ and the density is $\rho = 2600\,\text{kg/m}^3$. The subjacent halfspace has $c_s = 3464\,\text{m/s}$, $c_p = 6000\,\text{m/s}$ and $\rho = 2700\,\text{kg/m}^3$. The seismic source is a point dislocation, represented by a double couple source. A
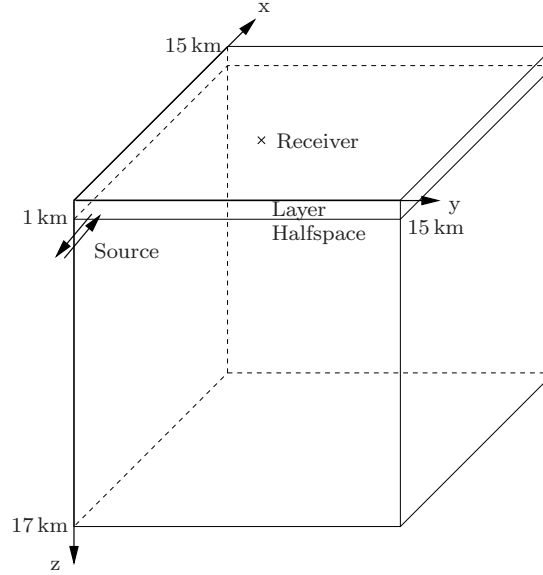
Figure 2.12: *Sketch of one of 4 symmetric quarters indicating the geometry of test case WP2_LOH1.*

couple source is a pair of parallel forces of equal magnitude in opposite direction and acting on different lines some distance apart from each other. As a measure of strength of the source, the 3×3 seismic moment tensor $\mathbf{M}$ describes the 9 possible combinations of forces and distances. In our case the only non-zero entries of the seismic moment tensor are $M_{xy} = M_{yx} = M_0 = 10^{18}$ Nm. The location of the point source is $(x_s, y_s, z_s) = (0, 0, 2)$ km, i.e., the center of the $xy-$plane of the domain Ω in 200 m depths. The moment-rate time history is given by the source time function

$$S^T(t) = M_0 \frac{t}{T^2} \exp\left(-\frac{t}{T}\right) , \qquad (2.13)$$

where the smoothness parameter $T = 0.1$ s controls the frequency content and amplitude of the source time function. As the source signal does not have a dominant frequency we use the maximum frequency of the signal which is defined to be 5 Hz. The considered receiver is located at $(x_r, y_r, z_r) = (6 \text{ km}, 8 \text{ km}, 0)$ at the free surface. Thus, the propagation distance from the source to the receiver is about 10 km, i.e., 5 km in the halfspace and 5 km in the surface layer. Therefore, the total propagation distance is about 20 wavelengths for the wave with the shortest wavelength and the time-window for the receiver is 0-9 s.

We set the desired accuracy to EM $\leq 10\%$, which automatically should provide

	WP2_LOH1			WP2_LOH3		
	$\mathcal{O}4$	$\mathcal{O}5$	$\mathcal{O}6$	$\mathcal{O}4$	$\mathcal{O}5$	$\mathcal{O}6$
$\mathrm{EM}_r[\%]$	5.8	4.7	6.2	7.0	6.5	7.4
$\mathrm{PM}_r[\%]$	1.7	1.4	1.7	2.8	2.9	2.8
$\mathrm{EM}_t[\%]$	6.3	5.0	5.9	5.1	5.2	5.1
$\mathrm{PM}_t[\%]$	1.2	1.3	1.0	1.2	1.1	1.5
$\mathrm{EM}_v[\%]$	3.0	3.0	3.7	4.9	4.6	5.2
$\mathrm{PM}_v[\%]$	1.4	1.1	1.4	2.7	2.7	2.6

Table 2.1: *Misfits of the radial (EM_r, PM_r), transversal (EM_t, PM_t) and vertical (EM_v, PM_v) velocity components for the WP2_LOH1 and WP2_LOH3 test cases.*
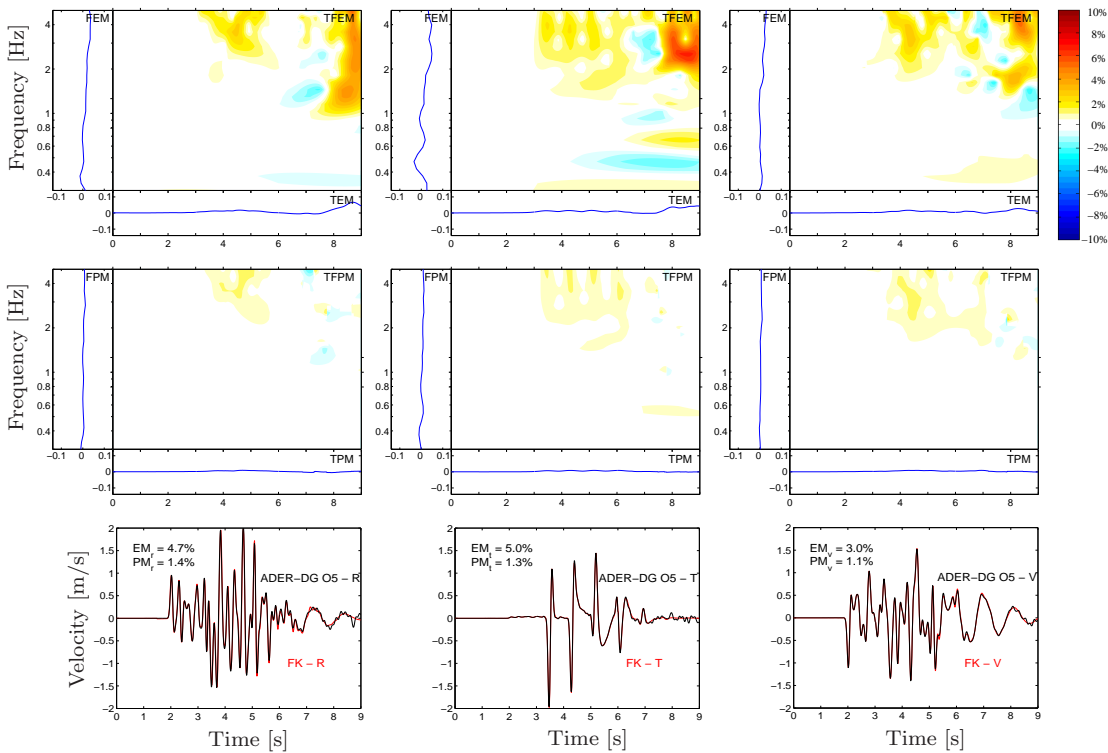

Figure 2.13: *Time-frequency representation of the misfits of the radial (left), transversal (middle) and vertical (right) components of the velocity seismograms for the WP2_LOH1 case. The comparison of the numerical (ADER-DG $\mathcal{O}5$, black) and the analytical (FK, red) seismograms is shown at the bottom together with their single-valued EM and PM.*

a smaller PM. Therewith, we can extract from Fig. 2.10 that we need 2.8, 1.8, or 1.4 elements per shortest wavelength for the estimated propagation distance when using an ADER-DG $\mathcal{O}4$, $\mathcal{O}5$, or $\mathcal{O}6$ scheme, respectively. Therefore, we generate three different tetrahedral meshes for three computations with the different approximation orders. The tetrahedra used by the ADER-DG $\mathcal{O}4$ scheme have an average edge length of 145 m in the layer and 250 m in the halfspace according to our analysis. The mesh spacings for the ADER-DG $\mathcal{O}5$ scheme are 225 m and 390 m and for the ADER-DG $\mathcal{O}6$ scheme 290 m and 500 m. The EM and PM of the obtained velocity seismograms with respect to the analytic frequency-wavenumber (FK) solutions [58] for the radial, transversal, and vertical components are given in Table 2.1. As expected, the values of the PM are always smaller than those of the EM. Furthermore, all misfits are clearly below the required 10%, which is due to the consideration of the maximum frequency of 5 Hz in the setup. The dominant frequency of the signal, however, is lower and therefore explains the better results. The important fact is that the three computations of different orders give basically the same accuracy, which confirms that our accuracy analysis and the accordingly chosen mesh spacings are correct. In Fig. 2.13 we show the TFR of the EM and PM (TFEM, TFPM) for the three components obtained with the ADER-DG $\mathcal{O}5$ scheme together with the comparison of the numerical and analytical seismogram in the time domain. Additionally, the time-dependent TEM and TPM (see Eq. (2.7)) as well as the frequency-dependent FEM and FPM (see Eq. (2.8)) are illustrated as the projection of the TFEM and the TFPM. The TFR of the misfits are shown in analogy to Figs. 7 and 8 of the work of Kristeková *et al.* [21]. Note, however, that the range of our color scale and our misfit axes only span $\pm10\%$ compared to $\pm40\%$ used by Kristeková *et al.* [21]. Even though this comparison shows that our results are more accurate, one has to consider that these reference solutions [21] might not be the present-day results. Furthermore, there are no CPU-time comparisons available. It is obvious that in our case the largest misfits occur towards the end of the numerical seismogram at high frequencies and the EM is much larger than the PM. Other investigations [61] showed that this is due to the non-perfect absorbing boundary conditions that introduce spurious reflections after around 6 s and therefore significantly contributes to the EM and PM values.

2.4.2   WP2_LOH3

In a further example, we apply the same three ADER-DG schemes with their corresponding tetrahedral meshes to the WP2_LOH3 test case, which has the same model setup as WP2_LOH1 but includes viscoelastic attenuation in the two materials. The damping factors inside the layer are $Q_p = 40$ for P-waves and $Q_s = 120$ for S-waves; within the halfspace underneath the damping factors are $Q_p = 69.3$ and $Q_s = 155.9$. This allows us to compare our results directly with those presented by Kristeková *et al.* [21]. The analytical solutions are again provided by the frequency-wavenumber (FK) method [62]. The misfit values are given in Table 2.1. Compared to the WP2_LOH1 case, the errors are slightly larger for the radial and vertical components but remain similar for the transversal component. However, even for viscoelastic wave propagation our parameter setup with respect to the required accuracy is still valid. The TFR of the misfits obtained by the ADER-DG $\mathcal{O}5$ scheme for the three velocity components are shown in Fig. 2.14 in analogy to Figs. 7 and 8 of [21]. Again, the range of our color scale and our misfit axes only spans $\pm10\%$. Furthermore, the ADER-DG scheme shows clearly lower misfits in the high frequency band above $3\,\mathrm{Hz}$ than the methods compared by Kristeková *et al.* [21]. In particular, the PM values in Fig. 2.14 are very low compared to the EM and can even hardly be seen at this scale for the transversal component. The actual seismic traces at the bottom of Fig. 2.14 show visual differences mainly towards the end after about $6\,\mathrm{s}$. However, the TFR, especially of the EM, discovers amplitude problems basically throughout the whole duration of the seismogram also in the low frequency range. This seems to be similar, however much weaker in comparison to the results obtained by WCC1 (Robert Graves, URS Corporation) and CMUN (Jacobo Bielak, Carnegie-Mellon University) presented by Kristeková *et al.* [21].

2.5   Discussion

We presented a quantitative accuracy analysis for the ADER-DG scheme for the simulation of seismic wave propagation on tetrahedral and hexahedral meshes. We evaluated the interaction of the approximation order of the numerical scheme, the mesh spacing of the used discretization and the propagation distance of the waves based on the time-frequency representation of the seismogram misfits. The results are obtained by a systematic variation of the different parameters on
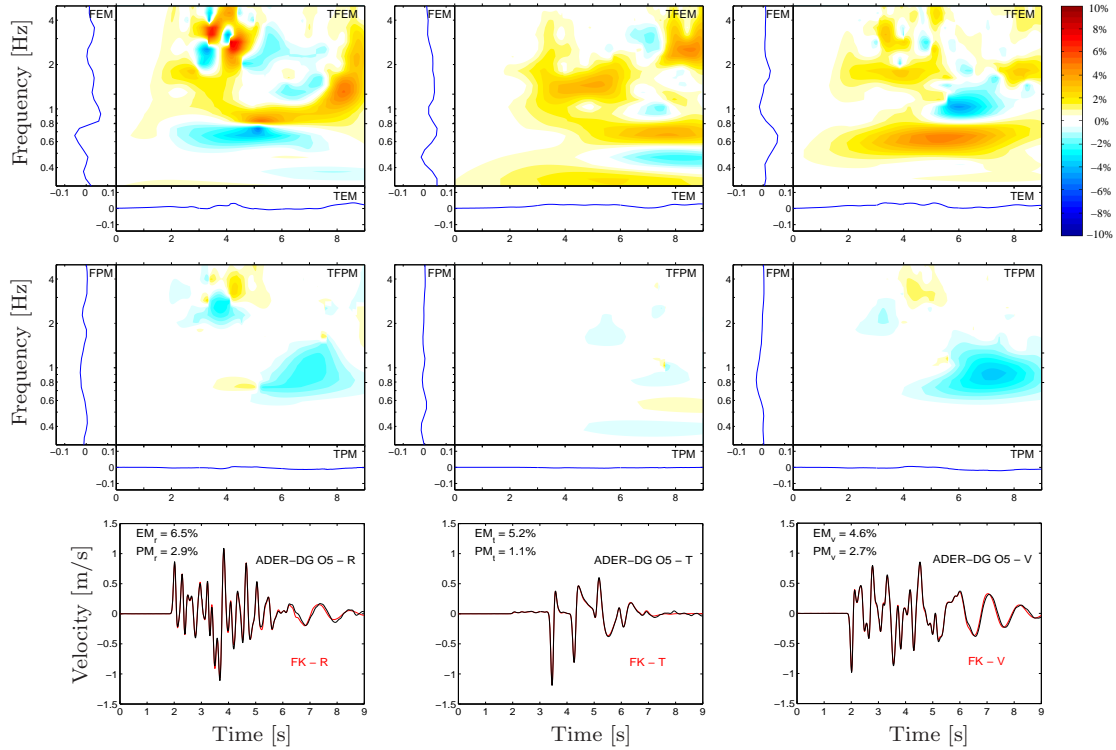
Figure 2.14: *Time-frequency representation of the misfits of the radial (left), transversal (middle) and vertical (right) components of the velocity seismograms for the WP2_LOH3 case. The comparison of the numerical (ADER-DG 𝒪5, black) and the analytical (FK, red) seismograms is shown at the bottom together with their single-valued EM and PM.*

a simplified but 3-D test model. The outcome of the analysis, mainly summarized in Fig. 2.10, serves as a guideline for choosing the correct modeling parameters with respect to a required accuracy limit. Hereby, we found that for the ADER-DG method the phase accuracy is always higher than the amplitude accuracy. Furthermore, we conclude that in general, the use of the higher approximation orders in combination with coarser meshes is preferable as the reduction in the number of mesh elements dominates the increased cost per element and therefore reduces the total computation time. However, geometrical constraints such as a rough surface topography or internal structure, might often prohibit the use of very coarse meshes and determine a certain mesh spacing that has to be used. Therefore, our study gives a clear relationship between the used mesh spacing, the expected propagation distance, the desired amplitude and phase accuracy, and the finally chosen approximation order.

Another main result coming out of this study is the different CPU time required by tetrahedral and hexahedral meshes. As shown in Fig. 2.11, it is much faster to compute on hexahedral meshes than on tetrahedral meshes to reach a desired accuracy (up to a factor of 36!). However, as already indicated, it is not always possible to use hexahedral meshes in a practicable way whenever the model includes complicated geological structures or complex topography. In such cases, for a suitable sampling of the geometry, we would have to use an enormously fine mesh spacing for hexahedrons or strongly deformed hexahedrons which drastically increases the computational costs. On top of that, it is one of the greatest conveniences of the ADER-DG method that it runs on unstructured tetrahedral meshes being extremely flexible with respect to complex geometries and allowing very fast mesh generation.

In summary, we can conclude, that it would be an excellent upgrade for the ADER-DG method if we could combine both element types within one mesh. We want to apply tetrahedrons to regions of complicated structures and fill up the rest of the computational domain with hexahedrons. In this manner, we can save runtime by using as few elements as possible and simultaneously we allow precise discretization while keeping the meshing process simple. This merging of different mesh types has already been performed for 2D simulations in this work and will be discussed in detail in the next chapter.

The practical use of our analysis study is validated through the application of our results to the well-acknowledged test cases WP2_LOH1 and WP2_LOH3 of the SPICE code validation project including heterogeneous elastic material, free surface boundary conditions and also viscoelastic attenuation. It is obvious that the main contribution to the misfit emerges at the end of the seismogram, when boundary effects become crucial. To overcome this drawback of the up to now used absorbing boundary conditions, we deal with an alternative solution for non-reflecting boundaries in Chap. 4.

For both test cases defining a desired accuracy limit and simulating the wave propagation for a specified distance but using different meshes led to the same expected results as the required approximation scheme could be chosen correctly. We emphasize the importance of such tools, as there is already a considerable amount of numerical methods available which become more and more sophisticated and whose computational implementations and efficiencies differ from each other. Therefore, it is difficult for a single scientist or group to use them all to their full capacity. A collective effort, where developers and experts of the various methods provide solutions to some established test cases, could clarify the picture

of how the different approaches perform and how they compare to each other. A number of test cases, analytical and reference solutions, including those of the ADER-DG method, are already available at www.nuquake.eu/SPICECVal. The different contributions create a database, where a comprehensive overview of the capabilities of contemporary methods for seismic wave propagation is offered to the rest of the seismological community.

Chapter 3

Non-conforming, Hybrid Meshes

Today research in seismology often depends on appropriate computational methods to model particular wave phenomena with sufficient accuracy. Additionally, with the increasing computational resources more realistic scenarios can be modeled and investigations can be carried out with higher resolution. The ADER-DG method has the advantage, that it can be formulated with arbitrary high-orders of accuracy in space and time, while at the same time unstructured meshes can be used to model complex geometries. However, regarding the CPU time, it turns out to be more efficient to compute on regular meshes instead of unstructured ones to reach a desired error level (see Chap. 2). Therefore, the performance of the ADER-DG method can be increased by combining different mesh types, i.e., creating hybrid meshes, similarly to certain FE methods [22, 23] or to the combination of FE and FD methods [63].

Furthermore, the mesh spacing - and therefore the possible time step for explicit time stepping schemes - is usually determinated by the shortest wave length to be propagated. In fact, when waves propagate through different materials, their wave lengths might change and it is suitable to adapt the mesh spacing to the local velocity structure in order to optimize accuracy with respect to run time. Therefore, we formulate an ADER-DG scheme for 2D simulations that achieves high-order approximation properties on hybrid meshes consisting of regular quadrilateral and unstructured triangular elements where appropriate. In this context we also introduce a straight forward refinement and coarsening strategy for velocity-adapted, purely quadrilateral meshes. However, this procedure leads to non-conforming element interfaces. To this end, the presented ADER-DG scheme is able to treat both, hybrid meshes and non-conforming interfaces, using the same numerical

methodology. Furthermore, this work serves as a feasibility study to analyze the correctness and performance of this new ADER-DG approach before extending it to tetrahedral and hexahedral meshes in three space dimensions. In this case, non-conformity of the mesh will be necessary in order to avoid pyramids as an additional element type that links tetrahedral with hexahedral meshes.

Following [64] we first reformulate the ADER-DG method focusing on the necessary changes in the flux computation across interfaces between adjacent elements which are needed to handle non-conforming boundaries. Then we present information on the parallelization strategy related to this new type of model discretization based on non-conforming, hybrid meshes. Afterwards, we show results of convergence tests to validate the parallel implementation of our scheme and present two different numerical examples of seismic wave propagation problems. Finally, we illustrate an application to a scenario including real data information in the area of the city of Grenoble.

3.1   The Altered Numerical Scheme

Since we implement non-conforming, hybrid meshes in two space dimensions for the present, we shortly introduce the 2D equations of the ADER-DG scheme. The governing equation reads

$$\frac{\partial Q_p}{\partial t} + A_{pq}\frac{\partial Q_q}{\partial x} + B_{pq}\frac{\partial Q_q}{\partial y} = S_p\,, \tag{3.1}$$

where $\mathbf{Q}$ is the vector of the $p = 5$ unknown variables

$$\mathbf{Q} = \{\sigma_{xx}, \sigma_{yy}, \sigma_{xy}, u, v\}^T\,. \tag{3.2}$$

Now, the matrices $A_{pq} = A_{pq}(\mathbf{x})$ and $B_{pq} = B_{pq}(\mathbf{x})$ are reduced to

$$\mathbf{A} = \begin{pmatrix} 0 & 0 & 0 & -(\lambda + 2\mu) & 0 \\ 0 & 0 & 0 & -\lambda & 0 \\ 0 & 0 & 0 & 0 & -\mu \\ -\frac{1}{\rho} & 0 & 0 & 0 & 0 \\ 0 & 0 & -\frac{1}{\rho} & 0 & 0 \end{pmatrix} \tag{3.3}$$
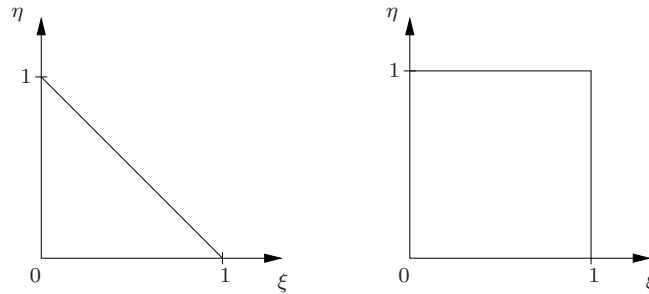
Figure 3.1: *Definition of the triangular reference element $\mathcal{E}_T$ (left) and the quadrilateral reference element $\mathcal{E}_Q$ (right) in the local $\xi\eta$-coordinate system.*

and

$$\mathbf{B} = \begin{pmatrix} 0 & 0 & 0 & 0 & -\lambda \\ 0 & 0 & 0 & 0 & -(\lambda + 2\mu) \\ 0 & 0 & 0 & -\mu & 0 \\ 0 & 0 & -\frac{1}{\rho} & 0 & 0 \\ 0 & -\frac{1}{\rho} & 0 & 0 & 0 \end{pmatrix}, \tag{3.4}$$

with $p, q = 1, \ldots, 5$. $S_p = S_p(\mathbf{x}, t)$ is the source vector again.

Solving the elastic wave equation (Eq. 3.1) on hybrid meshes we have to encounter different element types within the numerical scheme. For 2D simulations we comprise triangulars and quadrilaterals for the discretization of the computational domain. The particular reference elements in the local $\xi\eta$-coordinate system are illustrated in Fig. 3.1. Recalling the basic steps of the ADER-DG method (see Sec. 1.3), the first essential modification appears for the basis functions $\Phi_l(\xi, \eta)$ defined in reference space. From now on they depend on the element type of the particular element $\mathcal{E}^{(m)}$ as given in App. A and we introduce the following notation to distinguish them as

$$\Phi_l(\xi, \eta) = \begin{cases} \Theta_l(\xi, \eta) & \text{if} \quad \mathcal{E} = \mathcal{E}_T \quad \text{(element type is triangular)}, \\ \Psi_l(\xi, \eta) & \text{if} \quad \mathcal{E} = \mathcal{E}_Q \quad \text{(element type is quadrilateral)}. \end{cases} \tag{3.5}$$

For simplification, we will use the general notation $\mathcal{E}$ for an element and Φ for the basis functions in the following. Therefore, depending on the particular element type the corresponding basis functions have to be substituted.

Going further through the derivation of the ADER-DG scheme as in Sec. 1.3.2, we want to mention that also for the multiplication of the governing equation by a test function Φ_k (see Eq. (1.13)), the test function Φ_k has to be chosen from the same space as the basis functions Φ_l for the numerical approximation of

the vector $\mathbf{Q}_h$ in Eq. (1.10) depending on the particular element type. Now, we can use the same scheme as explicated in Sec. 1.3 with one sole exception: the flux term (see Eq. (1.15)), which exchanges information across element interfaces $\partial\mathcal{E}^{(m)}$ in order to extrapolate the numerical solution of stresses and velocities from one time level to the next one using an explicit time step scheme. For a 2D computation the flux term reads

$$
\int_{\partial\mathcal{E}^{(m)}} \Phi_k F_p^h \, \mathrm{d}S \;\; = \;\; \sum_{j=1}^{s} \frac{1}{2} T_{pq}^{(j)} \left(A_{qr}^{(m)} + |A_{qr}^{(m)}| \right) (T_{rs}^{(j)})^{-1} |\mathbf{S}^{(j)}| \, \hat{Q}_{sl}^{(m)} F_{kl}^{(j),0}
$$

$$
+ \;\; \sum_{j=1}^{s} \frac{1}{2} T_{pq}^{(j)} \left(A_{qr}^{(m)} - |A_{qr}^{(m)}| \right) (T_{rs}^{(j)})^{-1} |\mathbf{S}^{(j)}| \, \hat{Q}_{sl}^{(m_j)} F_{kl}^{(j),i} , \quad (3.6)
$$

with the so-called flux matrices

$$
F_{kl}^{(j),0} = \int_0^1 \Phi_k^{(m)} \Phi_l^{(m)} d\chi \tag{3.7}
$$

and

$$
F_{kl}^{(j),i} = \int_0^1 \Phi_k^{(m)} \Phi_l^{(m_j)} d\chi \tag{3.8}
$$

where we integrate over the unit interval $\chi \in [0,1]$ and therefore introduce the length of the j-th edge $|\mathbf{S}^{(j)}|$ in Eq. (3.6). T_{pq} and T_{pq}^{-1} are the transformation matrix and its inverse for the rotation to the edge-aligned coordinate system, which in 2D are given by

$$
\mathbf{T} \;\; = \;\; \begin{pmatrix} n_x^2 & n_y^2 & -2n_x n_y & 0 & 0 \\ n_y^2 & n_x^2 & 2n_x n_y & 0 & 0 \\ n_x n_y & -n_x n_y & n_x^2 - n_y^2 & 0 & 0 \\ 0 & 0 & 0 & n_x & -n_y \\ 0 & 0 & 0 & n_y & n_x \end{pmatrix} \tag{3.9}
$$

and

$$
(\mathbf{T})^{-1} \;\; = \;\; \begin{pmatrix} n_x^2 & n_y^2 & 2n_x n_y & 0 & 0 \\ n_y^2 & n_x^2 & -2n_x n_y & 0 & 0 \\ -n_x n_y & n_x n_y & n_x^2 - n_y^2 & 0 & 0 \\ 0 & 0 & 0 & n_x & n_y \\ 0 & 0 & 0 & -n_y & n_x \end{pmatrix} . \tag{3.10}
$$

In Eq. (3.7) the superscript 0 denotes, that the integral uses test functions $\Phi_k^{(m)}$ and basis functions $\Phi_l^{(m)}$ from the same element (m) and local edge (j). These integrals can be computed exactly in a preprocessing step and stored in the s different flux matrices $F_{kl}^{(j),0}$, with $j = 1, ..., s$, for later flux calculations. So for triangular elements there are $s = 3$, for quadrilaterals $s = 4$ matrices to store, while the size of these square matrices depends on the number L of basis functions used and therefore on the order of the DG scheme, i.e., the degree N of the approximation polynomials. This relation is given by $L = (N+1)(N+2)/2$ and therefore $k, l = 0, ..., L - 1$. As $F_{kl}^{(j),0}$ only contains information of the element (m) itself, we can compute the outgoing flux given by the first line in Eq. (3.6) for the non-conforming, hybrid meshes in exactly the same way as in previous DG approaches. We just have to make sure that the appropriate functions Φ are used according to the element type.

If we consider the incoming flux given by the second line in Eq. (3.6) the situation is slightly more complicated. The index i in Eq. (3.8) is the local index of the edge of the adjacent element (m_j). In previous formulations of our ADER-DG schemes the entire mesh has to consist of one element type and the meshes have to be conforming. In that case, two adjacent elements always share exactly one entire edge between two element vertices and the matrices given by Eq. (3.8) can be computed exactly via a preprocessing step and stored for later flux calculations. In total there are s^2 matrices of size $L \times L$ to store as each of the s edges of an element (m) can share one of the s edges of the adjacent element (m_j). Nevertheless, the storage of these few and rather small matrices is negligible compared to the storage requirement of the degrees of freedom $\hat{Q}_{pl}^{(m)}$ for all elements in the computational domain.

Now, in the case of non-conforming boundaries as shown in Fig. 3.2, two adjacent elements do not have to share exactly one common edge. Therefore, the flux matrices in Eq. (3.8) involving neighbor information have to be computed differently.

In fact, we calculate these integrals numerically by using Gauss-Legendre integration with a sufficiently high number of Gaussian integration points along the edge (j) of element (m) that ensures the exact integration of the product of the two polynomial basis functions Φ. This is achieved by

$$\int_0^1 \Phi_k^{(m)} \Phi_l^{(m_j)} d\chi = \sum_{c=1}^{N+1} \Phi_k^{(m)}(\xi_c, \eta_c) \Phi_l^{(m_j)}(\xi_c', \eta_c') w_c , \qquad (3.11)$$
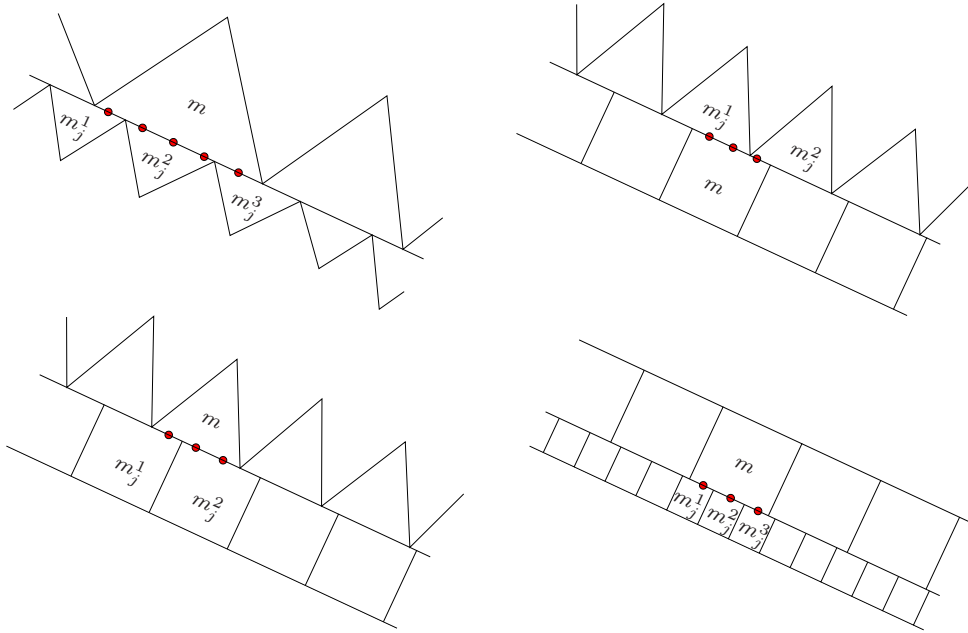
Figure 3.2: *Examples of non-conforming mesh coupling for purely triangular, purely quadrilateral or hybrid meshes. In all different cases, the numerical flux entering an element (m) over its edge (j) can be determined by Gauss-Legendre integration. This integration involves all adjacent elements (m_j^ν), that include a Gaussian integration point along edge (j) of element (m).*

with N being the polynomial degree of the used basis functions Φ, (ξ_c, η_c) and (ξ'_c, η'_c) the reference coordinates of the Gaussian integration points in the elements (m) and (m_j), respectively, and w_c the Gaussian weights.

According to Eq. (3.5), there are basically four different combinations of element pairs for such non-conforming, hybrid meshes as shown in Fig. 3.2. Explicitly, this can lead to the following products of basis functions in Eq. (3.11) depending on the element types on either side of the interface: $\Psi_k^{(m)}\Psi_l^{(m_j)}$, $\Theta_k^{(m)}\Theta_l^{(m_j)}$, $\Psi_k^{(m)}\Theta_l^{(m_j)}$, and $\Theta_k^{(m)}\Psi_l^{(m_j)}$. In contrast to conforming meshes, the number of neighboring elements across non-conforming boundaries can be larger than one. The exact number is determined by the locations of Gaussian integration points. As shown in Fig. 3.2 each Gaussian point might fall into a different neighbor or several Gaussian points might fall into the same neighbor. This variation in the number of neighbors also affects the amount of information to be communicated from one processor to another in the case of parallel computing, if the non-conforming interface happens to be a boundary between two partitions of the computational

mesh. Therefore, we present a brief description of our parallelization strategy in the following.

3.2 Parallelization of Non-conforming Hybrid Meshes

Concerning the parallelization of the ADER-DG method it is only the numerical flux that requires information from neighboring elements. Similar to the ADER-DG scheme working with conforming meshes [19], we need the time-integrated degrees of freedom $\hat{Q}_{sl}^{(m_j)}$ and the basis functions $\Phi_l^{(m_j)}$ of the neighbor element for computing the flux over an edge (j) according to Eq. (3.6). For non-conforming, hybrid meshes, we now might have one or more neighboring elements across a non-conforming interface and it is possible, that some or even all of these neighbors do not belong to the same subdomain due to mesh partitioning. Therefore, the neighbor search carried out in a preprocessing step is based on the location of the Gaussian integration points used for flux integration. In the case of more than one neighbor across one edge the amount of MPI communication increases compared to conforming meshes. However, this increase in communication is negligible with respect to the computation time. Furthermore, in the mesh partitioning process non-conforming meshes have to be treated slightly different from conforming ones. As we are using the METIS software package [65] to partition a mesh we have to partition the conforming triangular and quadrilateral parts of the hybrid mesh separately into the desired number of MPI subdomains that are then processed by different CPUs. In order to reduce the length of internal MPI-boundaries between different subdomains, we try to connect separate subdomains by minimizing the distances of their centers of gravity, which we approximate by the sum of all element barycenters of the subdomain divided by the corresponding number of elements belonging to this subdomain. We remark, that this connection approach only works well for rather small numbers of subdomains. However, it does not significantly affect the efficiency of the scheme, if the total number of elements inside a subdomain is large compared to the number of elements at the MPI boundary. For a visual example of the mesh partitioning strategy we refer to the following section of numerical tests. Nevertheless, it might be worth testing other mesh partitioners with respect to their capabilities of partitioning non-conforming, hybrid meshes more efficiently.

3.3   Results and Applications

In the following, we present the convergence results for the implementation of our new ADER-DG approach with non-conforming, hybrid meshes and show several applications to check its practicability and examine its performance.

3.3.1   Convergence Tests

By performing a numerical convergence test, we validate the expected order of approximation and the implementation of the modified scheme for non-conforming, hybrid meshes. To this end, we solve the two-dimensional homogeneous elastic wave equation (Eq. (3.1)) for $S_p(\mathbf{x}, t) = 0$ on a square shaped domain $\Omega = [-1, 1] \times [-1, 1] \in \mathbb{R}^2$ with periodic boundaries. We consider the initial condition

$$\mathbf{Q}_0 = \mathbf{Q}(\mathbf{x}, 0) = \mathbf{R}_2^{A_n} \sin(k \cdot \mathbf{x}) + \mathbf{R}_5^{A_n} \sin(k \cdot \mathbf{x}), \qquad (3.12)$$

with the wave number

$$k = (k_x, k_y)^T = \frac{2\pi}{25}(1, 1)^T. \qquad (3.13)$$

The vectors $\mathbf{R}_2^{A_n}$ and $\mathbf{R}_5^{A_n}$ denote the second and the fifth right eigenvectors of the normal Jacobian $\mathbf{A}$ in Eq. (3.3) oriented in direction $\mathbf{n} = (1, 1)^T$ normal to the wave front. Therefore, the initial condition Eq. (3.12) creates a plane sinusoidal P-wave traveling along the diagonal direction of Ω and a plane sinusoidal S-wave traveling into the opposite direction.

Throughout the computational domain Ω we use homogeneous material parameters, i.e., Lamé constants $\lambda = 2$ and $\mu = 1$, and density $\rho = 1$, leading to the constant wave propagation velocities $c_p = 2$ and $c_s = 1$ for the P- and S-wave, respectively. The final simulation time T is set to $T = 20\sqrt{2}$, such that the exact solution $\mathbf{Q}_e$ at simulation time $t = T$ is given by the initial condition, i.e., $\mathbf{Q}_e(\mathbf{x}, T) = \mathbf{Q}_0$. This way, the P- and S-wave travel 40 and 20 times, respectively, through the computational domain. The computations are performed on a sequence of 12 non-conforming, hybrid meshes (see Fig. 3.3). We use the following notation: Mesh k, with $k = 4s$, $s = 1, ..., 12$ contains k quadrilateral elements along each boundary of Ω leading to mesh spacings $\Delta h_s = 2/k$. Therefore, the mesh spacings Δh_s cover a range from $\Delta h_1 = 0.5$ to $\Delta h_{12} = 0.0417$. The spacing of the triangular mesh scales with the same factors.

We then compute the errors for all components of the numerical solution $(Q_s)_p$
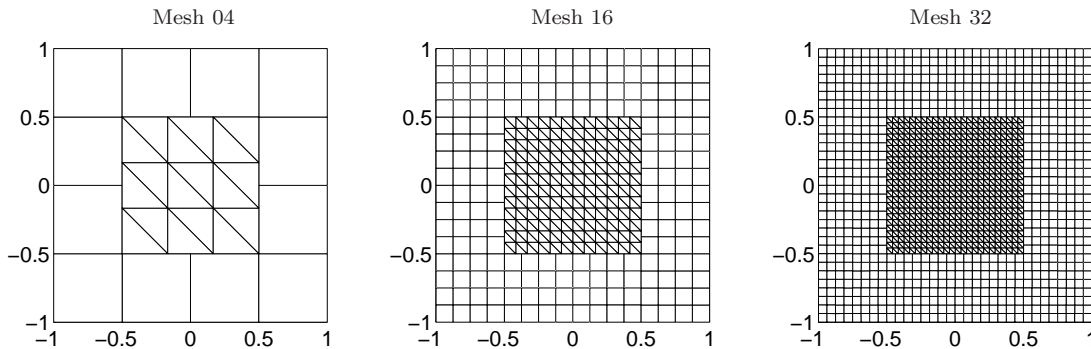
Figure 3.3: *Three of the 12 different meshes for convergence tests showing successive refinements of the triangular and quadrilateral elements. All meshes are hybrid meshes with non-conforming interfaces between two mesh types.*

in the L^∞ and in the L^2 norm, given by

$$\mathbf{E}^s_{L^\infty} = \max_\Omega |\mathbf{Q}_s - \mathbf{Q}_e| \tag{3.14}$$

and

$$\mathbf{E}^s_{L^2} = \sqrt{\sum_\Omega |\mathbf{Q}_s - \mathbf{Q}_e|^2}\,, \tag{3.15}$$

where index s denotes the numerical solution depending on the mesh spacing. The numerical convergence orders $\mathcal{O}_{L^\infty}$ and $\mathcal{O}_{L^2}$ can then be determined by two successively refined meshes and the convergence order is computed via

$$\mathcal{O}_{L^\infty} = \log\Big(\frac{E^s_{L^\infty}}{E^{s-1}_{L^\infty}}\Big) \big/ \log\Big(\frac{\Delta h_s}{\Delta h_{s-1}}\Big) \tag{3.16}$$

for an arbitrarily chosen component of the solution vector $\mathbf{Q}_s$. Tab. 3.1 shows the errors for σ_{xx} measured by Eq. (3.14) and Eq. (3.15) together with the convergence orders, total number N_d of degrees of freedom, and the required CPU time for running the code on 4 processors of the SGI Altix 4700 (HLRB II) of the Leibniz-Rechenzentrum.

In Fig. 3.4 we illustrate the results in the L^∞ norm in dependence of the degrees of freedom, the mesh spacing Δh and the CPU time. It is clear from Tab. 3.1 that our implementation of the ADER-DG schemes reaches the expected convergence orders even on non-conforming, hybrid meshes. Furthermore, Fig. 3.4 shows that the errors decrease with refining the mesh or increasing the order of polynomials as we have already seen when discussing the accuracy analysis in Sec. 2.3

Δh	E_{L^∞}	$\mathcal{O}_{L^\infty}$	E_{L^2}	$\mathcal{O}_{L^2}$	N_d	CPU [s]
$7.14 \cdot 10^{-2}$	$2.6354 \cdot 10^{0}$	$-$	$3.6131 \cdot 10^{0}$	$-$	4410	$2.90 \cdot 10^{2}$
$6.25 \cdot 10^{-2}$	$2.2751 \cdot 10^{0}$	0.8	$3.1501 \cdot 10^{0}$	0.8	5760	$3.43 \cdot 10^{2}$
$5.00 \cdot 10^{-2}$	$1.5622 \cdot 10^{0}$	2.4	$2.2096 \cdot 10^{0}$	2.3	9000	$7.51 \cdot 10^{2}$
$4.17 \cdot 10^{-2}$	$1.0490 \cdot 10^{0}$	3.0	$1.5245 \cdot 10^{0}$	2.8	12960	$1.35 \cdot 10^{3}$
$1.00 \cdot 10^{-1}$	$2.4524 \cdot 10^{-1}$	$-$	$3.5994 \cdot 10^{-1}$	$-$	4500	$2.11 \cdot 10^{2}$
$8.33 \cdot 10^{-2}$	$1.2126 \cdot 10^{-1}$	3.9	$1.8288 \cdot 10^{-1}$	3.7	6480	$3.61 \cdot 10^{2}$
$7.14 \cdot 10^{-2}$	$6.7487 \cdot 10^{-2}$	3.8	$1.0307 \cdot 10^{-1}$	3.7	8820	$5.44 \cdot 10^{2}$
$6.25 \cdot 10^{-2}$	$4.0985 \cdot 10^{-2}$	3.7	$6.4898 \cdot 10^{-2}$	3.5	11520	$8.44 \cdot 10^{2}$
$1.67 \cdot 10^{-1}$	$8.0675 \cdot 10^{-2}$	$-$	$1.4083 \cdot 10^{-1}$	$-$	2700	$1.05 \cdot 10^{2}$
$1.25 \cdot 10^{-1}$	$1.6277 \cdot 10^{-2}$	5.6	$3.3277 \cdot 10^{-2}$	5.0	4800	$1.86 \cdot 10^{2}$
$1.00 \cdot 10^{-1}$	$5.0019 \cdot 10^{-3}$	5.3	$1.2019 \cdot 10^{-2}$	4.6	7500	$3.51 \cdot 10^{2}$
$8.33 \cdot 10^{-2}$	$2.0084 \cdot 10^{-3}$	5.0	$5.4290 \cdot 10^{-3}$	4.4	10800	$5.68 \cdot 10^{2}$
$7.14 \cdot 10^{-2}$	$9.6098 \cdot 10^{-4}$	4.8	$2.7815 \cdot 10^{-3}$	4.3	14700	$9.19 \cdot 10^{2}$
$2.50 \cdot 10^{-1}$	$2.9958 \cdot 10^{-2}$	$-$	$7.2238 \cdot 10^{-2}$	$-$	1800	$5.27 \cdot 10^{1}$
$1.67 \cdot 10^{-1}$	$1.7515 \cdot 10^{-3}$	7.0	$6.3241 \cdot 10^{-3}$	6.0	4050	$1.63 \cdot 10^{2}$
$1.25 \cdot 10^{-1}$	$3.5419 \cdot 10^{-4}$	5.6	$1.3255 \cdot 10^{-3}$	5.4	7200	$3.38 \cdot 10^{2}$
$1.00 \cdot 10^{-1}$	$1.1372 \cdot 10^{-4}$	5.1	$4.2085 \cdot 10^{-4}$	5.1	11250	$7.10 \cdot 10^{2}$
$2.50 \cdot 10^{-1}$	$9.3617 \cdot 10^{-4}$	$-$	$5.0878 \cdot 10^{-3}$	$-$	2520	$1.03 \cdot 10^{2}$
$1.67 \cdot 10^{-1}$	$1.0519 \cdot 10^{-4}$	5.4	$5.4015 \cdot 10^{-4}$	5.5	5670	$3.33 \cdot 10^{2}$
$1.25 \cdot 10^{-1}$	$1.8534 \cdot 10^{-5}$	6.0	$1.1989 \cdot 10^{-4}$	5.2	10080	$6.84 \cdot 10^{2}$
$1.00 \cdot 10^{-1}$	$4.1622 \cdot 10^{-6}$	6.7	$3.4222 \cdot 10^{-4}$	5.6	15750	$2.70 \cdot 10^{3}$
$2.50 \cdot 10^{-1}$	$6.9493 \cdot 10^{-5}$	$-$	$6.8803 \cdot 10^{-4}$	$-$	3360	$2.74 \cdot 10^{2}$
$1.67 \cdot 10^{-1}$	$4.3120 \cdot 10^{-6}$	6.9	$3.7859 \cdot 10^{-5}$	7.2	7560	$8.82 \cdot 10^{2}$
$1.25 \cdot 10^{-1}$	$5.8470 \cdot 10^{-7}$	6.9	$5.0051 \cdot 10^{-6}$	7.0	13440	$1.78 \cdot 10^{3}$
$1.00 \cdot 10^{-1}$	$1.2294 \cdot 10^{-7}$	7.0	$1.1322 \cdot 10^{-6}$	6.7	21000	$3.61 \cdot 10^{3}$
$2.50 \cdot 10^{-1}$	$8.4521 \cdot 10^{-6}$	$-$	$6.8741 \cdot 10^{-5}$	$-$	4320	$5.08 \cdot 10^{2}$
$1.67 \cdot 10^{-1}$	$3.8038 \cdot 10^{-7}$	7.6	$3.1907 \cdot 10^{-6}$	7.6	9720	$1.67 \cdot 10^{3}$
$1.25 \cdot 10^{-1}$	$3.8508 \cdot 10^{-8}$	8.0	$4.0066 \cdot 10^{-7}$	7.2	17280	$3.19 \cdot 10^{3}$
$1.00 \cdot 10^{-1}$	$6.8260 \cdot 10^{-9}$	7.8	$6.6945 \cdot 10^{-8}$	8.0	27000	$6.39 \cdot 10^{3}$
$2.50 \cdot 10^{-1}$	$6.1153 \cdot 10^{-7}$	$-$	$7.0857 \cdot 10^{-6}$	$-$	5400	$8.02 \cdot 10^{2}$
$1.67 \cdot 10^{-1}$	$1.6421 \cdot 10^{-8}$	8.9	$1.8870 \cdot 10^{-7}$	8.9	12150	$4.31 \cdot 10^{3}$
$1.25 \cdot 10^{-1}$	$1.2834 \cdot 10^{-9}$	8.9	$1.7835 \cdot 10^{-8}$	8.2	21600	$8.49 \cdot 10^{3}$

Table 3.1: *Errors and convergence rates of σ_{xx}, degrees of freedom, and CPU-times from ADER-DG schemes of order $\mathcal{O}2$ to $\mathcal{O}9$ on non-conforming, hybrid meshes.*

on conforming meshes. It is important to note that for a particular accuracy level the total number of degrees of freedom is always less for higher-order schemes. This number depends on the amount of elements and the approximation order and is directly proportional to the required computer storage. In addition, it is generally faster to reach a certain accuracy level by using high-order schemes on coarse meshes. Therewith it is clear, that all the results obtained in Chap. 2 also hold for the ADER-DG scheme on non-conforming, hybrid meshes.

3.3.2 Homogeneous Material

After validating the convergence properties of the new ADER-DG scheme on non-conforming, hybrid meshes we test its accuracy for a typical wave propagation problem and compare the results to those obtained by the previous ADER-DG method on a conforming mesh as well as to an independent SEM method. For this test case we again take a square shaped domain $\Omega = [-1, 1] \times [-1, 1] \in \mathbb{R}^2$ and use homogeneous material parameters $\lambda = 1$, $\mu = 1$, and $\rho = 1$ of an ideal Poisson solid. This way, possibly occurring numerical artifacts can only be caused by the transition of waves through the non-conforming mesh boundaries. As source term we put a single force acting in x-direction at position $(0.31, -0.35)$ with a Ricker-pulse source time function of 8 Hz dominant frequency (see Sec. 1.4). A receiver, located at $(-0.8, 0.0)$, registers the passing P-wave and S-wave during a 3 s simulation. The non-conforming mesh is illustrated in Fig. 3.5. It contains boundaries between non-conforming, hybrid meshes as well as non-conforming boundaries between equal mesh types. The coarsest mesh spacing of $\Delta h = 0.06$ is taken for the innermost area. The conforming mesh used for the ADER-DG reference solution only consists of quadrilaterals of $\Delta h = 0.06$ which represents
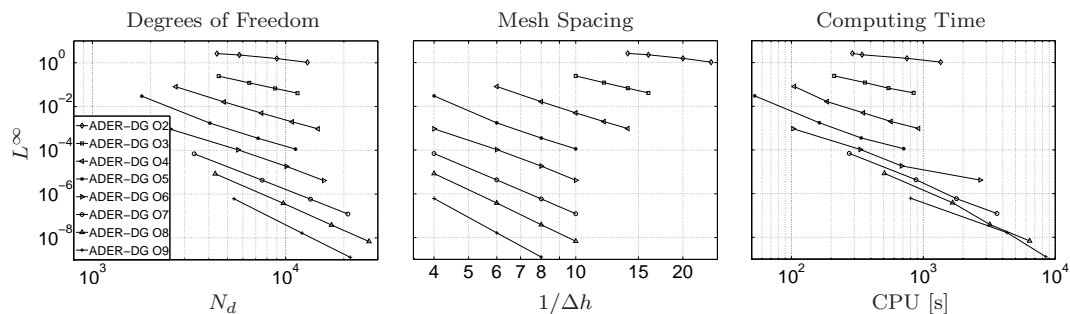

Figure 3.4: *Errors in L_∞ norm in dependence of degrees of freedom, mesh spacing and CPU time on HLRB II.*
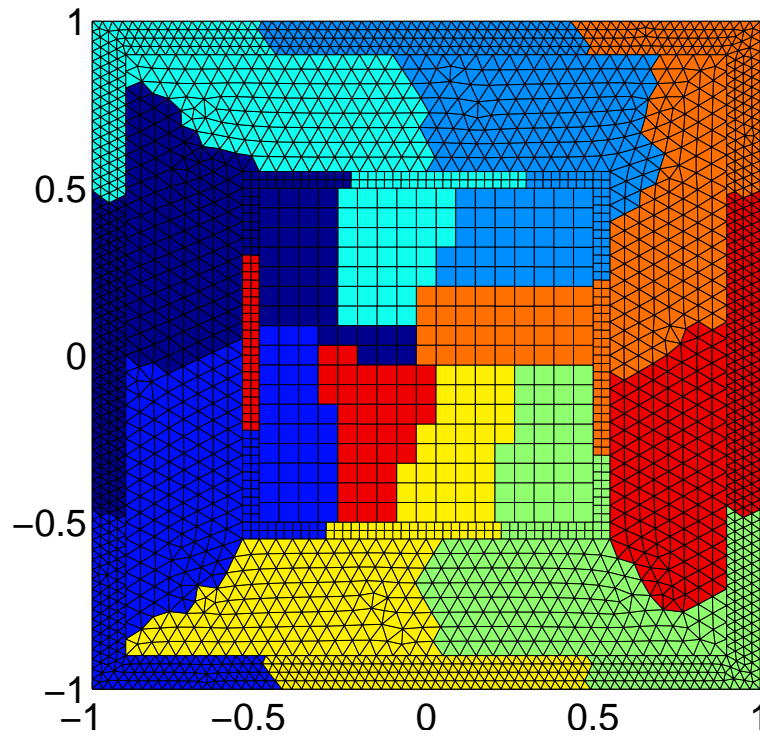
Figure 3.5: *Mesh of non-conforming boundaries including quadrangular-quadrangular, quadrangular-triangular and triangular-triangular interfaces.*
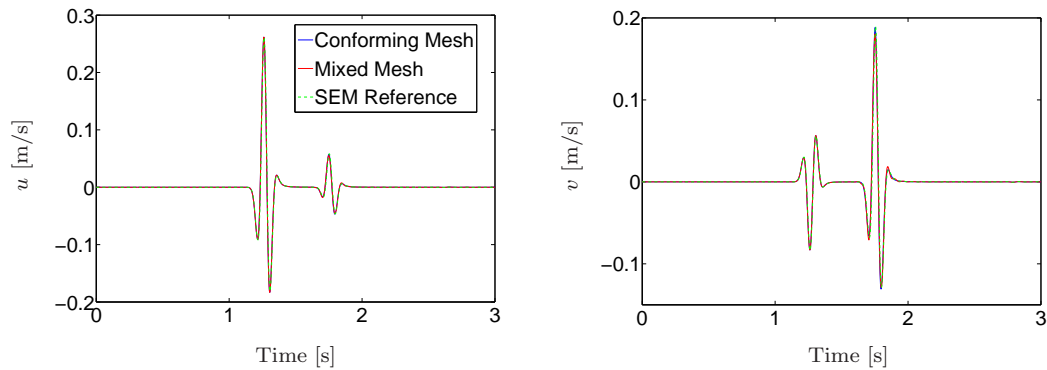

Figure 3.6: *Signals for the receiver located at $(-0.8, 0.0)$ computed on the conforming as well as the non-conforming mesh as a comparison with SEM results.*

about half the S-wavelength. Thus, a simulation with an approximation order 6 provides sufficient accuracy [66].

The differently colored elements in Fig. 3.5 show the 8 subdomains for the parallel computation. As explained in Section. 3.2 the partitioning routine attempts to assemble neighboring subdomains of different zones. Starting with the dark blue part of processor 1 it performs well. However, combining the red parts for processor 8 does not permit any more freedom and the residual subdomains of each zone have to be gathered.

Fig. 3.6 shows plots of the velocity components u and v in x- and y-direction, respectively, computed with the ADER-DG method on a non-conforming (red) and on a conforming (blue) mesh as well as an independent reference solution obtained by spectral elements on a regular quadrilateral mesh (dashed green). The comparison shows a visually perfect match between all signals and no numerical artifacts appear due the the non-conforming boundaries that the waves propagate across. This further validates the correctness of our approach and implementation of our new ADER-DG scheme for non-conforming, hybrid meshes. In the following, we treat a more challenging problem of a thin surface layer which is particularly important in computational seismology.

3.3.3   Thin Layer

Here, we present the performance of the proposed scheme in comparison to the previous approach with conforming meshes for a more sophisticated test case, which considers a strong material change between a thin surface layer and an elastic half space as presented similarly in [67]. The thin layer significantly influences the seismic wave field even if its thickness is small compared to the wave length. We use the computational domain $\Omega = [0, 35] \times [-15, 0]\,\mathrm{km}^2$ and a single force with a Ricker pulse of peak frequency $2\,\mathrm{Hz}$ acting in x-direction at $(15, -0.2)\,\mathrm{km}$ as source time function. We put one receiver on the free surface at $(25, 0)\,\mathrm{km}$ and the other one into the half space at $(25, -2)\,\mathrm{km}$. The elastic parameters of the only $20\,\mathrm{m}$ thick surface layer and the underlying elastic half space are given in Tab. 3.2. The wave velocities in the half space are 2.8 times faster than in the thin low-velocity surface layer. Note that the dominant S-wave length in the half space is $707\,\mathrm{m}$ and therefore about 35 times larger than the layer thickness. To solve the problem with sufficient resolution [66] with an ADER-DG scheme of order $\mathcal{O}6$ in space and time we choose an element edge length of $80\,\mathrm{m}$ in the thin layer, corresponding to about three elements per dominant S-wave length in

Zone	$\rho\,[kg/m^3]$	$\mu\,[Pa]$	$\lambda\,[Pa]$	$c_p\,[m/s]$	$c_s\,[m/s]$
Thin Layer	2000	$5.0e^8$	$5.0e^8$	866	500
Half Space	2500	$5.0e^9$	$5.0e^9$	2449	1414

Table 3.2: *Definition of the elastic material parameters for the thin layer test case.*

Mesh	# of Elements	Time Step [s]	Restrictive Layer	Run-time [s]
CF	13540	$4.15 \cdot 10^{-4}$	Half Space	6737
NC	10010	$5.52 \cdot 10^{-4}$	Thin Layer	4881

Table 3.3: *Comparison of the conforming (CF) and non-conforming (NC) meshes for the thin layer test case computed on 8 processors.*

this layer. However, due to the thickness of only 20 m of the layer, that has to be respected by the mesh, the triangular elements are slightly elongated as shown in the zoomed parts of Fig. 3.7. We also see the difference of the two meshes in the connection of the thin layer to the half space. While the conforming mesh has to adapt its elements in the high velocity half space to the finely meshed interface, the non-conforming mesh allows for a mesh spacing proportional to the velocity structure immediately below the interface between the two layers. This leads to a reduction of the number of mesh elements, an increase in the possible time step length, and therefore a reduction of 27% in total simulation time as summarized in Tab. 3.3. It is interesting that in the conforming mesh the time step is restricted by the high wave velocity and the small elements directly below the material interface in the half space. The elements could be chosen larger from an accuracy point of view but the mesh conformity forces them to be small at the interface. By contrast, in the non-conforming approach the time step is restricted by the small elements in the thin layer which is due to the physics and geometry of the problem. The domain below 2 km basically serves as an enlargement to avoid any possible effects from the boundaries. Therefore, both the conforming and the non-conforming mesh are identical below 2 km and are gradually coarsened to keep the computational cost low. Furthermore, we compute the same test case with a SEM code of spatial accuracy $\mathcal{O}6$ and time accuracy $\mathcal{O}2$ on a regular quadrilateral mesh with 20 m mesh spacing due to the thin layer.

The results in form of seismograms at the two receivers are presented in Fig. 3.8. Visually all three methods provide the same solutions. The strong
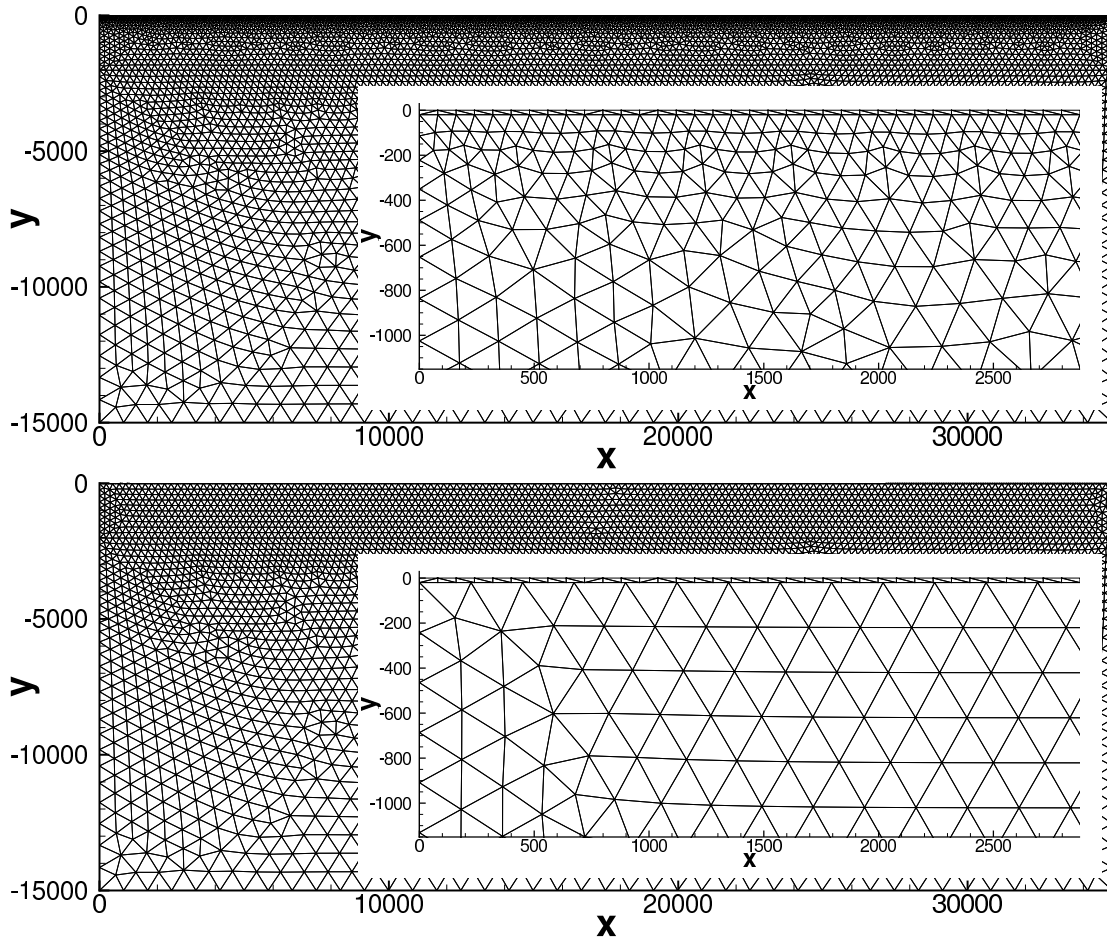
Figure 3.7: *Meshes for thin layer test case with their zoomed sections to visualize the thin layer. Top: the conforming mesh, where the mesh spacing gradually grows from 80 m to 225 m. Bottom: the non-conforming mesh with a sudden change in mesh spacing from 80 m to 225 m.*

Rayleigh wave at the free surface receiver induces some slight differences between the ADER-DG solutions and the independent SEM reference, which is due to its extremely high resolution using the regular 20 m mesh leading to 1312500 elements. However, we only detect a small amplitude misfit in this surface wave, while the phases and all other waves fit perfectly.

In addition, we computed the same test case with the conforming mesh, but treating the element edges at the material interface as non-conforming to estimate the computational overhead due to the point-wise Gaussian flux integration Eq. (3.11) in comparison to the precomputed flux matrices Eq. (3.8). The computational overhead seems to be negligible as the computing time due
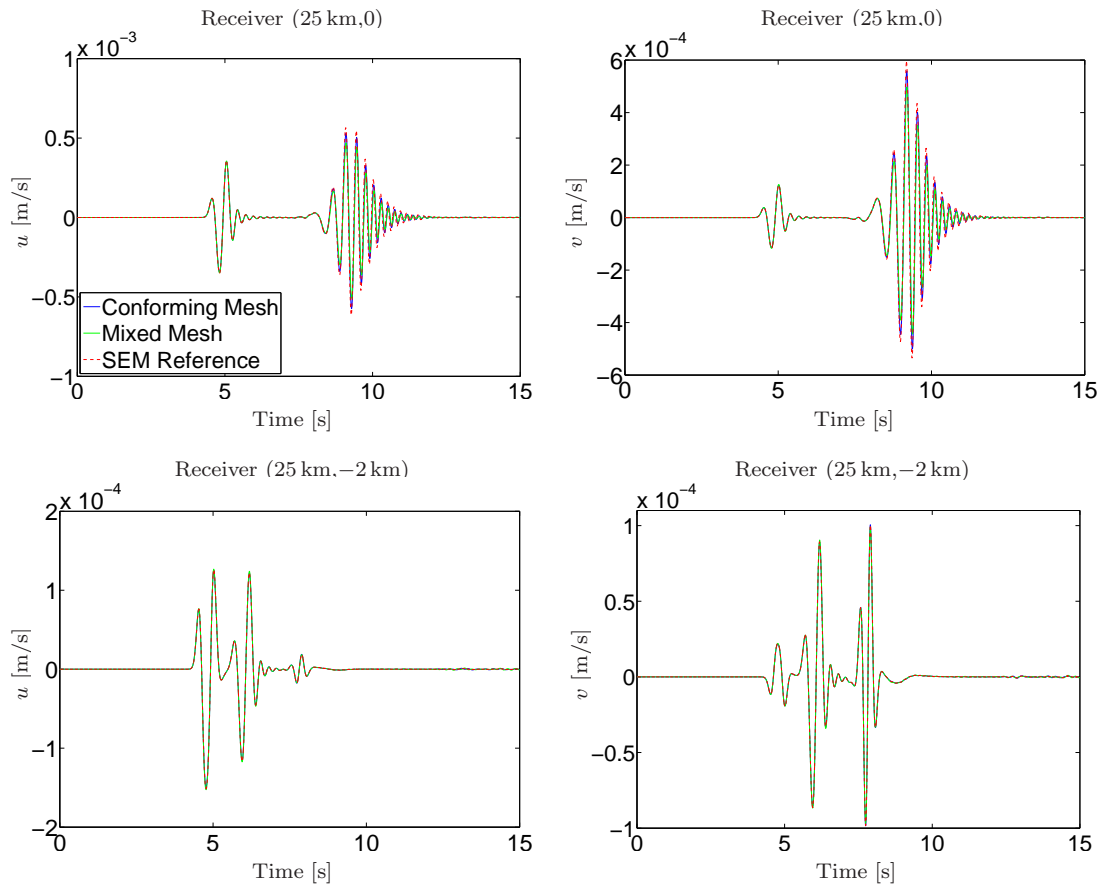
Figure 3.8: *Seismograms of the horizontal and vertical velocity components u and v, respectively, of ground motion at the two receivers. The receiver at the surface (top) shows a clear and highly oscillating Rayleigh wave arriving after the direct wave. The buried receiver (bottom) exhibits the direct P-wave and the interference of surface-reflected P- and S-waves.*

to the non-conforming treatment of the conforming mesh increased only by 0.8%. For truly non-conforming meshes this increase is clearly dominated by the reduction of the computational cost due to a smaller number of elements and the possible increase of the time step. Therefore, the new ADER-DG method for non-conforming meshes seems to be particularly suited for such challenging wave propagation problems and gives additional flexibility as shown in the following more realistic example.
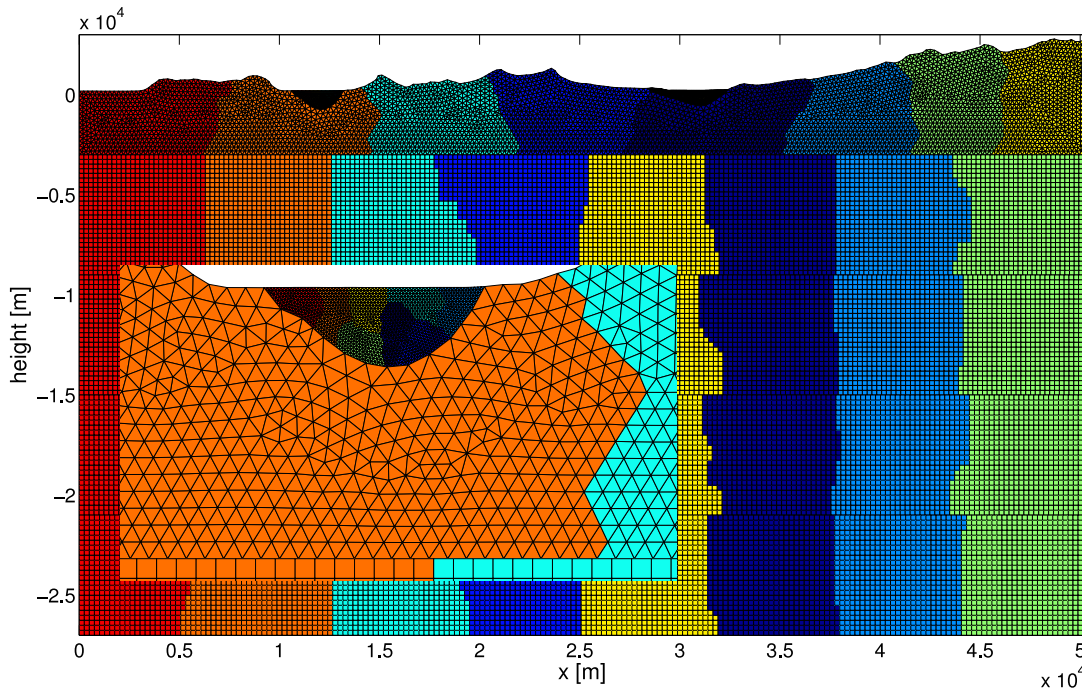
Figure 3.9: *Non-conforming, hybrid mesh for the wave propagation scenario of Grenoble with strongly variable material. Each color indicates the mesh partition handled by one of the eight processors.*

3.3.4   Grenoble - 2D

In this example we apply the new ADER-DG scheme on a more realistic scenario based on a modified benchmark [68]. We are simulating seismic wave propagation in an east-west cross-section north of the city of Grenoble using 50 km width, 27 km depth and 3 km height to include the mountain topography. This 2D section is shown in Fig. 3.9 and cuts through two valleys filled with alluvial sediments. The wave speeds in these two basin structures are extremely slow compared to the surrounding solid bedrock as shown by the material parameters in Tab. 3.4. To account for the very slow wave speeds in the basin, we apply an extremely fine mesh on them which is visualized in the zoomed section in Fig. 3.9. Generating the mesh that adapts to the free surface topography and the two basin-bedrock interfaces has been achieved with a triangular mesh of varying mesh spacing. With increasing velocities in the deeper layers we adjust the mesh spacing of the quadrilaterals non-conformingly, but proportionally to the velocity structure to achieve an optimally large time step length. In Fig. 3.9 we show the

Zone	$\rho\,[\text{kg/m}^3]$	$\mu\,[\text{Pa}]$	$\lambda\,[\text{Pa}]$	$c_p\,[\text{m/s}]$	$c_s\,[\text{m/s}]$
Basin 1 (west)	$2.2 \cdot 10^3$	$7.0 \cdot 10^8$	$4.8 \cdot 10^9$	$1.7 \cdot 10^3$	$5.7 \cdot 10^2$
Basin 2 (east)	$2.1 \cdot 10^3$	$1.9 \cdot 10^8$	$4.1 \cdot 10^9$	$1.5 \cdot 10^3$	$3.0 \cdot 10^2$
Layer 1	$2.7 \cdot 10^3$	$3.0 \cdot 10^{10}$	$3.0 \cdot 10^{10}$	$5.8 \cdot 10^3$	$3.3 \cdot 10^3$
Layer 2	$2.7 \cdot 10^3$	$3.3 \cdot 10^{10}$	$3.3 \cdot 10^{10}$	$6.0 \cdot 10^3$	$3.5 \cdot 10^3$
Layer 3	$2.8 \cdot 10^3$	$3.6 \cdot 10^{10}$	$3.3 \cdot 10^{10}$	$6.2 \cdot 10^3$	$3.6 \cdot 10^3$
Layer 4	$2.8 \cdot 10^3$	$3.8 \cdot 10^{10}$	$3.8 \cdot 10^{10}$	$6.3 \cdot 10^3$	$3.7 \cdot 10^3$
Layer 5	$2.9 \cdot 10^3$	$4.1 \cdot 10^{10}$	$4.1 \cdot 10^{10}$	$6.5 \cdot 10^3$	$3.8 \cdot 10^3$

Table 3.4: *Material parameters for the east-west cross-section north of Grenoble. The computational domain is divided into seven zones, the two basins and five layers of bedrock.*

colored mesh partition for 8 processors. First it is applied to each of the different zones and afterwards different subdomains are gathered.

Again we use an explosive source with a Ricker pulse of $3\,\text{Hz}$ dominant frequency just below the Belledonne massif at location $(35, -2.5)\,\text{km}$. Fig. 3.10 illustrates snapshots for the horizontal velocity component of the seismic wave field at times $1.5\,\text{s}$, $3.0\,\text{s}$, $4.5\,\text{s}$, and $6.0\,\text{s}$. We observe the strong direct wave as well as reflected and converted waves from the free surface. In particular, there is a remarkable scattering of the seismic wave field due to the rough free surface topography. The maximum amplitude and longest duration of ground motion is obtained inside the basin as expected from the strong impedance contrast between the sediments and the bedrock. Looking especially at the downward propagating waves, no spurious numerical effects due to the non-conforming meshes can be detected, which confirms that the proposed ADER-DG scheme with its additional flexibility of non-conforming, hybrid meshes can be used for such modelling problems effectively.

3.4   Discussion

We introduced an extension of the high-order accurate ADER-DG method for non-conforming, hybrid meshes in two space dimensions. The key issue is the modified computation of the flux integral between adjacent elements that do not need to share a common edge. The applied point-wise Gaussian integration preserves the scheme's high approximation order in space and time as confirmed by numerical convergence tests up to 9th order. Tests on different wave propaga-
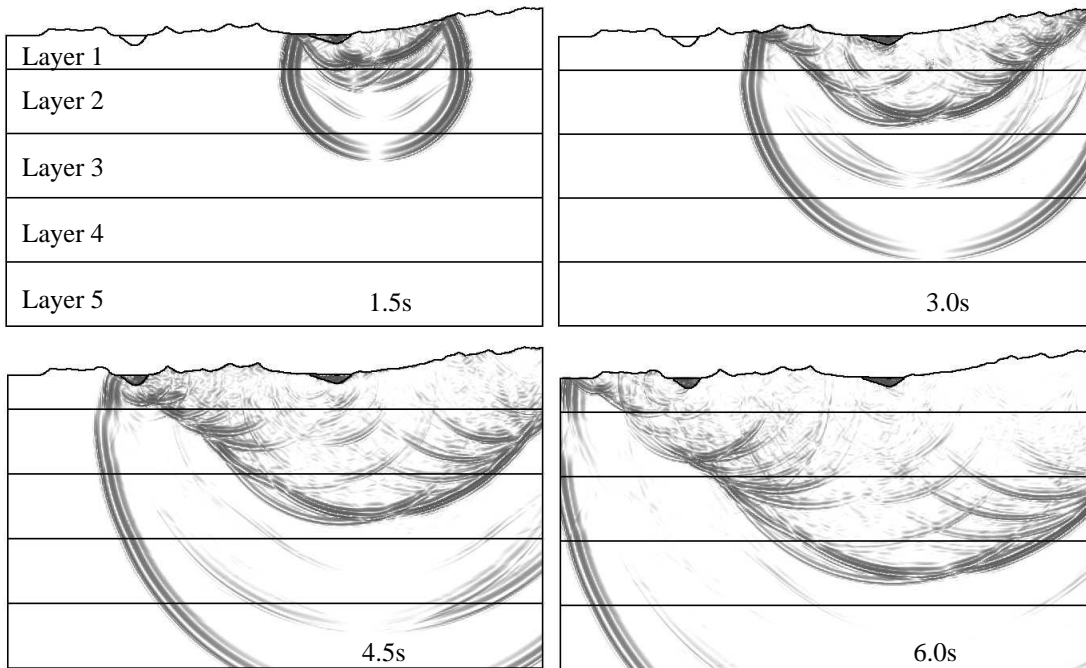
Figure 3.10: *Snapshots of the horizontal seismic velocity component u in the 2D section north of Grenoble for four different times. Note the strong scattering of the wave field due to the rough free surface topography.*

tion problems show an excellent agreement with reference solutions and can lead to a clear reduction in computational cost due to an optimal adaptation of the mesh spacing to the physical and geometrical properties of the problem. We do not observe numerical artifacts caused by the non-conformity of the mesh and provide a simple mesh refinement or coarsening strategy for regular quadrilateral meshes to use an optimal time step length. Also the parallel implementation of the ADER-DG approach for non-conforming unstructured meshes seems to perform well. The results are encouraging and promise to achieve similar or even larger benefits from the mesh coupling of tetrahedral and hexahedral elements in three space dimensions due to the much more efficient simulation on hexahedral meshes than on tetrahedral ones. However, this is subject to our current research and developments.

Chapter 4

Convolutional Perfectly Matched Layers

Solving a PDE numerically we have to truncate the computational domain artificially. One key issue is how to perform this truncation without introducing significant artifacts into the computation. Especially for wave propagation simulations this is a serious problem, as we usually encounter oscillating and only slowly decaying solutions. Therefore, we use absorbing boundary conditions (ABCs), introduced in Sec. 1.5, which should avoid reflections from the boundaries. However, ABCs only work perfectly for normal incidence of the waves and get worse for gracing incidence. According to our misfit analysis (Chap. 2) actually the main deficiency of seismograms results from spurious reflections from the boundaries. Thus, we want to find a more expedient way of avoiding this impact of artificial boundaries.

In 1994, Berenger [24] first introduced the perfectly matched layer (PML) for the absorption of electromagnetic waves. It is a layer surrounding the computational domain in which the waves are attenuated and decay exponentially. Bergenger overcame the problem of stepwise reflections by material changes (due to the damping profile) inside the layer. He split the magnetic field component into two space-dependent subcomponents of normal and tangential direction with respect to the outer boundary. Therewith, the absorption works perfectly with zero reflection for all angles of incidence and independent of frequency.
However, the method faces two essential problems: Firstly, from a mathematical point of view, the problem is no more strongly well-posed but only weakly well-posed, which means that small perturbations already can cause instabilities

[69]. Secondly, after discretization, the method suffers from reflections at grazing incidence again. To improve the behavior of the discrete PML at grazing incidence, Kozuoglu and Mittra [70] used the unsplit reformulation of Berenger's PML in terms of a complex coordinate stretching [71] and modified this classical PML by adding a frequency-dependent term. A novel implementation thereof was achieved by Roden and Gedney [25], where they could reduce the number of auxiliary variables. In the following we introduce this so-called convolutional perfectly matched layer (CPML) for the ADER-DG method step-by-step. We examine its performance with respect to CPU time and memory usage and critically look at difficulties concerning the stability of the code. Then we show some examples on the basis of test cases performed and published by Komatitsch and Tromp [72] and by Komatitsch and Martin [73] and finally we discuss our results.

4.1   The Extended Numerical Scheme with CPML

In order to avoid reflections from the outer boundary of the computational domain, the idea of the CPML is to surround the domain by a layer in which a kind of frequency- and space-dependent damping profile is applied to the waves. This can be performed by transforming the spacial differential operators of the governing equation (Eq. (3.1)) inside the layer. For a better understanding we explicitly show the linear hyperbolic system of differential equations:

$$
\begin{aligned}
\frac{\partial}{\partial t}\sigma_{xx} - (\lambda + 2\mu)\frac{\partial}{\partial x}u - \lambda\frac{\partial}{\partial y}v &= S_1\,, \\
\frac{\partial}{\partial t}\sigma_{yy} - \lambda\frac{\partial}{\partial x}u - (\lambda + 2\mu)\frac{\partial}{\partial y}v &= S_2\,, \\
\frac{\partial}{\partial t}\sigma_{xy} - \mu(\frac{\partial}{\partial x}v + \frac{\partial}{\partial y}u) &= S_3\,, \\
\rho\frac{\partial}{\partial t}u - \frac{\partial}{\partial x}\sigma_{xx} - \frac{\partial}{\partial y}\sigma_{xy} &= \rho S_4\,, \\
\rho\frac{\partial}{\partial t}v - \frac{\partial}{\partial x}\sigma_{xy} - \frac{\partial}{\partial y}\sigma_{yy} &= \rho S_5\,.
\end{aligned}
\tag{4.1}
$$

The transformed derivatives $\partial_{\tilde{x}}$ and $\partial_{\tilde{y}}$, determined to act inside the layer, are defined as

$$\begin{aligned}
\partial_{\tilde{x}} &\equiv \frac{1}{\kappa_x}\partial_x + \varphi_x(t) * \partial_x\,, \\
\partial_{\tilde{y}} &\equiv \frac{1}{\kappa_y}\partial_y + \varphi_y(t) * \partial_y\,.
\end{aligned} \tag{4.2}$$

The second term in each case denotes a convolution of the differential operator with the function φ_i, $i = x, y$, which reads

$$\varphi_i(t) \equiv -\frac{d_i}{\kappa_i^2}H(t)\,\mathrm{e}^{-\left(\frac{d_i}{\kappa_i}+\alpha_i\right)t}\,. \tag{4.3}$$

Here, $H(t)$ denotes the Heaviside function and usually we set $\kappa_i = 1$. The linear function α_i, defined inside the layer, goes from 0 to $\alpha_{\max} = \pi f_{\max}$, with $f_{\max}$ being the maximum frequency of the signal. The value 0 is assigned to the outer boundary of the domain and the maximum value refers to the interface between the inner domain and the layer. The damping function d_i is given by

$$d_i(r_i) = -\frac{3}{2\Delta}c_p \log\left(R_c\right)\left(\frac{r_i}{\Delta}\right)^2\,, \tag{4.4}$$

where Δ is the thickness of the layer and r_i marks the distance from the interface. Note, that d_i quadratically depends on the position r_i inside the layer. $R_c = 0.001$ denotes the theoretical reflection coefficient.

Before we apply the transformed operators of Eq. (4.2) to Eq. (4.1) we abbreviate the expressions by introducing new memory variables ϕ_{pi}, where $p = 1, \ldots, 5$ stands for each of the 5 elastic variables of vector $\mathbf{Q}$ (see Eq. (3.2)) and i refers to the directions of the derivatives. The memory variables are defined as

$$\phi_{pi} \equiv \varphi_i * \frac{\partial Q_p}{\partial i} = \int_0^t \varphi_i(t-\tau)\frac{\partial Q_p(\tau)}{\partial i}\,\mathrm{d}\tau\,. \tag{4.5}$$

Therewith, the linear hyperbolic system of Eq. (4.1), transformed inside the CPML, reads

$$
\frac{\partial}{\partial t}\sigma_{xx} - (\lambda + 2\mu)\left(\frac{1}{\kappa_x}\frac{\partial}{\partial x}u + \phi_{4x}\right) - \lambda\left(\frac{1}{\kappa_y}\frac{\partial}{\partial y}v + \phi_{5y}\right) = S_1\,,
$$

$$
\frac{\partial}{\partial t}\sigma_{yy} - \lambda\left(\frac{1}{\kappa_x}\frac{\partial}{\partial x}u + \phi_{4x}\right) - (\lambda + 2\mu)\left(\frac{1}{\kappa_y}\frac{\partial}{\partial y}v + \phi_{5y}\right) = S_2\,,
$$

$$
\frac{\partial}{\partial t}\sigma_{xy} - \mu\left(\frac{1}{\kappa_x}\frac{\partial}{\partial x}v + \phi_{5x}\right) - \mu\left(\frac{1}{\kappa_y}\frac{\partial}{\partial y}u + \phi_{4y}\right) = S_3\,,
$$

$$
\rho\frac{\partial}{\partial t}u - \left(\frac{1}{\kappa_x}\frac{\partial}{\partial x}\sigma_{xx} + \phi_{1x}\right) - \left(\frac{1}{\kappa_y}\frac{\partial}{\partial y}\sigma_{xy} + \phi_{3y}\right) = \rho S_4\,,
$$

$$
\rho\frac{\partial}{\partial t}v - \left(\frac{1}{\kappa_x}\frac{\partial}{\partial x}\sigma_{xy} + \phi_{3x}\right) - \left(\frac{1}{\kappa_y}\frac{\partial}{\partial y}\sigma_{yy} + \phi_{2y}\right) = \rho S_5\,, \quad (4.6)
$$

where only 8 of the 10 possible memory variables ϕ_{pi} are required. Within this modified scheme the amount of unknown variables has increased from 5 to 13. In order to gather the full scheme consisting of all 13 equations, we have to evolve the memory variables in time. The derivation yields

$$
\begin{aligned}
\frac{\partial \phi_{pi}}{\partial t} &= \frac{\partial}{\partial t}\left(\varphi_i * \frac{\partial Q_p}{\partial i}\right) \\[2mm]
&= \frac{\partial}{\partial t}\int_0^t -\frac{d_i}{\kappa_i^2}H(t-\tau)\,e^{-\left(\frac{d_i}{\kappa_i}+\alpha_i\right)(t-\tau)}\,\frac{\partial Q_p(\tau)}{\partial i}\,d\tau \\[2mm]
&= -\frac{d_i}{\kappa_i^2}\int_0^t \delta(t-\tau)\,e^{-\left(\frac{d_i}{\kappa_i}+\alpha_i\right)(t-\tau)}\,\frac{\partial Q_p(\tau)}{\partial i}\,d\tau \\[2mm]
&\quad - \left(\frac{d_i}{\kappa_i}+\alpha_i\right)\int_0^t -\frac{d_i}{\kappa_i^2}H(t-\tau)\,e^{-\left(\frac{d_i}{\kappa_i}+\alpha_i\right)(t-\tau)}\,\frac{\partial Q_p(\tau)}{\partial i}\,d\tau \\[2mm]
&= -\frac{d_i}{\kappa_i^2}\frac{\partial Q_p}{\partial i} - \left(\frac{d_i}{\kappa_i}+\alpha_i\right)\phi_{pi}\,. \quad (4.7)
\end{aligned}
$$

This expression describes the time evolution of the memory variables in a continuous form, which follows a standard partial differential equation. Therefore, we

can complete the modified scheme Eq. (4.6) with the remaining 8 equations:

$$\frac{\partial \phi_{1x}}{\partial t} + \frac{d_x}{\kappa_x^2}\frac{\partial \sigma_{xx}}{\partial x} + \left(\frac{d_x}{\kappa_x} + \alpha_x\right)\phi_{1x} = 0\,,$$

$$\frac{\partial \phi_{2y}}{\partial t} + \frac{d_y}{\kappa_y^2}\frac{\partial \sigma_{yy}}{\partial y} + \left(\frac{d_y}{\kappa_y} + \alpha_y\right)\phi_{2y} = 0\,,$$

$$\frac{\partial \phi_{3x}}{\partial t} + \frac{d_x}{\kappa_x^2}\frac{\partial \sigma_{xy}}{\partial x} + \left(\frac{d_x}{\kappa_x} + \alpha_x\right)\phi_{3x} = 0\,,$$

$$\frac{\partial \phi_{3y}}{\partial t} + \frac{d_y}{\kappa_y^2}\frac{\partial \sigma_{xy}}{\partial y} + \left(\frac{d_y}{\kappa_y} + \alpha_y\right)\phi_{3y} = 0\,,$$

$$\frac{\partial \phi_{4x}}{\partial t} + \frac{d_x}{\kappa_x^2}\frac{\partial u}{\partial x} + \left(\frac{d_x}{\kappa_x} + \alpha_x\right)\phi_{4x} = 0\,,$$

$$\frac{\partial \phi_{4y}}{\partial t} + \frac{d_y}{\kappa_y^2}\frac{\partial u}{\partial y} + \left(\frac{d_y}{\kappa_y} + \alpha_y\right)\phi_{4y} = 0\,,$$

$$\frac{\partial \phi_{5x}}{\partial t} + \frac{d_x}{\kappa_x^2}\frac{\partial v}{\partial x} + \left(\frac{d_x}{\kappa_x} + \alpha_x\right)\phi_{5x} = 0\,,$$

$$\frac{\partial \phi_{5y}}{\partial t} + \frac{d_y}{\kappa_y^2}\frac{\partial v}{\partial y} + \left(\frac{d_y}{\kappa_y} + \alpha_y\right)\phi_{5y} = 0\,. \tag{4.8}$$

Together, both systems of equations (Eqs. (4.6) and (4.8)) build a linear hyperbolic system with an additional reaction term $\tilde{\mathbf{E}}$, which can be written in matrix form

$$\frac{\partial \tilde{Q}_p}{\partial t} + \tilde{A}_{pq}\frac{\partial \tilde{Q}_q}{\partial x} + \tilde{B}_{pq}\frac{\partial \tilde{Q}_q}{\partial y} = \tilde{E}_{pq}\tilde{Q}_q + S_p\,, \tag{4.9}$$

where $\tilde{\mathbf{Q}}$ denotes the vector of 13 unknowns

$$\tilde{\mathbf{Q}} = (\sigma_{xx}, \sigma_{yy}, \sigma_{xy}, u, v, \phi_{1x}, \phi_{2y}, \phi_{3x}, \phi_{3y}, \phi_{4x}, \phi_{4y}, \phi_{5x}, \phi_{5y})^T\,. \tag{4.10}$$

$\tilde{\mathbf{A}}$ and $\tilde{\mathbf{B}}$ are 13×13 Jacobian matrices, given by

$$\tilde{\mathbf{A}} = \begin{bmatrix} \frac{1}{\kappa_x}\mathbf{A} & 0 \\ \mathbf{A}_d & 0 \end{bmatrix} \in \mathbb{R}^{13\times13}\,, \quad \tilde{\mathbf{B}} = \begin{bmatrix} \frac{1}{\kappa_y}\mathbf{B} & 0 \\ \mathbf{B}_d & 0 \end{bmatrix} \in \mathbb{R}^{13\times13}\,, \tag{4.11}$$

where $\mathbf{A}, \mathbf{B} \in \mathbb{R}^{5\times5}$ are the Jacobians of the purely elastic part as given inside the computational domain (see Eqs. (3.3) and (3.4)). The matrices $\mathbf{A}_d$ and $\mathbf{B}_d \in \mathbb{R}^{8\times5}$

have the structure

$$
\mathbf{A}_d =
\begin{pmatrix}
\frac{d_x}{\kappa_x^2} & 0 & 0 & 0 & 0 \\
0 & 0 & 0 & 0 & 0 \\
0 & 0 & \frac{d_x}{\kappa_x^2} & 0 & 0 \\
0 & 0 & 0 & 0 & 0 \\
0 & 0 & 0 & \frac{d_x}{\kappa_x^2} & 0 \\
0 & 0 & 0 & 0 & 0 \\
0 & 0 & 0 & 0 & \frac{d_x}{\kappa_x^2} \\
0 & 0 & 0 & 0 & 0
\end{pmatrix}
,\quad
\mathbf{B}_d =
\begin{pmatrix}
0 & 0 & 0 & 0 & 0 \\
0 & \frac{d_y}{\kappa_y^2} & 0 & 0 & 0 \\
0 & 0 & 0 & 0 & 0 \\
0 & 0 & \frac{d_y}{\kappa_y^2} & 0 & 0 \\
0 & 0 & 0 & 0 & 0 \\
0 & 0 & 0 & \frac{d_y}{\kappa_y^2} & 0 \\
0 & 0 & 0 & 0 & 0 \\
0 & 0 & 0 & 0 & \frac{d_y}{\kappa_y^2}
\end{pmatrix}
. \tag{4.12}
$$

The matrix $\tilde{\mathbf{E}}$ of Eq. (4.9) represents a reaction source which couples the memory variables to the original elastic system. It can be decomposed as

$$
\tilde{\mathbf{E}} =
\begin{bmatrix}
0 & \mathbf{E} \\
0 & \mathbf{E}_d
\end{bmatrix}
\in \mathbb{R}^{13 \times 13} , \tag{4.13}
$$

with

$$
\mathbf{E} =
\begin{pmatrix}
0 & 0 & 0 & 0 & \lambda + 2\mu & 0 & 0 & \lambda \\
0 & 0 & 0 & 0 & \lambda & 0 & 0 & \lambda + 2\mu \\
0 & 0 & 0 & 0 & 0 & \mu & \mu & 0 \\
\frac{1}{\rho} & 0 & 0 & \frac{1}{\rho} & 0 & 0 & 0 & 0 \\
0 & \frac{1}{\rho} & \frac{1}{\rho} & 0 & 0 & 0 & 0 & 0
\end{pmatrix}
\tag{4.14}
$$

and

$$
\mathbf{E}_d =
\begin{pmatrix}
-\beta_x & 0 & 0 & 0 & 0 & 0 & 0 & 0 \\
0 & -\beta_y & 0 & 0 & 0 & 0 & 0 & 0 \\
0 & 0 & -\beta_x & 0 & 0 & 0 & 0 & 0 \\
0 & 0 & 0 & -\beta_y & 0 & 0 & 0 & 0 \\
0 & 0 & 0 & 0 & -\beta_x & 0 & 0 & 0 \\
0 & 0 & 0 & 0 & 0 & -\beta_y & 0 & 0 \\
0 & 0 & 0 & 0 & 0 & 0 & -\beta_x & 0 \\
0 & 0 & 0 & 0 & 0 & 0 & 0 & -\beta_y
\end{pmatrix}
, \tag{4.15}
$$

where $\beta_i = \frac{d_i}{\kappa_i} + \alpha_i$, $i = x, y$.

Summarizing, we can solve the hyperbolic differential equation inside the convolutional perfectly matched layer in exactly the same way as inside the computational domain, with the only difference, that we now have a system of 13 equations.

Note, that the outer boundary of the CPML is still treated like an absorbing boundary in terms of Sec. 1.5, which means, that in fact, the CPML is a combination of the damping layer and ABCs.

Concerning the memory usage of the scheme applied to a CPML we look at the degrees of freedom (DOF), given by

$$ \text{DOF} = L \times (\text{\# of variables}) \times (\text{\# of elements}) , \qquad (4.16) $$

where L denotes the number of basis functions (see Sec. 1.3.1). The number of variables inside the layer increases by 8. Therewith the total augmentation of degrees of freedom depends on the number of elements inside the layer. Assuming the layer to cover 10% of the computational domain, we arrive at a 16% higher memory requirement. Similar dependencies are expected for the CPU time which we consider for the test cases.

4.2   Stability Study

Although there exist some reports [74, 25] of successful applications of the CPML methodology, it turned out that it sometimes suffers from emerging instabilities. The problem for the original split scheme as well as for the unsplit CPML method is, that the extended system loses its strong well-posedness. This means that the modified scheme is no longer symmetric hyperbolic, i.e., $\tilde{\mathbf{A}}$ and $\tilde{\mathbf{B}}$ cannot be symmetrized simultaneously [69]. Therefore, the so-called ill-posedness can cause emerging instabilities due to small perturbations.

Studying the characteristics of this labile system seems to be quite demanding. According to Martin, Komatitsch and Ezziani [75], the simulation remains stable for a long time but non-physical waves and numerical instabilities or dispersion can appear. Marcinkovich and Olsen [76] report about problems only in special 3D cases and try to avoid instabilities by smoothing the media. They detect some numerical noise as soon as the source is placed close to the layer and suggest to keep distance for at least 5 grid points. To achieve higher stability, Festa, Delavaud and Vilotte [77] introduce a frequency cut-off and overdamping. However, applying this modification causes a dispersion error in the signals. Hu [78] claims, that instabilities are angle dependent, caused by waves of positive group and negative phase velocity and associates unstable modes with high wave numbers. In order to delay the instability, Simone and Hesthom [79] stepwise decrease

the degree of the polynomials but still see longterm instabilities. One of the latest publications by Quasimov and Tsynkov [80] seems to be quite promising, but their stabilization technique only works for an odd number of space dimensions. For our implementation we performed several parameter studies. We examined different frequencies, changed the distance between source and interface and between receiver and interface, created a couple of meshes of different element type and varying mesh spacing and altered the thickness of the layer. However, we cannot determine a general dependency on parameterization for the behavior of instabilities.

As applying the CPML makes the scheme instable per definition, we have to control the characteristics of the numerical simulation. Therefore, we keep track of the kinetic energy $E_{\mathrm{kin}} \sim (u^2 + v^2)$ inside the domain, which is not allowed to grow as soon as there is no more physical energy production, e.g. due to source terms. In case E_{kin} increases within a couple of timesteps, we switch off the modification of the scheme inside the layer and further compute using the original absorbing boundary conditions as before (see Sec. 1.5).

4.3   Results

In order to validate our implementation of the CPML for the ADER-DG scheme, we perform three test cases. We want to examine the performance of the CPML concerning spurious reflections at the artificial boundaries of the computational domain and confirm our way to superwise stability. The first two test cases are suggested by Komatitsch and Tromp [72] and hence called KoTro1 and KoTro2. The third one is named KoMa as it was first computed by Komatitsch and Martin [73].

4.3.1   KoTro1

To illustrate the efficiency of the CPML system, we simulate the propagation of P-SV waves in a 2D elastic isotropic homogeneous medium following the test case of Komatitsch and Tromp [72] who developed the PML formulation for the second-order seismic wave equation.
The computational domain is given by $\Omega = [0, 15] \times [0, 60]\,\mathrm{m}^2$ containing a $\Delta = 2.5\,\mathrm{m}$ thick damping layer which counts 10 elements for a given mesh spacing of
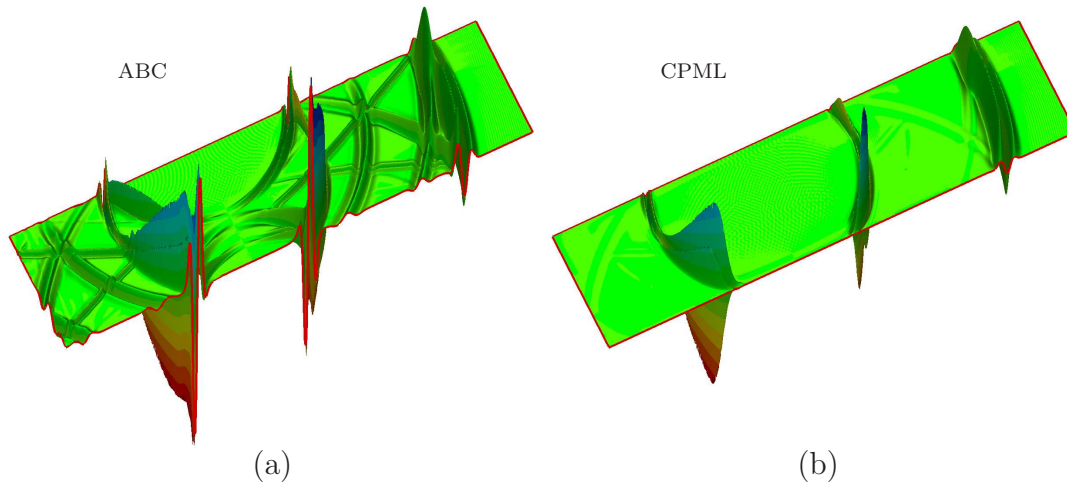
Figure 4.1: *Test case KoTro1: Snapshots of velocity u after 0.016 s simulation for (a) absorbing boundary conditions and (b) a convolutional perfectly matched layer.*

$\Delta h = 0.25$ m. The material parameters are $c_p = 2000\,\mathrm{ms}^{-1}$, $c_s = 880\,\mathrm{ms}^{-1}$ and $\rho = 2200\,\mathrm{kgm}^{-3}$ leading to a Poisson's ratio of $\nu = 0.38$. Again, we use a Ricker wavelet (see Sec. 1.4) as source time function. The dominant frequency is set to $f_0 = 900$ Hz and the source is located at $(4.5, 24)$ m not very far from the interface between the inner computational domain and the damping layer. The receiver is put even closer to the CPML, located at $(12, 33)$ m. For the simulation we use an $\mathcal{O}5$ scheme corresponding to polynomial degree 4. The total simulation time is $T = 25$ ms.

For the sake of comparability we take exactly the same model setup but without the CPML and compute the test case using common ABCs. In Fig. 4.1 we illustrate the results as snapshots of the velocity u after 0.016 s propagation time. It is obvious that there arise enormous reflections from the boundary in case (a) where purely ABCs are used. At grazing incidence the deficiencies are most significant and only for normal incidence the ABCs work perfectly. Fig. 4.1(b) represents the snapshot for the CPML, which clearly points out the improvement due to the absorbing layer. There emerge no considerable reflections from the boundaries. We want to remark, that the waves are damped inside the layer and therefore they are smoothed down to 0 at the outermost boundary. Suitable results only exist inside the computational domain before the waves enter the CPML. In Fig. 4.2 we plot (a) the horizontal and (b) the vertical component of
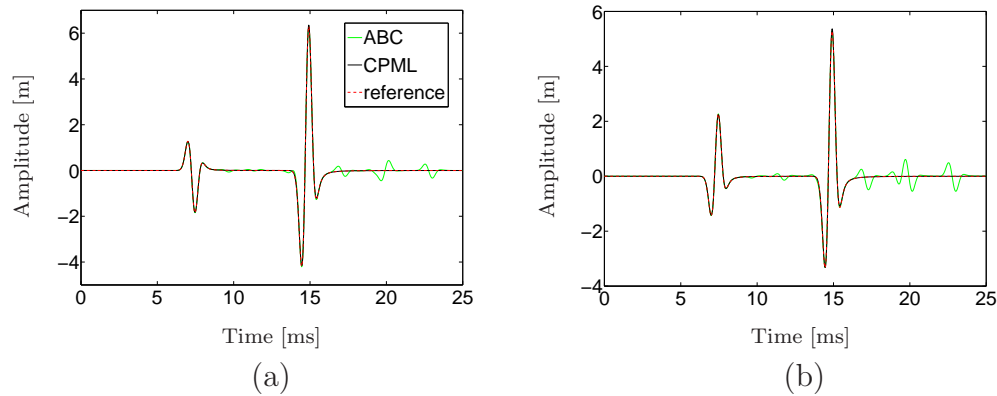
Figure 4.2: *Test case KoTro1: Horizontal (a) and vertical (b) components of displacement recorded by the receiver at* $(12, 33)$ m *for absorbing boundary conditions (green), convolutional perfectly matched layers (black) and a reference solution (dashed red). The reference solution is obtained by a computation on an enlarged domain, for which boundaries do not yet influence the signals.*

displacement recorded by the receiver at $(12, 33)$ m for 3 different simulations in order to obtain a quantitative comparison. As before, one simulation is performed using ABCs, one for the CPML and a third one run again with ABCs but on an enlarged domain of size 100×60 m^2. In this way, there arise no reflections of any boundary at the receiver within the total simulation time of $T = 25$ ms. Hence this simulation serves as a reference solution. Up to numerical deviation the signals obtained with the CPML lie exactly on top of the red reference signal. Regarding the artificial reflections of the results produced by using ABCs it is evident how effectively the CPML works. For a definite statement we look at the envelope misfit (EM). The horizontal component computed using only ABCs produces EM $= 1.05\%$ whereas for the CPML we obtain EM $= 1.05 * 10^{-1}\%$. The results look similar for the vertical component. Here, ABCs lead to EM $= 1.41\%$ whereas the CPML causes only EM $= 1.42 * 10^{-1}\%$. Thus, we can conclude that the results of our numerical simulation improved by one order of magnitude for applying the CPML. Computed on the local cluster COREDUMP, which is a HP ProLiant GL 580 G5 machine of 16 Intel Xeon X7350 QuadCore processors, the runtime takes 570 s using a CPML and 350 s for ABCs. It should me mentioned that in spite of a 60% longer simulation time we still benefit from the CPML. The alternative to avoid boundary reflections using common ABCs is the enlargement of the domain as used for the reference solution, which would increase the CPU time by a factor of 4.5.

Moreover, the code is running stable until the end of the simulation at $T = 0.025\,\text{s}$. We do not have to switch off the CPML. In order to critically look at stability constraints, we examine the wave propagation even up to $0.05\,\text{s}$, when all waves have traveled out of the domain. Again, there do not appear any instabilities or unwanted oscillations. The CPML is feasible without any constraints and the energy inside the domain is decaying constantly.

4.3.2 KoTro2

As we want to perform a more sophisticated test case, we validate the CPML method also for surface waves. Therefore, we take a computational domain of $\Omega = [-15, 15] \times [-30, 0]\,\text{m}^2$ and encounter one free surface as well as CPMLs at two of the remaining boundaries. Following Komatitsch and Tromp [72] the source is again a Ricker pulse with dominant frequency of $1000\,\text{Hz}$. It is placed very close to the surface at a depths of $y = -1.5\,\text{m}$ and a horizontal distance of $x = 3\,\text{m}$ from the center of the domain in order to generate a strong incident Rayleigh wave. The medium has a P-wave velocity of $c_p = 2000\,\text{m/s}$, a S-wave velocity of $c_s = 1154.7\,\text{m/s}$ and the density is $\rho = 2200\,\text{kgm}^{-3}$. A receiver is located on the surface at a horizontal distance of $x = 10.5\,\text{m}$ from the center and records the two components of displacement. A CPML of width $\Delta = 2.5\,\text{m}$, which counts again 10 elements for a mesh spacing of $\Delta h = 0.25\,\text{m}$, is applied to the two vertical edges of the medium. No CPML is used at the bottom of the domain, as the simulation stops at $T = 25\,\text{ms}$, before reflected waves can come back to the receiver. The polynomial degree is chosen to be 4. In order to examine the improvement of a CPML we recompute the same test case using only ABCs for artificial boundaries. For a reference solution we consider the same model setup but using only ABCs at the vertical boundaries and for a domain enlarged in positive x-direction. Its size is given by $\Omega = [-15, 35] \times [-30, 0]\,\text{m}^2$. The seismograms of displacement for the receiver at $(10.5, 0)\,\text{m}$ of all three simulations are presented in Fig. 4.3. Like Komatitsch and Tromp, we mostly observe a strong Rayleigh wave as the receiver is located at the surface and additionally the smaller direct body waves. In case of the simulation using ABCs, a large spurious signal is reflected at the vertical boundary, while for the acting CPML, this unwanted reflection is almost perfectly suppressed. The reference signal underlines this result, showing a failure-free seismogram. Furthermore, the computation including the CPML remains stable until the final simulation time.
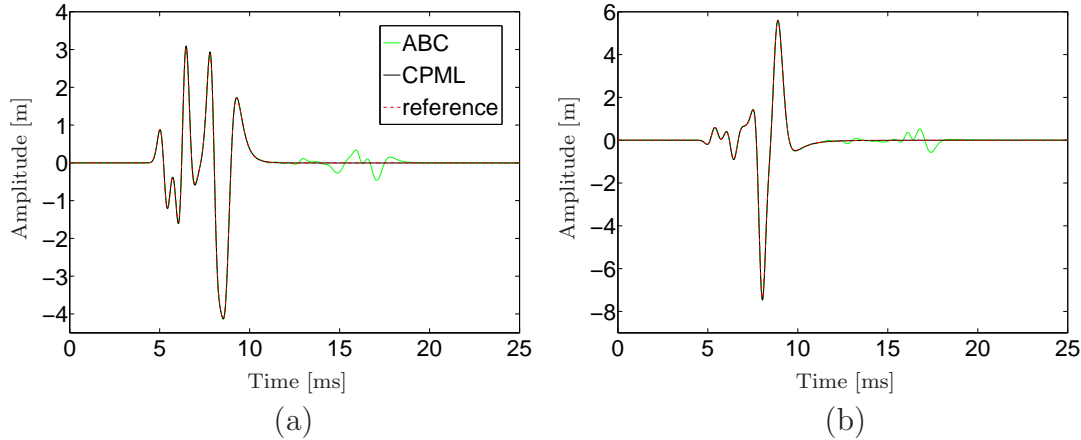
Figure 4.3: *Test case KoTro2: Horizontal (a) and vertical (b) components of displacement recorded by the receiver at $(10.5, 0)$ m for absorbing boundary conditions (green), convolutional perfectly matched layers (black) and a reference solution (dashed red). The reference solution is obtained by a computation on an enlarged domain, for which artificial boundaries do not yet influence the signals.*

4.3.3   KoMa

Our third test case is related to one example presented by Komatitsch and Martin [73] in 2007. They introduce the unsplit CPML to the equations of elastodynamics using the velocity-stress formulation Eq. (1.1) and apply it to the FD method in 3D. It can be shown (App. C) that their formulation of the scheme inside the CPML is included as a special case within our more general formulation. Besides the arbitrary constant term within our solution, the main discrepancy of the two approaches is, that Komatitsch and Martin assume the spatial partial derivative to be constant over one timestep, whereas our method provides high-order solutions due to the polynomial description.

The model setup of test case KoMa looks very similar to the one of test case KoTro (Sec. 4.3.1). The computational domain is given by $\Omega = [0, 1000] \times [0, 6400]$ m including a CPML of 200 m. With a mesh spacing of $\Delta h = 20$ m, the width of the CPML again counts 10 elements. The material properties are given by $\rho = 2800 \, \text{kgm}^{-3}$, $c_p = 3300 \, \text{ms}^{-1}$ and $c_s = 1905 \, \text{ms}^{-1}$. Therewith, the Poisson's ration is $\nu = 0.25$. The Ricker source has a dominant frequency of $f_0 = 7 \, \text{Hz}$ and is located at $(790, 4270)$ m. The polynomial degree 4 for the approximation of the solution remains unchanged and the total simulation time is set to $T = 4 \, \text{s}$. For a simulation without an energy-controlled switch off of the CPML, we detect a

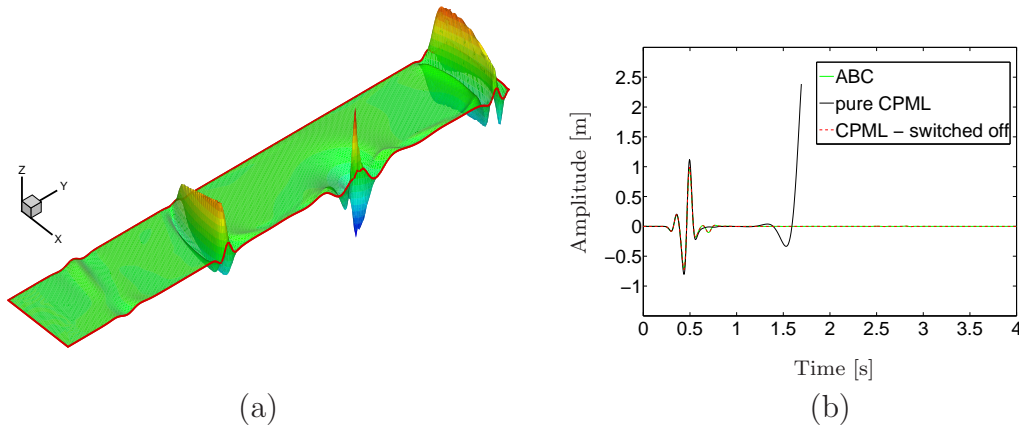(a)   (b)

Figure 4.4: *Test case KoMa: (a) Snapshot of velocity u after 1.2 s propagation time for a simulation performed by using the CPML. (b) Seismograms of vertical displacement recorded by the receiver at (210, 4130) m as a comparison between computations using either ABCs, a pure CPML or an energy-controlled CPML, which is switched off after 0.1 s.*

fast growing instability. It emerges inside the absorbing layer close to the source location, visible after about 0.8 s. Fig. 4.4 (a) illustrates the instability as a snapshot of velocity u after 1.2 s propagation time. The recorded signals of a nearby receiver at (210, 4130) m are plotted in Fig. 4.4 (b). Here, we only show the pure CPML results up to 1 s as the divergence is rapidly increasing. Already 0.2 s later, the receiver records values of a factor of 10 higher than the original amplitude of the signal. The fact, that this receiver registers the instability, proves that the instability is not only arising inside the CPML but also expanding into the inner computational domain.

For a comparison we perform exactly the same simulation but using common ABCs instead of the CPML. The signal is also plotted in Fig. 4.4 (b). As for this receiver location the waves arrive almost perpendicular at the boundary we discover only small reflections.

A third simulation is performed using the CPML, but with switching off the CPML according to the energy criterion (see Sec. 4.2). Already after 650 iterations, which corresponds to a simulation time of 0.1 s, the energy control forces us to terminate the CPML approach and thus, only ABCs are used for the rest of the computation. It is perspicuous, that we do not achieve any improvement by using the CPML, as it has to be switched off before the signal arrives at the boundary. Hence, we cannot gain any improved absorption result of the CPML. At least, the quality of our simulation is not suffering from this approach, which

means, that the results are not worse than results obtained by using mere ABCs. However, due to the initialization of the CPML and the reinitialization when the system returns to ABCs, the CPU time is increasing. For the test case KoMa the computation on 16 processors of the local cluster COREDUMP using ABCs lasts approximately one hour whereas the energy controlled CPML simulation requires one and a half hours, which makes a difference of 50%.

Although Komatitsch and Martin cannot exclude that their approach becomes unstable, they claim, that they do not observe any instability developing during the 3D simulation up to $160\,\mathrm{s}$. Using the classical second-order staggered grid in space and time they produce low-order results which tend to preserve stability longer than high-order results [79]. For a second-order ADER-DG scheme the stability holds up $1.75\,\mathrm{s}$ which is much longer than for the fifth-order (polynomial degree 4) simulation, but still not comparable to the test case of Komatitsch and Martin.

4.4   Discussion

We presented a convolutional perfectly matched layer for the ADER-DG method. In general, it achieves a satisfying absorption of seismic waves of arbitrary frequency at artificial boundaries of the computational domain. After the discretization of the scheme, the capacity decreases for grazing incidence of the waves, but it is still much more effective than common absorbing boundary conditions or prior PMLs. However, another shortcoming of the CPML is a potential instability arising already for small perturbations. According to different parameter studies, it is difficult if not impossible to predetermine where and when the system starts to diverge. Therefore, we control the computation by tracking the energy of the system which can act as an indicator for emerging instabilities.
The test cases examined in this study show considerably different results. The first one called KoTro1 performs very well without having to switch off the CPML. In this way the results improve by one order of magnitude implying an increase of CPU time of 60%. The second test case called KoTro2 confirms this high capability of the CPML also for surface waves. However, the third test case, KoMa, suffers from a growing instability already before the outgoing waves arrive at the outer boundary. Thus, the system has to return to a computation with common ABCs before it would be able to profit from the layer. This means an increase of computational cost while the results do not improve. Hence, we suggest the user

to perform a simplified test run and to decide if it is worth to activate a CPML before computing extensive parameter studies.

Chapter 5

Topography Effects on Seismic Waves

The problem of scattering of seismic waves caused by an irregular topography which affects the intensity of ground motions has been studied for many years. Bouchon [26], e.g., claims that surface displacement appears to be strongly influenced by surface irregularities. He performs an application to the Pacoima Dam site, California, and figures out that the high accelerations recorded during the San Fernando earthquake in 1971 could have been amplified between 30% and 50% by uneven topography. In the case of a ridge, a zone of amplification takes place near the top, whereas, for a depression, a zone of attenuation occurs near the bottom. Studying the region of the Appalachian Mountains, Griffiths and Bollinger [27] find out that, using mine blasts, the vertical data obtained display a lesser degree of amplification than do the horizontal data. Nowadays, simulations show that depending on the relative location of faulting and the nearby large-scale topography, the topography can shield some areas from ground shaking up to 50% [28]. However, also interaction between small-scale topographic features and high-frequency surface waves can produce unusual strong shaking. Focussing on the area of Shamao mountain, Taiwan, Lee et. al [29] demonstrate a relative change in ground motion of a factor of 2 between a valley and a ridge. For the Umbria-Marche earthquake in 1997 Pischiutta et. al [81] find two separate frequency bands in which amplifications take place. Their 2-D model underestimates the observed amplification. This detection is frequent in the literature [82, 83, 84, 85] and can be justified by considering the high complexity of reality compared to the simplified theoretical models, which often do not involve subsur-

face layering, neighboring topography and smaller scale geological irregularities in general.

We perform a systematic study on topographic effects using the ADER-DG method which is highly suitable for complex topography, as it can handle unstructured meshes. We analyze ground motion characteristics for different parameters like

- Frequency,

- Dataset Resolution,

- Strength of the Topographic Relief and

- Wave Type

in an alpine region around Grenoble in a first study.

As people from the seismological branch of the Munich Earth Observatory of the Ludwig-Maximilians-Universität (LMU) München measured amplification factors up to 5 between the stations in the valley and at the top of Mt. Hochstaufen, South Bavaria, we are interested in an application to this area and compare the results of our study to real measurements in a second step.

5.1   Grenoble

5.1.1   Model Setup

For a systematic study of topographic effects on seismic waves we chose the area of Grenoble, a city in south-eastern France situated at the foot of the French Alps at an altitude of 204 - 500 m. Fig. 5.1 shows a satellite picture of the Grenoble valley bounded by the Belledonne range in the east. Here, the mountains reach a height of 2977 m. Therewith, the incorporated topography includes summits, steep slopes as well as a few plateaus and the plain of the Grenoble valley. Our computational domain encompasses an area of 50 km×47 km. The depths of the 3 dimensional domain conforms to the input signal in each simulation and is given in Tab. 5.1. As we only consider teleseismic events, we use a vertical plane-wave incidence from below. In the simulation code this is accomplished by defining an initial condition of a Ricker-type wave. Hence, the depth of the domain depends

Figure 5.1: *Satellite picture of the region of Grenoble looking from south to north. The city itself lies in a valley at the foot of the French Alps. The high mountains on the right side of the picture form the Belledonne Massif.*

on the halfwidth of the input wave travelling upwards into positive z-direction. Having seen that pure absorbing boundary conditions are not absolutely satisfying, especially at grazing incidence (see Chap. 2), we apply periodic boundary conditions to the lateral faces of the domain (see Sec. 1.5). Since the opposite faces have to be conforming, we also need to ensure conforming edges lying vis-à-vis at the topography. Therefore, we set the height of the edges to the minimum altitude of the topography. In order to smooth the topography down to that minimum value $z_{\min}$ at the outer boundary we perform a damping profile to an outer layer having a width of 10% of the domain's extension in the particular dimension. With the real coordinates z_{real} and the modified coordinates z_{layer} inside the layer the damping profile applied to the topography reads

$$z_{\mathrm{layer}}(x,y) = z_{\min} + z_{\mathrm{real}}(x,y) * \frac{1}{2}\left[\sin\left(\frac{d(x,y)}{\Delta}\pi - \frac{\pi}{2}\right) + 1\right]. \qquad (5.1)$$

Here, Δ denotes the fixed distance between the outer boundary and the interface, where the damping layer meets the inner domain and d represents the distance
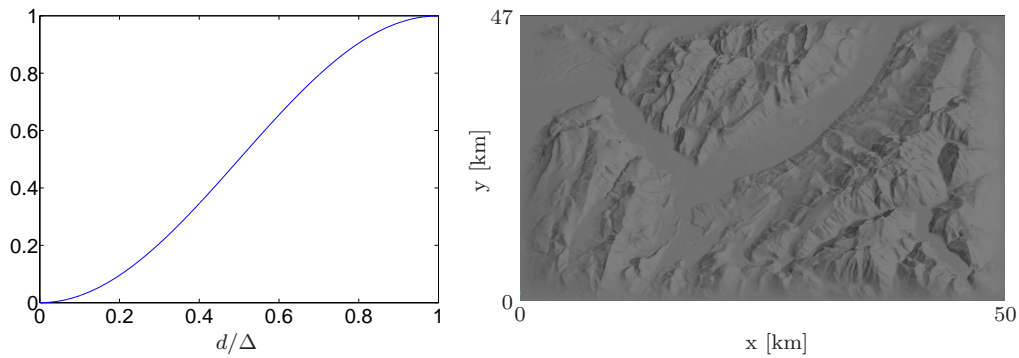
Figure 5.2: *(a) Damping profile for the smoothing layer surrounding the computational domain. (b) Surface topography, slightly tilted, as used in computations.*

to the outer boundary. The damping profile is visualized in Fig. 5.2 (a).   Fig. 5.2

f [Hz]	z_{source} [km]	z_{bottom} [km]	$\Delta h_{\max}$ [m]	T [s]
2	-2.5	-5	500	5
1	-3.5	-7	800	5
0.5	-7	-14	1600	10
0.25	-14	-26	1600	16

Table 5.1: *Chosen parameters for a systematic study depending on the frequency of the input signal.*

(b) shows the surface for the modified topography in a slightly tilted 3D view (azimuth $= 0^{\circ}$, vertical elevation $= 48^{\circ}$), looking from south to north with a light source from the east.

As we want to focus on purely topographic effects, we assume homogeneous material properties throughout the domain. The density is given by $\rho = 2700 \, \text{kg/m}^3$, the shear modulus is $\mu = 6.912 \cdot 10^9 \, \text{Pa}$ and the bulk modulus is $\lambda = 1.3824 \cdot 10^{10} \, \text{Pa}$. Thus, we obtain wave velocities of $c_p = 3200 \, \text{m/s}$ and $c_s = 1600 \, \text{m/s}$.

Like the depths of the model, several parameters, listed in Tab. 5.1, depend on the frequency f of the input signal. The depth z_{source} of the source refers to the center of the Ricker-type plane wave propagating in z-direction and z_{bottom} means the depth of the computational domain. The maximum mesh spacing $\Delta h_{\max}$ is roughly estimated as half the wavelengths. For simulations using an
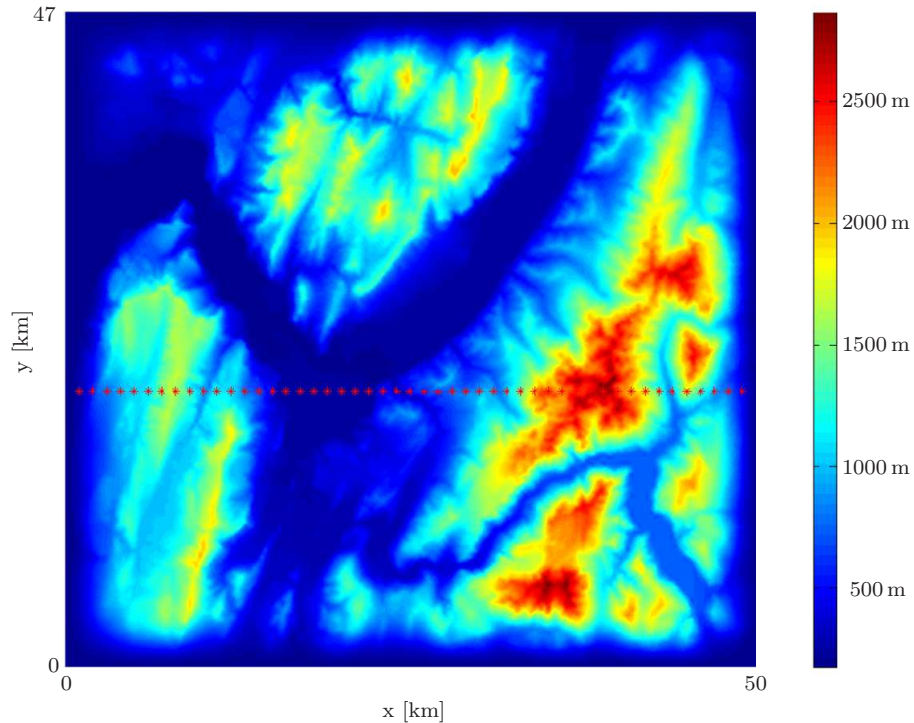
Figure 5.3: *49 receivers, indicated by red stars, are located at the surface of the domain. The color code refers to the surface elevation.*

ADER-DG $\mathcal{O}4$ scheme and propagation distances of only a few wavelengths this should lead to reasonable results as we have seen in Chap. 2. Only for the lowest frequency we leave the mesh spacing equal to 1600 m which is still fine enough with respect to the extension of the domain. Therewith, we arrive at about 2 to 3 million elements per mesh. The total simulation time T, the period until the crucial part of the signal arrives at the receivers at the surface, depends on the depth of the source and thus on the frequency. The simulations last about 5 to 15 hours performed on 510 processors of the SGI Altix 4700 (HLRB II) at Leibniz-Rechenzentrum, just to give a rough indication for the CPU time.

As visualized in Fig. 5.3 we include a receiver line of 49 geophones along $y = 20\,\mathrm{km}$ at the surface, where the distance of 2 receivers is given by $\Delta x = 1\,\mathrm{km}$. In this way we can track particle motion across the valley as well as for the highest elevation of the domain. In addition, we create a regular grid of 401×401 data points at the surface, leading to a spacing of 120 m in x- and 113.75 m in y-direction. For each of these grid points, we measure the peak ground velocity (PGV) and acceleration (PGA) during the simulations.
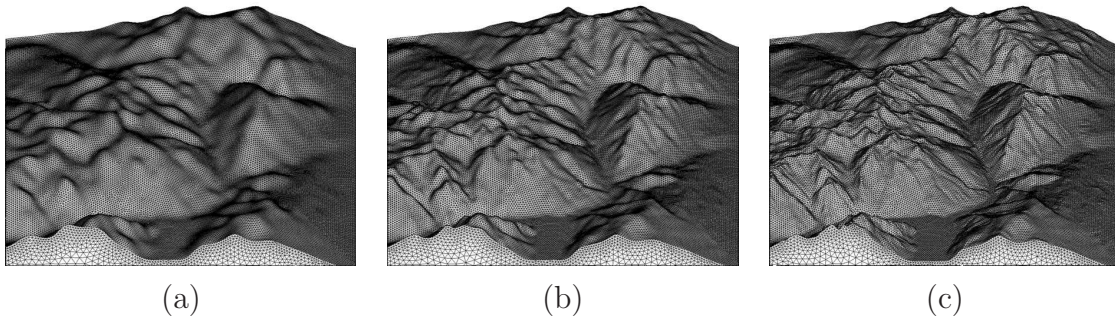
(a)   (b)   (c)

Figure 5.4: *Different dataset resolutions for an extraction at the Belledonne Massif. We consider (a) 500 m (b) 250 m and (c) 100 m sampling to create the geometry, while the triangular surface-mesh spacing of 100 m is kept constant.*

Firstly, we study different frequencies of the input signal over a range of one order of magnitude from 0.25 Hz up to 2 Hz.

Secondly, we are interested in the effect of dataset resolution. Therefore, we take digital elevation models of different resolution and build the surface geometry with bicubic spline interpolation. With refining the datasets, using a spatial sampling of $\Delta s = 500$, 250 and 100 m, the details of topographic features increase, as shown in Fig. 5.4. However, the mesh spacing $\Delta h = 100$ m of the computational mesh and therefore the numerical resolution at the topographic surface is kept constant in order to avoid changes due to numerical discretization differences. This means that the mesh spacing for the whole volume of the domain starts with $\Delta h = 100$ m at the surface and grows with increasing depth until the respective maximum mesh spacing $\Delta h_{\max}$, depending on the frequency, is attained.

As a third step, we consider the influence of the strength of the topographic relief itself. To this end, we amplify or deamplify the topography by scaling factors of $A_{\text{topo}} = 0.5$, 1, 1.5 and 2. Fig. 5.5 shows the computational domains for the 4 different scaling factors, where the amplification factor $A_{\text{topo}} = 1$ corresponds to the real topography. Deamplifying the topography by $A_{\text{topo}} = 0$, we obtain a flat box which serves as a reference model without topography.

As a fourth parameter, we examine different wave types: for the vertical propagation direction (z-axis) we distinguish between compressional waves polarized in z-direction (P-waves), and shear waves polarized in either x- or y-direction (SX- or SY-waves, respectively).
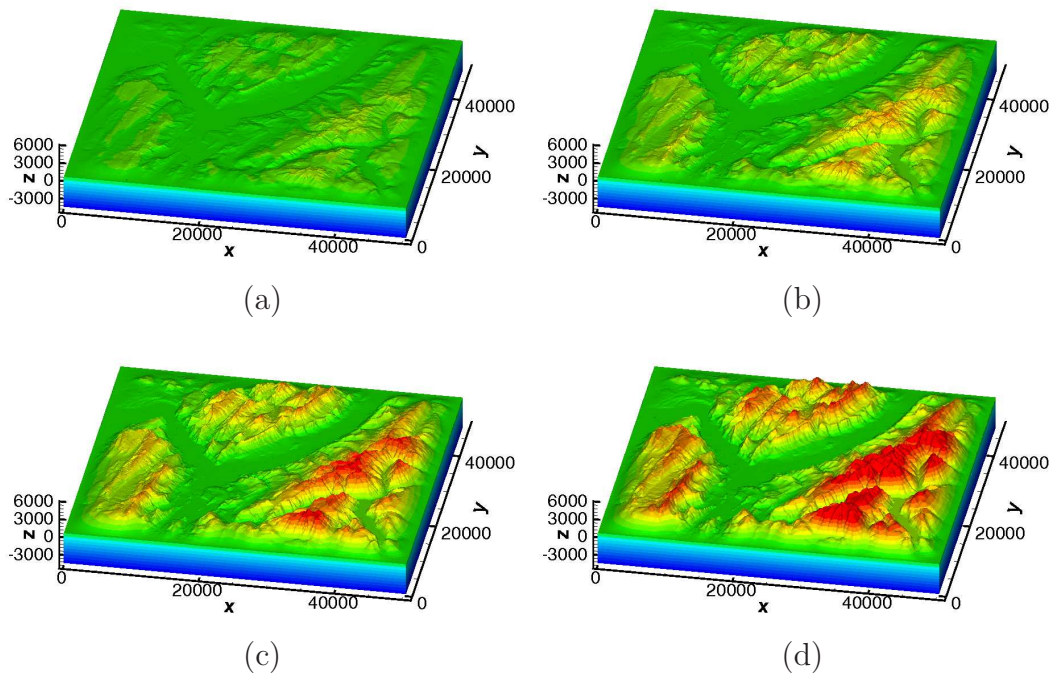
Figure 5.5: *Computational domain for the 4 different topographies. The real topography (b) is multiplied by (a) 0.5, (c) 1.5 and (d) 2. The color code denotes the elevation.*

5.1.2 Results

Comprising several combinations of different parameterizations as specified above, more than 100 simulations are performed. Here, we want to focus on some selected results.

First, we investigate PGV maps for several parameter studies. To account for a clear and understandable presentation of the results, we start with some reference simulations for which we use flat boxes as computational domains. Therewith, the amplification factor applied to the topography is denoted by $A_{\text{topo}} = 0$ and the reference PGV maps are given by PGV_{flat}. Independent of the input signal frequency, the wave type, the dataset resolution and the location at the surface we obtain the - up to numerical accuracy - same value for the peak ground velocities for all reference simulations and all grid points given by $\text{PGV}_{\text{flat}} = 2.0\,\text{m/s}$. From now on, we normalize all PGV maps by this reference value, which means that we divide the PGVs by $\text{PGV}_{\text{flat}} = 2.0\,\text{m/s}$. Hence, we obtain a dimensionless quantity having a value greater than 1 whenever we observe

Frequency [Hz]	PGV_{min}	PGV_{max}	PGA_{min}	PGA_{max}
0.25	0.73	1.52	0.77	1.85
0.5	0.62	1.59	0.68	1.93
1.0	0.58	1.71	0.64	1.84
2.0	0.53	1.64	0.63	1.88

Table 5.2: *Maximum and minimum values of peak ground velocity (PGV) and peak ground acceleration (PGA) in dependence of the frequency computed for a planar P-wave traveling through a domain with real topography ($A_{topo} = 1$) and 250 m dataset resolution. All values are normalized by the reference solution given by PGV_{flat} or PGA_{flat}, respectively.*

an amplification of the PGV and a value smaller than 1 for a deamplification. In the following we continue to denote this quantity by PGV. The same convention is used for PGA, where PGA_{flat} depends on the frequency of the input signal.

Frequency

Our initial test case considers various frequencies of the Ricker-shaped input signal. To this end, we keep the type of the input signal, a vertical plane P-wave, and the dataset resolution of 250 m constant. The surface of the computational domain represents the real topography, i.e., the amplification factor $A_{topo} = 1$. The PGVs for $f = 0.25\,Hz, 0.5\,Hz, 1\,Hz$ and $2\,Hz$ are illustrated in Fig. 5.6. The color code refers to PGV, normalized to 1, as explained above. Warm colors indicate a higher PGV and cold colors a lower PGV than the reference value. One general statement is, that we observe amplifications of PGV at mountain tops or ridges. As expected, for flat areas or plateaus we usually see PGVs similar to the reference value. Regarding steep slopes or quite narrow valleys the PGVs are lower than the reference value. The four plots in Fig. 5.6 clearly show, that the PGV pattern becomes more and more spatially refined with increasing frequency. This observation is quite comprehensible as higher frequencies better resolve geometrical structures. Another effect of increasing frequency is the tendency of increasing deviation of extremal PGV values from the mean value which can be extracted from Tab. 5.2. Here, the spatial minima and maxima of the PGVs and PGAs with respect to the entire surface are given for different frequencies. Therewith, we can conclude, that the effect of topography gets more and more decisive for increasing frequency in general. However, the continuous frequency-dependent decrease of the minima of PGVs and PGAs is clearer than the increase of their maxima.
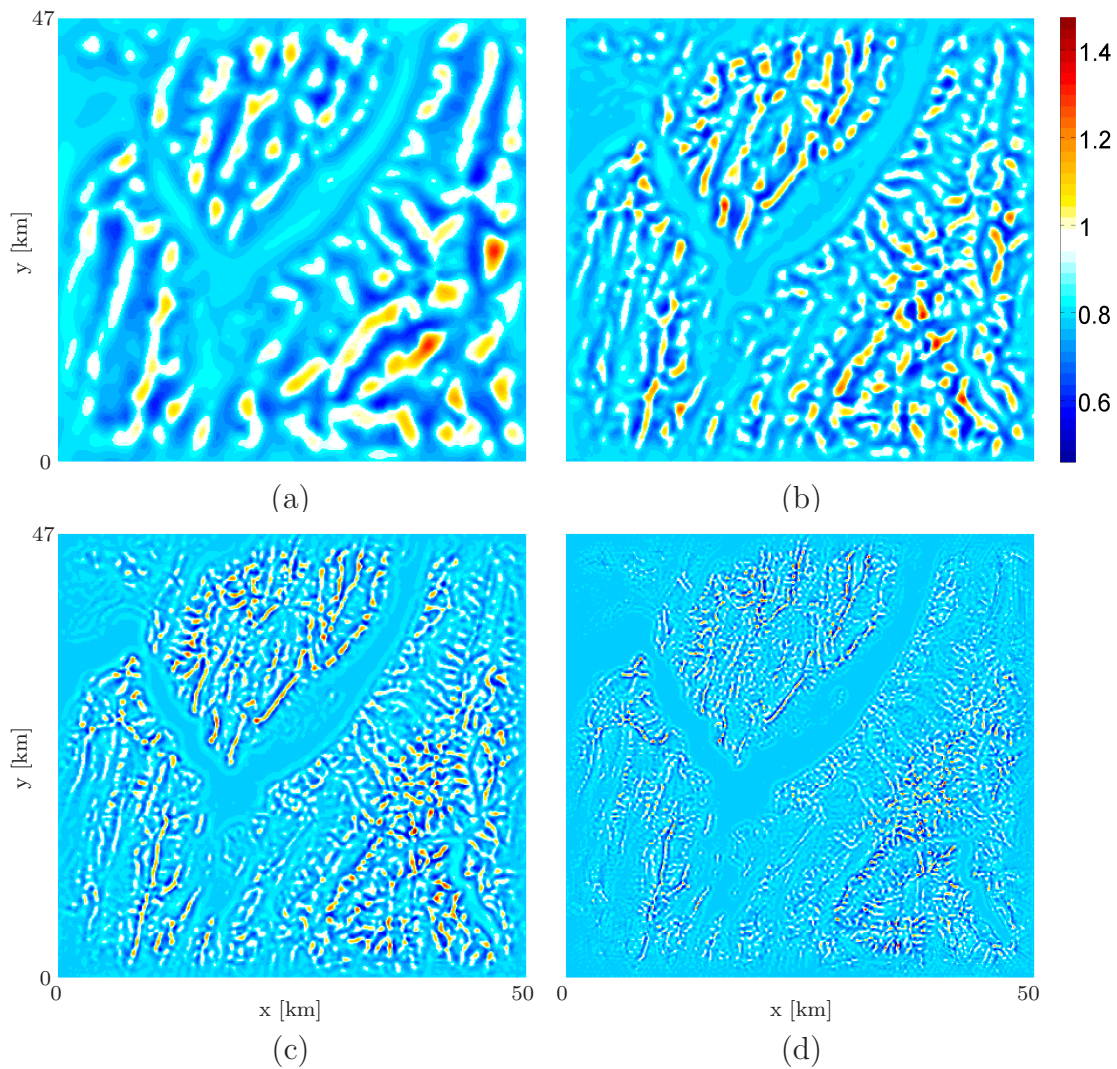
Figure 5.6: *Peak ground velocity (PGV) map as result of a vertical plane P-wave of (a) 0.25 Hz, (b) 0.5 Hz, (c) 1 Hz and (d) 2 Hz applied to the real topography with a dataset resolution of 250 m.*

Fig. 5.7 visualizes the maximal values of PGVs in dependence of the frequency for different dataset resolutions. The highest PGV value is reached for a 2 Hz signal using the finest sampling rate. A closer look to the relevance of dataset resolution is given in the next paragraph.

Dataset Resolution

The following discussion refers to different underlying dataset resolutions. Fig. 5.8
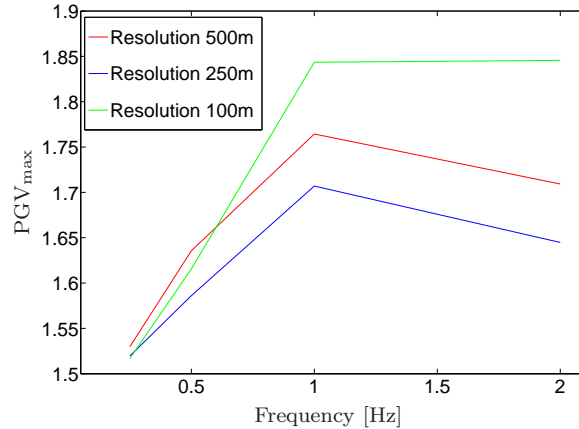
Figure 5.7: *PGV$_\mathrm{max}$ in dependence of the dominant frequency of the incoming P-wave for different dataset resolutions applied to the real topography ($A_{topo} = 1$).*

Resolution [m]	PGV$_\mathrm{min}$	PGV$_\mathrm{max}$	PGA$_\mathrm{min}$	PGA$_\mathrm{max}$
500	0.72	1.71	0.80	1.90
250	0.53	1.64	0.63	1.88
100	0.48	1.85	0.62	2.02

Table 5.3: *Maximum and minimum values of PGV and PGA in dependence of the dataset resolution applied to the real topography computed for a planar P-wave of $2\,$Hz.*

shows the two PGV maps for simulations on domains with a $\Delta s = 100\,$m resolved surface and a $\Delta s = 500\,$m resolved surface. Once again, we want to point out, that the mesh spacing of $\Delta h = 100\,$m at the surface remains unchanged. As the mesh spacing of half of the shortest occurring wavelength is accepted to be sufficient to reach a numerical error below 10% (see Chap. 2), the discretization of the topography does not affect the results, as the surface discretization is about 4 times finer than required for sufficient numerical accuracy. We use the real topography and an input signal of $f = 2\,$Hz, as the effect of different dataset resolutions is more matured for higher frequencies. For $\Delta s = 100\,$m we see not only a much more detailed PGV map than for $\Delta s = 500\,$m, but also increased amplification and deamplification values as can be extracted from Tab. 5.3. Moreover, the extremal values of PGV are only rarely reached in case of the coarse dataset resolution as topographic features are mostly smoothed out. By contrast, the PGV maps for different dataset resolutions of simulations with
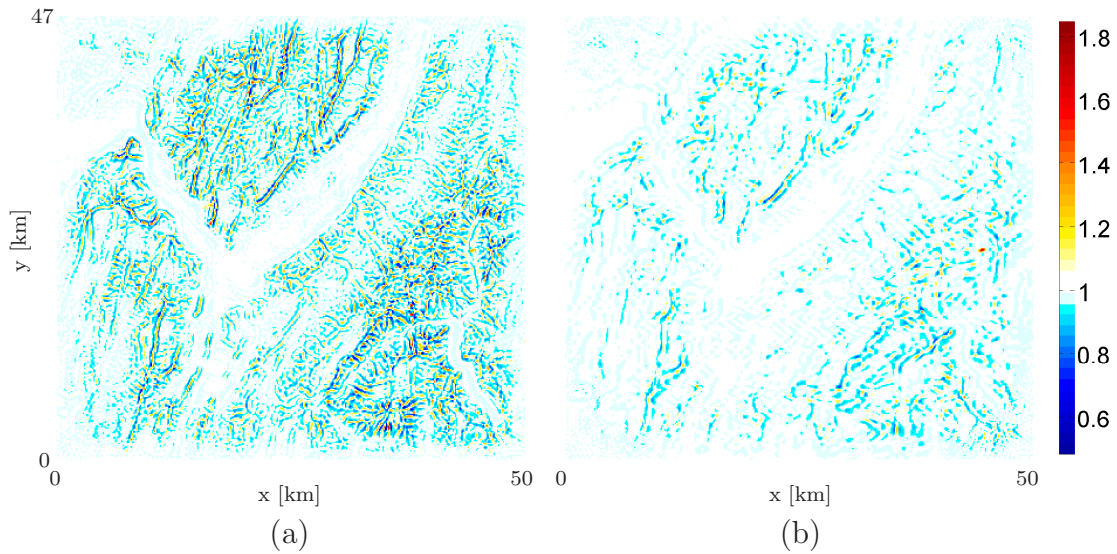
Figure 5.8: *PGV map for simulations using differently resolved surfaces of the real topography. The geometry is discretized by (a) $\Delta s = 100$ m and (b) $\Delta s = 500$ m, whereas the mesh spacing $\Delta h = 100$ m remains equal. As input signal we chose a plane P-wave of frequency 2 Hz.*
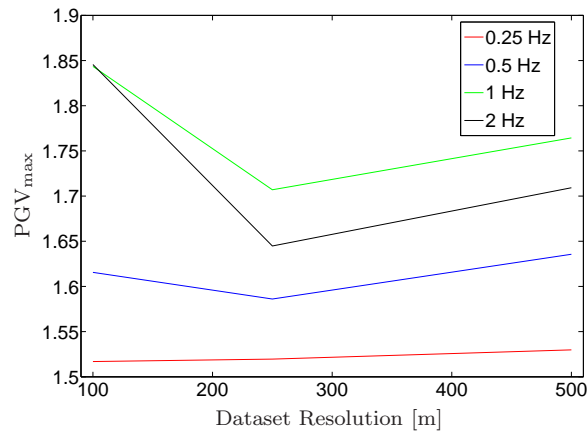
Figure 5.9: *$PGV_{\max}$ in dependence of data set resolution for different frequencies of the incoming P-wave applied to the real topography ($A_{topo} = 1$).*

an input signal of $f = 0.25$ Hz and $f = 0.5$ Hz show almost no difference, as confirmed by the small changes of the $PGV_{\max}$ value in Fig. 5.9. For the frequency $f = 1$ Hz a difference in PGV maps is identifiable, but the PGV map obtained for the dataset resolution of 100 m does not expose more details compared to the

PGV map for the resolution of 500 m. Hence, we conclude that the determining criterion for the required dataset resolution is the highest considered frequency and accordingly the shortest considered wavelength. Obviously, Fig. 5.9 shows, that the used dataset resolution for the 0.25 Hz simulation (corresponding to the shortest wavelength of 6400 m) lies below such an upper limit, as the data line is nearly constant. Regarding the 0.5 Hz simulation (i.e., 3200 m shortest
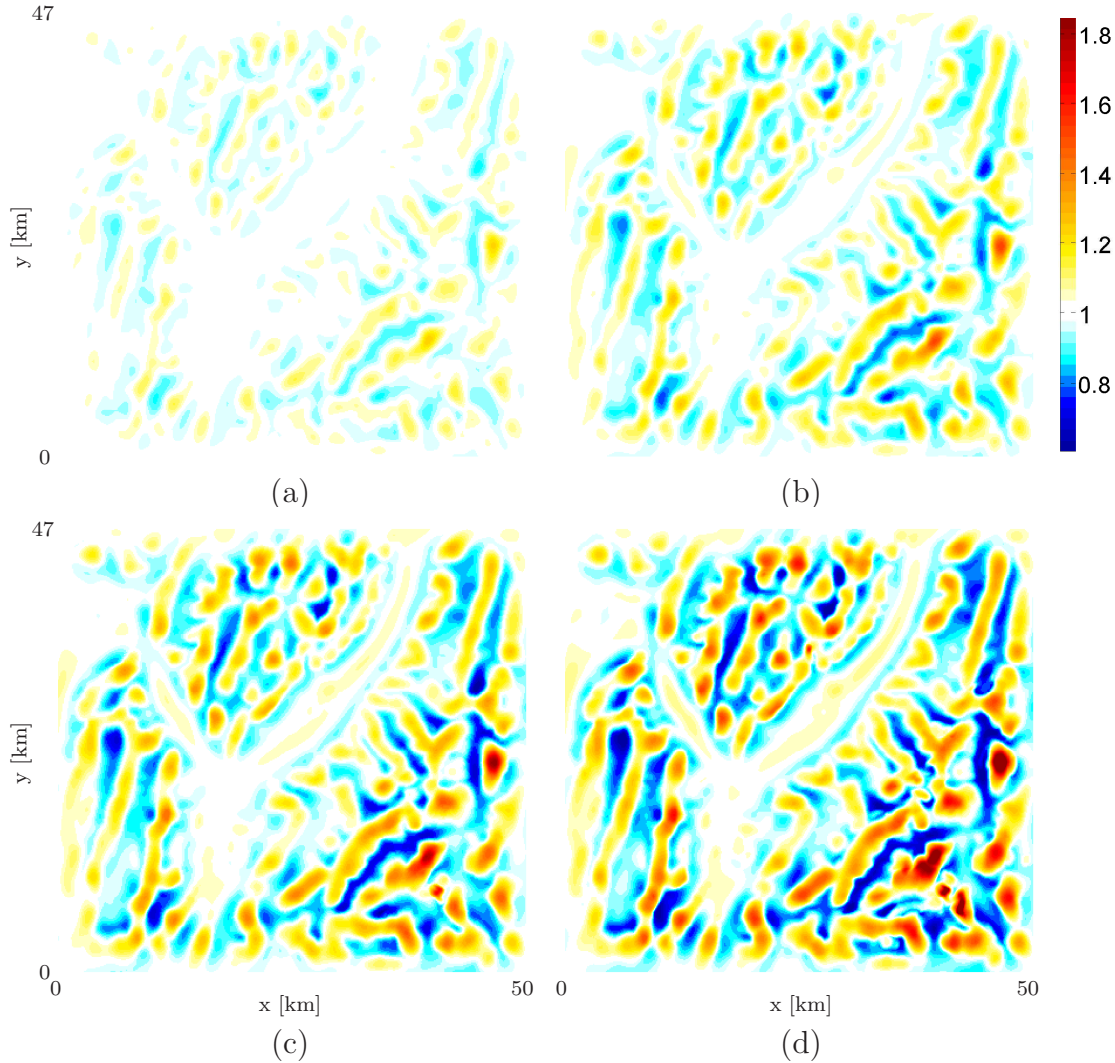

Figure 5.10: *PGV map showing the effects of the topographic relief. The applied amplification factors to real topography are given by (a) $A_{\text{topo}} = 0.5$, (b) $A_{\text{topo}} = 1.0$, (c) $A_{\text{topo}} = 1.5$ and (d) $A_{\text{topo}} = 2.0$. For all simulations we used a plane P-wave of 0.25 Hz as input signal and the dataset resolution of $\Delta s = 500$ m.*

A_{topo}	PGV_{min}	PGV_{max}	PGA_{min}	PGA_{max}
0.5	0.86	1.25	0.88	1.40
1.0	0.73	1.53	0.77	1.84
1.5	0.61	1.84	0.67	2.29
2.0	0.57	2.28	0.62	3.27

(a)

A_{topo}	PGV_{min}	PGV_{max}	PGA_{min}	PGA_{max}
0.5	0.81	1.34	0.86	1.34
1.0	0.62	1.76	0.71	1.86
1.5	0.51	1.92	0.65	2.27
2.0	0.45	2.45	0.57	2.66

(b)

Table 5.4: *Maximum and minimum values of PGV and PGA in dependence of the amplification factor applied to the topography computed for a planar P-wave of (a) $0.25\,\text{Hz}$ and (b) $1\,\text{Hz}$ with dataset resolution $\Delta s = 500\,\text{m}$.*

wavelength), we observe a lower gradient between $100\,\text{m}$ and $250\,\text{m}$ dataset resolution than between $250\,\text{m}$ and $500\,\text{m}$ dataset resolution. Thus, we assume the limit somewhere in between the second interval. For both the $1\,\text{Hz}$ ($1600\,\text{m}$ shortest wavelength) and the $2\,\text{Hz}$ ($800\,\text{m}$ shortest wavelength) simulation the gradient is stronger within the first interval. As the black line in the plot illustrates a considerable change between the first two data points, we suggest to use a spatial sampling of $100\,\text{m}$ at most for the shortest wavelength of $800\,\text{m}$. Summarizing those observations, we can give a rough estimation for the required dataset resolution for simulations which include topography: we suggest to use the eighth part of the shortest considered wavelength at most.

Strength of the Topographic Relief
Looking at PGVs we additionally want to comprise varying amplification factors of the topography. Therefore we consider simulations where the real surface is amplified by $A_{\text{topo}} = 0.5, 1.0, 1.5$ and 2. First, we show results obtained by using a plane P-wave of $f = 0.25\,\text{Hz}$ as an input signal and use the resolution
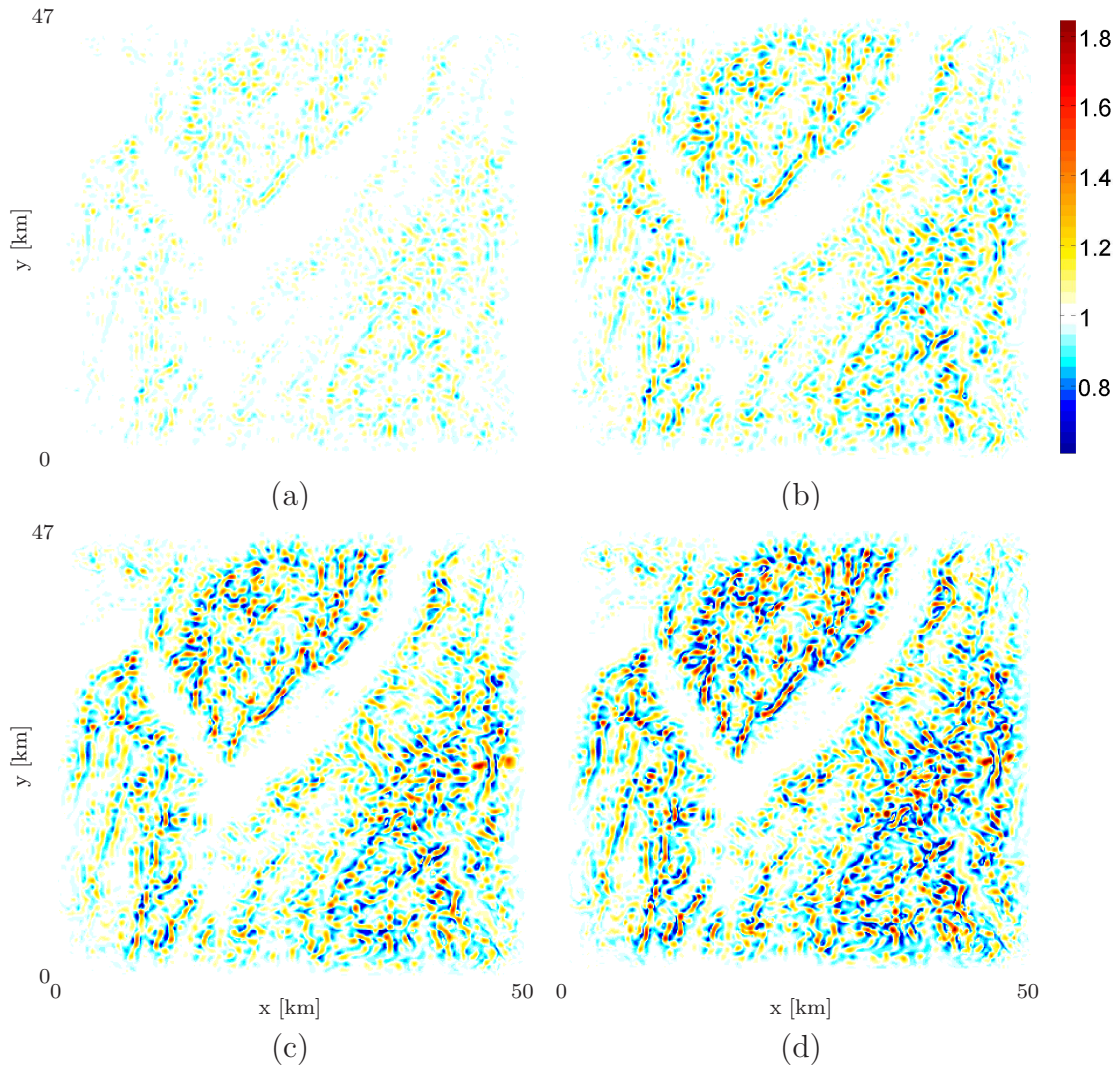
Figure 5.11: *PGV map showing the effects of distinct topography. The applied amplification factors to real topography are given by (a) $A_{\text{topo}} = 0.25$, (b) $A_{\text{topo}} = 1.0$, (c) $A_{\text{topo}} = 1.5$ and (d) $A_{\text{topo}} = 2.0$. For all simulations we used a plane P-wave of $1\,\text{Hz}$ as input signal and the dataset resolution of $\Delta s = 500\,\text{m}$.*

$\Delta s = 500\,\text{m}$. The PGV maps are given in Fig. 5.10. Again, the color code denotes the ratio of the measured PGVs and the reference PGV. It is evident, that the PGVs are drastically affected by the topography. With increasing the amplification factors of the topography, also the deviations of PGVs and PGAs from the reference value grow. Tab. 5.4 (a) presents the extremal values of the PGV and PGA maps in order to verify this statement.
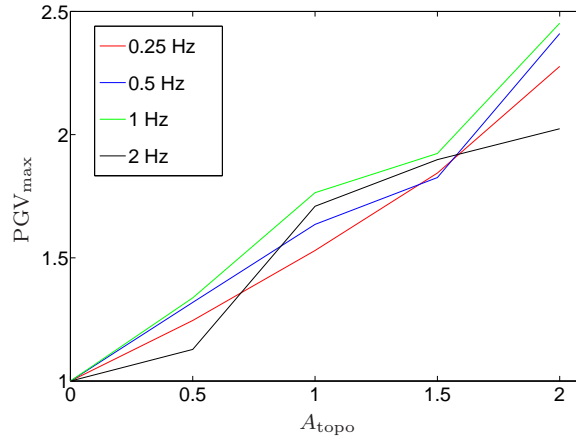
Figure 5.12: *PGV_{max} in dependence of the strength of the topographic relief for different frequencies of an incoming P-wave computed for a dataset resolution of $\Delta s = 500\,\mathrm{m}$.*

Fig. 5.11 displays the PGVs of simulations for $f = 1\,\mathrm{Hz}$, whereas the remaining parameterizations are kept unchanged. The results demonstrate the same tendency of PGVs and PGAs, which become more pronounced for increasing amplification factors applied to topography. According to the frequency study above, the PGV pattern for the $f = 1\,\mathrm{Hz}$ simulations are much more detailed compared to the simulations using a $f = 0.25\,\mathrm{Hz}$ input signal (Fig. 5.10). The extremal values of PGVs and PGAs for the 1 Hz simulation are given in Tab. 5.4 (b). It also attracts attention, that the extremal PGVs of the $f = 1\,\mathrm{Hz}$ simulations are always further away from the mean value than those of the $f = 0.25\,\mathrm{Hz}$ simulations, which confirms our results from the frequency study above. The maximum PGVs for all considered frequencies are displayed in Fig. 5.12. All lines steadily increase with increasing the amplification factors of topography. Thus, we conclude that PGVs are heavily influenced by the strength of the topographic relief, whereas the single extremal values predominantly depend on the complicated interference of the wavefield, which is heavily scattered by the topography.

Wave Type

Finally, Fig. 5.13 (a), (c) and (e) illustrate the disparity between SX-, SY- and P-waves for simulations including the real topography with a dataset resolution of 500 m. The input signals with a frequency of 2 Hz are planar body waves propagating from the bottom to the free surface and polarized in either x-, y- or

Wave Type	PGV_{min}	PGV_{max}	PGA_{min}	PGA_{max}
P-wave	0.53	1.64	0.63	1.88
SX-wave	0.35	2.36	0.41	2.61
SY-wave	0.36	2.48	0.36	2.62

(a)

Wave Type	PGV_{min}	PGV_{max}	PGA_{min}	PGA_{max}
P-wave	0.72	1.71	0.80	1.90
SX-wave	0.37	2.10	0.41	2.01
SY-wave	0.38	2.03	0.40	2.05

(b)

Table 5.5: *Maximum and minimum values of PGV and PGA in dependence of the wave type applied to real topography computed for* 2 Hz *signals with dataset resolution of (a)* $\Delta s = 250$ m *and (b)* $\Delta s = 500$ m.

z-direction.

Comparing the PGVs of the compressional wave (e) with the two shear waves, it is obvious, that topography has a higher impact on shear waves. For S-waves, not only most of the points have a PGV which deviates from the reference value 1, but also the different scalings of the colorbars point out, that the amplifications and deamplifications for PGVs are much more pronounced than for P-waves. Tab. 5.5 highlights this observation for the considered parameterization and additionally for an equal model setup but using a dataset resolution of $\Delta s = 250$ m.

In general, regarding different frequencies of S-waves, we recognize the same behavior as for P-waves: Minima and maxima of PGVs become more and more distinct for increasing frequency. However, as already mentioned, the topographic influence on shear waves is higher than on P-waves. Moreover, Fig. 5.14 visualizes the maxima of PGVs depending on frequency for different wave types. In this test case, we discover, that for each wave type, the highest PGV values are reached for 1 Hz simulations. Therefore, we assume that the prominent topographic features of the studied region could be on a scale where wavelengths of about 1600 m are influenced most.

Concerning PGAs of S-waves we obtain results comparable to those of P-waves. With increasing frequency, the minimum of PGAs is steadily decreasing, whereas
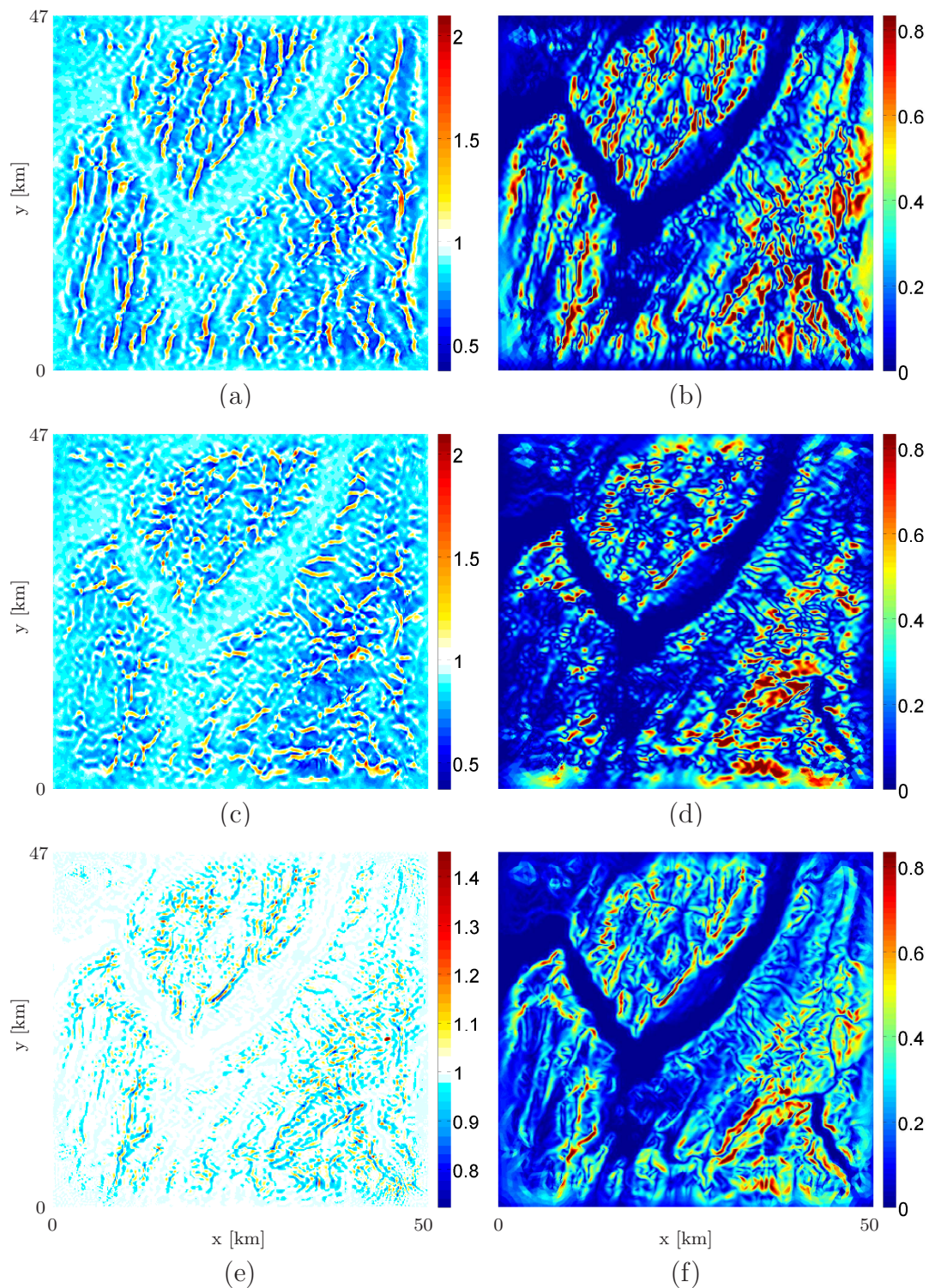
Figure 5.13: *PGV map for a simulation of (a) a plane SX-wave, (c) a plane SY-wave and (e) a plane P-wave of 2 Hz frequency applied to the real topography with a dataset resolution of 500 m. The colorbars refer to relative PGV. (b) and (d) illustrate the* **slope** *of the topography, depending on the x- and y-direction, respectively. Here, the colorbars denote absolute slope. The mean values between slopes in x- and y-direction are given in (f).*
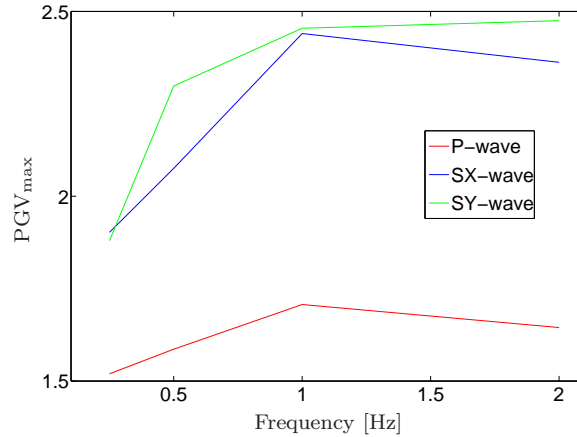
Figure 5.14: $PGV_{\max}$ in dependence of the frequency of different incoming wave types applied to the real topography ($A_{topo} = 1$) with a dataset resolution of $\Delta s = 250\,\mathrm{m}$.

only the tendency of an increasing maximum is identifiable. Like for PGVs, the upper and lower limits of PGAs for S-waves are more pronounced than for P-waves.

A closer look to the SX- and SY-wave (Fig. 5.13 (a) and (c), respectively) shows that the maximum PGVs prevail at ridges elongated in y- and x-direction, respectively. This detection seems quite intuitive, as the ridges which induce high PGVs are oriented perpendicular to the polarization of the waves, which in turn means that the essential topographic characteristics, like changes between steep slopes, strong curvatures and crests, coincide with the polarization of the waves. The statement also holds for minimum PGVs: the slopes below ridges of appropriate direction usually show strongest deamplification, which is similar to the observations of Bouchon [26].

   Having seen that PGVs are strongly influenced by changes in topography, we pay particular attention to the spatial derivative of the topography in the following. In order to obtain single-valued quantities we first separately look at the gradient of topography in either x- or y-direction shown in Fig. 5.13 (b) and (d). Here the colorbars denote the absolute value of slope. Comparing PGVs with the accordant derived topography, we observe very similar structures in general as well as some patches of excellent agreement. For example at the upper right corner of Fig. 5.13 (a), north of the Belledonne Massif, we obtain high PGVs at a north-south elongated ridge. For the eastern hillside PGVs are clearly deamplified whereas for the western hillside we see PGVs varying around the mean

value. The same feature arises for the gradient in Fig. 5.13 (b). The ridge itself represents a local maximum in space and therewith a minimum with respect to slope. The eastern hillside indicates much steeper topography than the western one.

Another manifest example is the steep slope at the right bottom of Fig. 5.13 (d). Also the PGV map in Fig. 5.13 (c) emphasizes this region by exposing a deamplification of ground velocities.

If we now try to find these two examples within the other set of plots in each case, we discover, that both regions are much less conspicuous for the other direction. This fact emphasizes again the strong dependence of topographic effects on polarization.

Fig. 5.13 (f) shows the average of slopes in x- and y-direction. Therewith we obtain a quantity for the absolute steepness independent of direction. This in turn is quite useful to analyze the PGVs of an incoming P-wave. Most of the features highlighted by the gradient can also be identified for the PGV map (Fig. 5.13 (e)). For example the distinct ridge north of Grenoble or the steep hills confining the Belledonne Massif in the south are in clear agreement. Besides, the PGVs also agree with regions of low topographic changes, like the valley of Grenoble, the valley of Le Bourg d'Oisons, south-east of the Belledonne range, or the plateau in the north of the just mentioned steep hills. Summarizing, we can say that all these characteristics bring out the relation between PGVs and topography again: widely flat areas, basins or plateaus do not influence the PGVs significantly, whereas the steeper the surface is, the more deamplification results for PGVs. At mountain ridges or summits, where the slope changes most, we obtain maximum PGV.

As this last feature concerns the derivative of slope, not the slope itself, we additionally look at the curvature of the topography. It is illustrated in Fig. 5.15 in the right column of plots. Fig. 5.15 (b) and (d) refer to curvature in x- and y-direction, respectively, and Fig. 5.15 (f) reflects the mean value of curvature. The left column, like in Fig. 5.13, corresponds to recorded PGVs. Compared to the slope, the curvature offers an even more detailed pattern, where the dependency on direction is characteristic. However, taking a closer look to the details, the plots for slope mostly reveal a better fit to PGVs than the plots for curvature.

So far, we analyzed the PGV and PGA, which are single-valued quantities, for each of the grid points at the surface. To see the complete signal in time for a particular location, we now investigate in detail particle motions along the
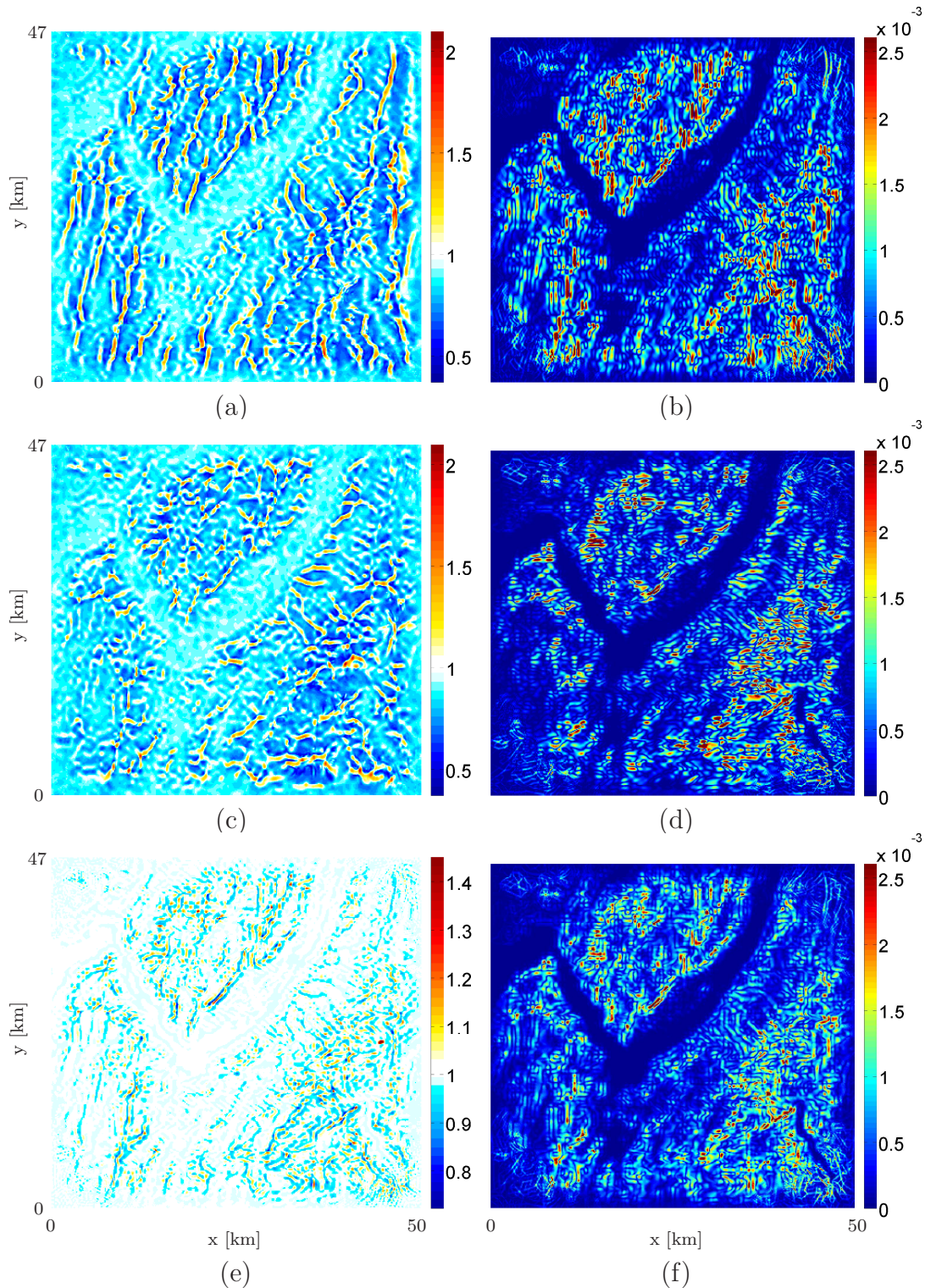
Figure 5.15: *PGV map for a simulation of (a) a plane SX-wave, (c) a plane SY-wave and (e) a plane P-wave of 2 Hz frequency applied to the real topography with a dataset resolution of 500 m. The colorbars refer to relative PGV. (b) and (d) illustrate the* **curvature** *of the topography, depending on the x- and y-direction, respectively. Here, the colorbars denote absolute curvature. The mean values between curvatures in x- and y-direction are given in (f).*

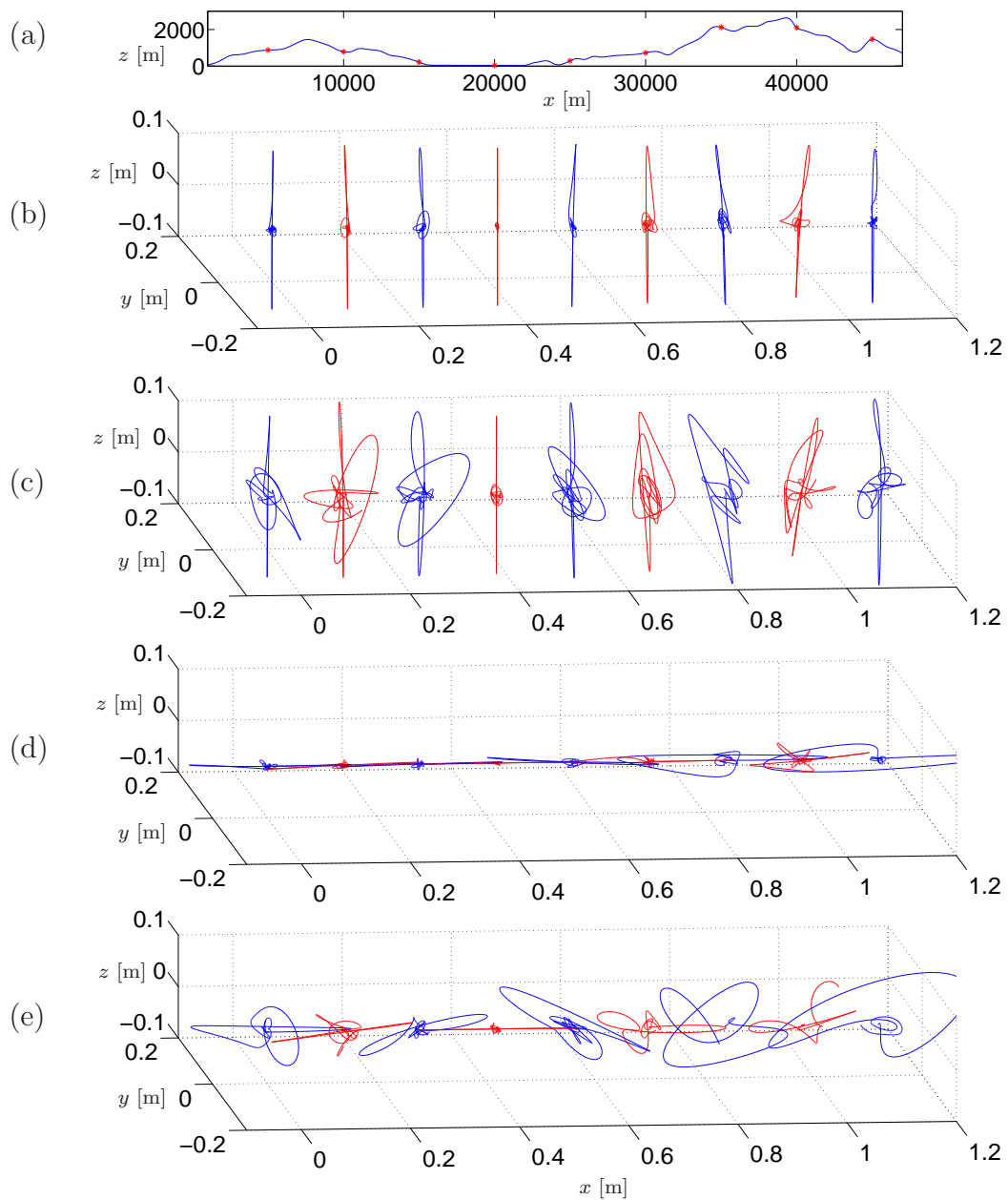**Figure 5.16:** *(a) Profile of the 2D section where receivers (red stars) are located. (b) Trajectories of particle motion along the 2D section for an incoming P-wave of 2 Hz frequency and $A_{\text{topo}} = 0.5$. (c) Trajectories of particle motion along the 2D section for an incoming P-wave of 2 Hz frequency and $A_{\text{topo}} = 2$. (d) and (e) show according results to (b) and (c) for an incoming SX-wave.*

receiver line defined in the previous section in Fig. 5.3. Fig. 5.16 (a) shows the real profile of the 2D section with some receivers on the surface. Those receivers, for which we present the particle motion, are indicated by red stars. Fig. 5.16 (b) and (c) illustrate the particle motions obtained for a P-wave arriving at the topography which is amplified by $A_{topo} = 0.5$ and $A_{topo} = 2$, respectively. By contrast, the particle motions for a SX-wave are displayed in Fig. 5.16 (d) and (e), again for $A_{topo} = 0.5$ and $A_{topo} = 2$, respectively. Usually, the oscillation of a particle at the surface follows the polarization of the incoming wave. For P-waves as well as for SX-waves this fact is mostly evident for the deamplified topography. However, already for these two plots (Fig. 5.16 (b) and (d)) we observe perturbations from this predominant direction. Comparing the trajectories of particles to their locations, we see that flat areas clearly reflect the impulse of the polarization direction. At steep locations or summits we remark a much more complex motion including the other directions. The particle motions generated by the amplified topography (Fig. 5.16 (c) and (e)) are even more affected. Especially for the SX-wave some particle motions are quasi decoupled from the original polarization of the wave with the exception of the single receiver located in the midst of the valley at $x = 20000\,\mathrm{m}$.

5.1.3   Discussion

We performed a systematic study of topography effects on seismic wave propagation. The investigated parameters included frequency, dataset resolution, strength of the topographic relief and wave type.

Peak ground motion reaches highest values at ridges or mountain tops in general. It is obvious, that the PGV pattern mainly follows the gradient of topography, not the topography itself or the curvature. The highest amplification factor of PGV for a theoretical simulation applied to real topography is 2.48. It is reached for a SY-wave of $2\,\mathrm{Hz}$. The most impressive example of topographic effects for a simulation with real topography is a ratio of 6.89 between maximum and minimum PGV for a SY-wave of $2\,\mathrm{Hz}$ with a dataset resolution of $250\,\mathrm{m}$.

Regarding different frequencies we can conclude, that higher frequency results in an exceedingly detailed PGV map. The maximum value of PGV tends to grow and the minimum PGV clearly decreases with increasing frequency.

The PGV maps of the $2\,\mathrm{Hz}$ simulations become more and more differentiated with refining the dataset resolution. Moreover, the deviation from the mean value of these PGVs drastically increases for higher resolution. We suggest to

take a dataset resolution of the eighth part of the shortest considered wavelength
at most.

By analyzing different amplifications (resp. deamplifications) of the real topogra-
phy, we find out, that steeper topography increases maximum PGV and decreases
minimum PGV significantly. This result elucidates the high impact of topogra-
phy on seismic waves.

In our study topography better affects shear waves more than compressional
waves. SX-waves are primarily influenced by topographic structures elongated in
y-direction and vice versa.

From the complete time signals of the receivers at the surface it is manifest that
single components behave very differently as particle motion becomes much more
complex due to wave interference.

5.2   Hochstaufen

After the systematic study of topographic effects on seismic waves, we now want
to compare our numerical results with real measurements. The key question here
is, if the amplitude amplifications in observations can be explained by the to-
pography effect alone, or if other mechanisms have to be considered. Therefore
we choose the region of Mt. Hochstaufen, located in Southern Bavaria, Germany,
where the Munich Earth Observatory of the LMU München maintains several
seismic stations.

Beforehand, we perform a frequency study in order to get an overview of topo-
graphic effects on seismic waves on the scale of the selected region. Additionally,
we simulate surface waves and discuss the obtained results in matters of topog-
raphy.

5.2.1   Model Setup

The involved region of Mt. Hochstaufen has an elevation between $448\,\mathrm{m}$ and
$1771\,\mathrm{m}$. We translate the topography by $z = -448\,\mathrm{m}$. Therewith, the height of
the model surface reaches values from 0 to $1323\,\mathrm{m}$. A surface map of the region
of Mt. Hochstaufen where the stations are included is given in Fig. 5.17 (a). We
take a digital elevation model of $25\,\mathrm{m}$ sampling rate from the Land Processes
Distributed Active Archive Center (LP DAAC) and create a tapered surface as
described in Sec. 5.1.1 in order to obtain a model which is appropriate for periodic
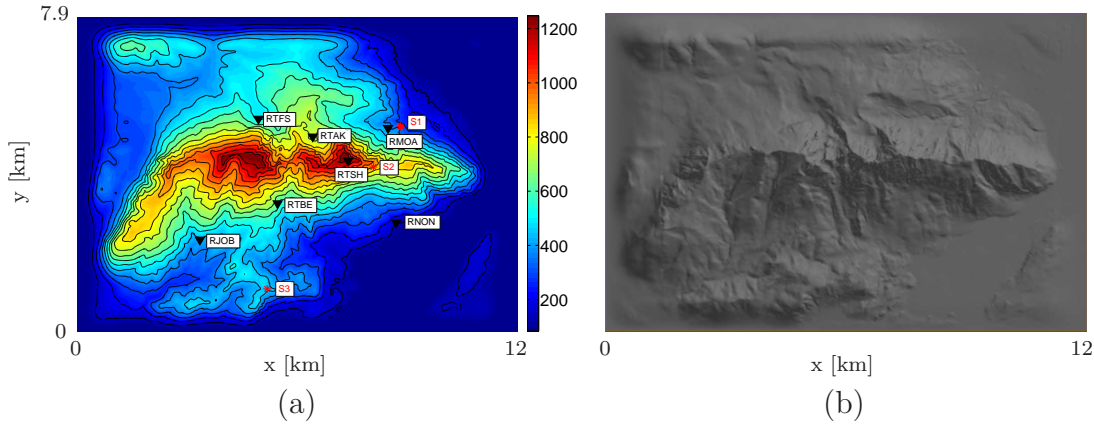
Figure 5.17: *(a) Contour plot of Mt. Hochstaufen including the seismic stations and the epicenters of three considered events. The color code refers to modeled elevation. (b) Surface topography as used in the computations.*

f [Hz]	z_{source} [m]	z_{bottom} [m]	Δh_{max} [m]	# elements
20	-300	-600	80	$1.5 \cdot 10^6$
10	-550	-1100	160	$6.6 \cdot 10^5$
5	-1100	-2200	320	$5.6 \cdot 10^5$
2	-2750	-5500	800	$5.4 \cdot 10^5$
1	-5500	-11000	1600	$5.4 \cdot 10^5$

Table 5.6: *Chosen parameters for the simulations at Mt. Hochstaufen depending on the frequency of the input signal.*

boundary conditions. The free-surface topography of lateral extension $[0, 12] \times [0, 7.9] \, \text{km}^2$, pictured in Fig. 5.17 (b), is discretized by a mesh spacing of 50 m and the depth of a 3 dimensional domain again depends on the frequency of the input signal to accommodate the desired wavelengths. The studied frequencies as well as the applied parameters are given in Tab. 5.6. Analyzing surface waves, which travel in south-north direction, we enlarge the surface of the domain to $\Omega = [0, 12] \times [-2, 7.9] \, \text{km}^2$ in order to have enough space for generating surface waves before they enter the actual domain.

As there exists no detailed geological model of the region we assume homogeneous material throughout the domain. The density is given by $\rho = 2800 \, \text{kg/m}^3$, the shear modulus is $\mu = 2.867 \cdot 10^{10} \, \text{Pa}$ and the bulk modulus is $\lambda = 3.6848 \cdot 10^{10} \, Pa$, which yield wave velocities of $c_p = 5800 \, \text{m/s}$ and $c_s = 3200 \, \text{m/s}$. These are typical

material parameters for limestone, which dominates the region. The locations of 7 real seismic stations, as indicated in Fig. 5.17, are included in the computations to record the seismic signals. Additionally, we generate PGV maps. Again, the simulations for an ADER-DG $\mathcal{O}4$ scheme are performed on 510 processors of the SGI Altix 4700 (HLRB II) at Leibniz-Rechenzentrum and take about 10 h runtime for synthetic data of 12 s record length. The computations of surface wave propagation on the enlarged domains last approximately 10% longer.

5.2.2 Results

Like in the previous section we examine different input wave and source types of various frequencies.

Body Waves

Firstly, we consider body waves, i.e., P-waves, SX- and SY-waves travelling in vertical direction. The dominant frequencies of the Ricker-shaped plane waves are given in Tab. 5.6. Fig. 5.18 shows the PGV maps of the simulations for SX- and SY-waves. As explained in Sec. 5.1.2 the color code refers to the PGV maps normalized by the reference value of 2.0 m/s. In general, we can confirm the characteristics of topographic effects: The amplification of waves reaches its maximum at mountain tops and ridges, whereas the strongest deamplification is observed at the lower parts of steep hills. In predominantly flat areas, the PGV values resemble the reference value. Like for the test case of Grenoble we see a more and more detailed PGV pattern with increasing frequency.

Comparing SX- with SY-waves we recognize again that ground motion is influenced most when topographic features are oriented perpendicular to the polarization of the waves. This statement can be exemplified in the area of the main ridge of Mt. Hochstaufen elongated in west-east direction. Especially with increasing frequency we identify higher PGVs for SY-waves than for SX-waves. This observation also holds for the steep slopes north and south of this ridge, where the deamplification of PGV is more distinct for SY-waves. By contrast, in the west of the mountain, where a kink leads the ridge in south-west direction, the effects emerge also for SX-waves. The clear stripe of deamplification followed by a line of high amplification at the left upper boundary of the PGV maps in Fig. 5.18 is best visible in subfigures (h) and (k). It is an effect of the taper function applied to the topography at the outer boundaries of the domain. In
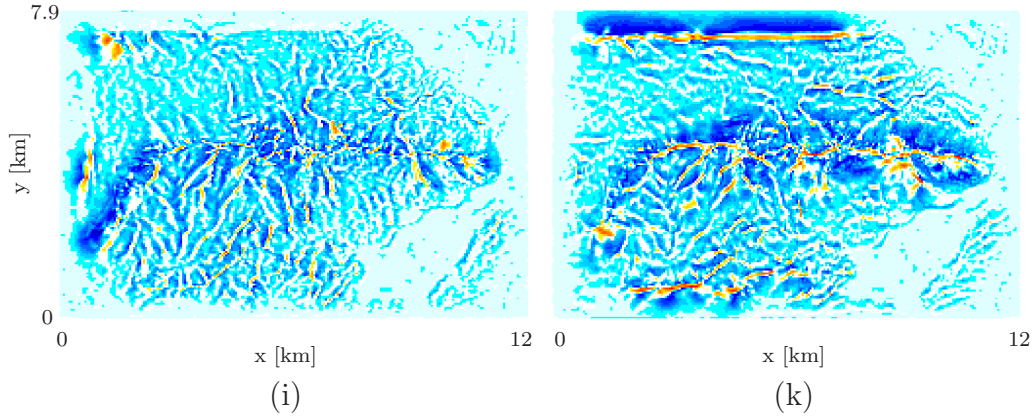
(a)

(b)

(c)

(d)

(e)

(f)

(g)

(h)
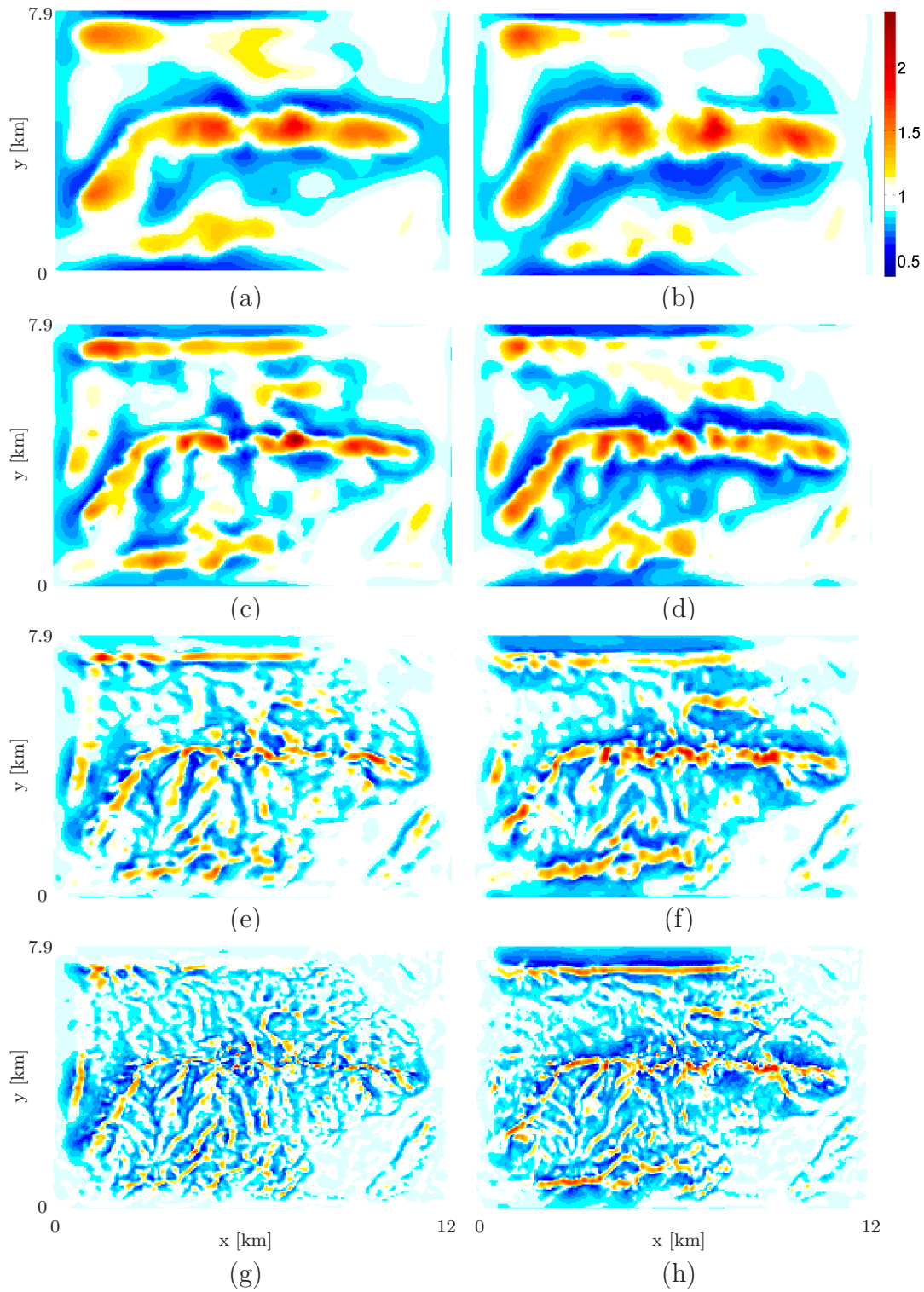
Figure 5.18: *Peak ground velocity (PGV) map obtained by simulating plane SX-waves of (a) 1 Hz, (c) 2 Hz, (e) 5 Hz, (g) 10 Hz, (i) 20 Hz and plane SY-waves of (b) 1 Hz, (d) 2 Hz, (f) 5 Hz, (h) 10 Hz and (k) 20 Hz. The color code refers to relative PGV.*

this area Mt. Teisenberg, which is oriented in east-west direction, is emerging and the topography has to be tapered continuously towards the outer boundary. PGVs of P-waves are less pronounced than PGVs of S-waves, as can be extracted from Tab. 5.7. Polarized in vertical direction, P-waves are influenced by topography independently of any particular alignment.

f [Hz]	P-wave		SX-wave		SY-wave	
	PGV_{min}	PGV_{max}	PGV_{min}	PGV_{max}	PGV_{min}	PGV_{max}
1	0.76	1.45	0.58	2.01	0.62	2.09
2	0.59	1.71	0.52	2.56	0.50	1.95
5	0.64	1.63	0.45	2.16	0.47	2.36
10	0.64	1.74	0.43	2.26	0.44	2.27
20	0.67	1.81	0.37	1.87	0.42	2.43

Table 5.7: *Maximum and minimum values of peak ground velocity (PGV) in dependence of the frequency computed for planar P-, SX- and SY-waves.*

Surface Waves

In our next study, we focus on surface waves. In order to create Rayleigh waves, we enlarge the domain by 2 km in the south. There, we put 119 point sources equidistantly from each other along a line at the surface. The source locations
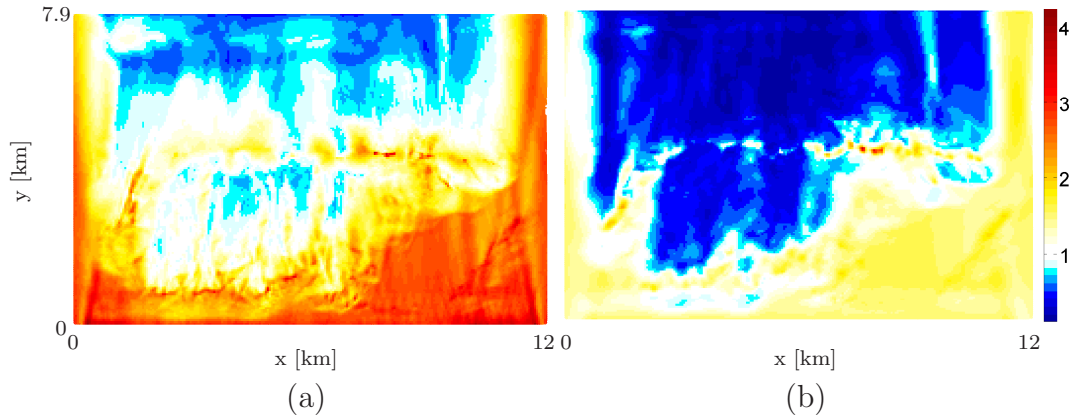
Figure 5.19: *Peak ground velocity map for simulations of surface waves of (a) 1 Hz and (b) 5 Hz travelling in south-north direction.*

f Hz	PGV_{min}	PGV_{max}
1	0.44	4.23
5	0.10	3.61

Table 5.8: *PGV_{min} and PGV_{max} for simulations of surface waves travelling from south to north.*

are given by $(100k, -1000, -0.1)$ m, with $k = \{1, 2, \ldots, 119\}$. The source time functions are Ricker-shaped impulses of either 1 Hz or 5 Hz acting on the vertical velocity component to create a vertical line force on the surface. This generates a strong plane Rayleigh wave travelling from south to north. Concerning the domain, the periodic boundaries remain in the east and the west, whereas in the south and the north we now apply absorbing boundaries which should work perfectly for the waves of normal incidence.

Fig. 5.19 shows the PGV maps for the simulations of (a) 1 Hz and (b) 5 Hz Rayleigh waves. For each simulation the PGVs are normalized to 1. This means that we perform reference simulations using the same setup but a flat surface. We obtain constant PGVs all over the surface ($PGV_{flat} = 1.8$ m/s for a 1 Hz and $PGV_{flat} = 6.7$ m/s for a 5 Hz simulation). Therewith, the PGVs of simulations including the real topography are divided by PGV_{flat} and can be compared to each other.

It is obvious that topography has an enormous impact an surface waves. On the one hand it shields the area behind (seen in propagation direction)

Event	Date	Time	Location [m]	Magnitude
1	September, 20th, 2007	16:51:43	(8801, 5176, -448)	1.5
2	September, 20th, 2007	20:04:51	(8063, 4167, 552)	3.4
3	April, 17th, 2008	16:00:31	(5170, 1133, -2448)	3.4

Table 5.9: *Location with respect to our model.*

Mt. Hochstaufen from ground shaking in both cases. On the other hand, there arises an amplification of PGV in front of the massif. This implies that waves are reflected from the mountain and interfering with each other. This can even be observed at the eastern and western boundary of the domain. We want to remark that we are using periodic boundaries there. Hence, the reflections from Mt. Hochstaufen seem to overlap in this area. Comparing Fig. 5.19 (a) with (b) we conclude, that the reflections are stronger for lower frequencies whereas the shielding seems to be more efficient for higher frequencies.

The extremal values of PGVs are presented in Tab. 5.8. It points out, that regions behind a topographic shield can attain a deamplification of 90%, whereas the area in front of such a shield may be amplified by a factor greater than 4 due to reflections.

Local Events

Finally, we look at some local events, for which real data are available. We choose three events that happened in the years 2007 and 2008. They are described in Tab. 5.9, where the coordinates of the hypocenters refer to the coordinate system of our model. Fig. 5.17 (a) illustrates the epicenters of the events and 7 stations located in the section of our computational domain which recorded the signals. The measured data run through a 0.5 Hz high-pass filter and the amplitude is corrected with respect to the instrument response spectrum.

For simulating these events we first use explosive point sources of 0.5 Hz, 2 Hz and 5 Hz dominant frequency for a general study. Explosive sources have a spherically symmetric radiation pattern and hence describe a fair alternative for simulations where the source mechanism and orientation is unknown. Moreover, the amplitude of the signals can be corrected with respect to the distance between source and receiver due to geometrical spreading. Afterwards we simulate double-couple point sources in order to examine how decisive the source orientation is.

In order to make the results of our numerical simulations comparable to real data, we examine amplification factors of PGVs between each available station

and the defined reference station RNON. The results for all 3 events are given in Tab. 5.10.

Regarding the real data (PGV_{real}) of event 1 (Tab. 5.10 (a)), we observe the highest amplification of PGV for the station RTSH, followed by RTAK and RTBE, whereas a clear deamplification occurs for stations RJOB and RTFS. This is quite perspicuous as RTSH is the station which is located closest to the top of Mt. Hochstaufen. RTFS and RJOB both are further away from the hypocenter than RNON and therefore, the low PGV values could partly be a consequence of geometrical spreading. Corrected according to the inverse square law, we obtain a factor of 0.41 for RJOB and 0.45 for RTFS. Additionally, both stations are located at the bottom of steep hills which also entails low PGVs. The same distance correction for stations RTBE and RTAK reflects amplification factors of 1.86 and 1.90, respectively. On the one hand, the adjacency of these two values is evident as both stations have similar surroundings. On the other hand, we would expect a much lower PGV value, as RTBE and RTAK are placed shortly below the middle of the slopes. Thus, we conclude, that the consideration of topography alone can not fully explain the observations.

The PGVs of simulating event 1 using an explosive source of $0.5\,\mathrm{Hz}$ ($PGV_{expl}^{0.5}$) tend to agree with real data. Again RTSH shows the highest amplification and the descending order of amplification factors is similar. However, it seems as if the simulation always underestimates the effect of topography on seismic waves. For the stations RTSH, RTAK and RTBE, where we observe an amplification in real data, the synthetic data indicate lower PGVs and for the stations RTFS and RJOB the synthetic data reveal higher PGVs than real data. Moreover, except for station RTBE, the synthetic data are always closer to the mean value. These characteristics agree with previous studies of Bouchon, Pischiutta and others [82, 83, 84, 85, 81] and implies that the complexity of reality, i.e., potentially inhomogeneous material and other site-effects, has a notable impact on seismic waves and therefore the effects on seismic waves cannot be described by topography considerations alone. The amplification factors for higher frequencies of explosive sources (PGV_{expl}^{2} and PGV_{expl}^{5}) do not deviate considerably from the results of the $0.5\,\mathrm{Hz}$ simulation. The greatest difference appears for the station RTSH, where the amplification factors clearly decrease with increasing frequency. This observation can be explained as higher frequencies see topographic structures in more detail. The station RTSH is located below the top of Mt. Hochstaufen. Therefore, it shows high PGVs for waves of low frequency for which - on a coarse scale - the station is placed close to the summit. By contrast, waves of higher

Station	RJOB	RTBE	RTSH	RTAK	RTFS
$\mathrm{PGV_{real}}$	0.16	1.14	5.11	1.74	0.28
$\mathrm{PGV^{0.5}_{expl}}$	0.29	0.41	1.67	1.17	0.52
$\mathrm{PGV^{2}_{expl}}$	0.27	0.34	1.63	0.99	0.48
$\mathrm{PGV^{5}_{expl}}$	0.33	0.36	1.19	0.79	0.43
$\mathrm{PGV^{4}_{double}}$	0.82	0.76	2.33	0.67	0.56

(a)

Station	RJOB	RTBE	RTSH	RMOA	RTAK	RTFS
$\mathrm{PGV_{real}}$	0.12	0.34	2.91	0.70	0.22	0.11
$\mathrm{PGV^{0.5}_{expl}}$	0.15	0.33	2.68	1.67	0.83	0.29
$\mathrm{PGV^{2}_{expl}}$	0.15	0.29	2.54	1.78	0.80	0.26
$\mathrm{PGV^{5}_{expl}}$	0.21	0.36	2.33	1.90	0.65	0.30
$\mathrm{PGV^{4}_{double}}$	0.60	0.93	3.90	1.88	1.77	1.35

(b)

Station	RJOB	RMOA
$\mathrm{PGV_{real}}$	0.92	0.51
$\mathrm{PGV^{0.5}_{expl}}$	1.39	1.31
$\mathrm{PGV^{2}_{expl}}$	1.49	1.34
$\mathrm{PGV^{5}_{expl}}$	1.59	1.27
$\mathrm{PGV^{4}_{double}}$	1.22	0.98

(c)

Table 5.10: *PGV amplification factors, normalized to the reference station RNON, for (a) event 1, (b) event 2 and (c) event 3. We regard real data and synthetic data for explosive sources of 0.5 Hz, 2 Hz and 5 Hz dominant frequency as well as a simulation for an arbitrarily oriented double-couple point source, where the maximum frequency is given by 4 Hz.*

frequency sample the surface more localized.

Analyzing event 2 (Tab. 5.10 (b)), we only see an amplification of PGV for the station RTSH in real data. All other stations demonstrate a deamplification of PGV. From a pure topographic point of view this result confirms the previous studies well, as RTSH is located at the ridge and the remaining stations are distributed over the slopes. Comparing event 1 with event 2 we observe similar factors for the stations RJOB, RTFS and still for RTSH. However, an enormous contrast arises for the stations RTAK and RTBE. Therefore, we assume that also the unknown source mechanism has a considerable effect on peak ground velocity. It should be mentioned that, for event 2, the PGVs of the stations RTAK and RTBE fit better to what we expect by regarding only topography.
The synthetic data for explosive sources, $PGV_{expl}^{0.5}$, PGV_{expl}^{2} and PGV_{expl}^{5}, agree with real data surprisingly well to a large extent. Only station RTAK and RMOA present up to a factor of 4 higher PGVs than real data. As also RTFS overvalues the PGV of real data, it attracts attention that these three stations are located north of the ridge. Therefore, a possible explanation for this behavior could again be an oriented source mechanism or a material contrast between the northern and the southern part of the mountain. Again, the amplification factors for station RTSH decrease with increasing frequency which confirms the argumentation made within the analysis of event 1. Additionally, we want to remark, that similar to event 1, the simulation shows less deviation from the reference value than the measured data in general.

For event 3 (Tab. 5.10 (c)), only three stations were active within the considered region. As expected, the stations RJOB and RMOA, both located at the base of a slope, show a deamplification of PGV in real data. As RMOA is further away from the hypocenter than RJOB, we rectify the distance dependence of PGVs again. The corrected results are 0.63 for RJOB and 0.51 for RMOA. As expected, these two values are close to each other, because both stations have similar locations with respect to topography.
The synthetic data for the simulations of explosive sources do not coincide with the real data. At least, like for real data, the values for RJOB are higher than for RMOA, which can be explained by geometric spreading. Moreover, the observed deamplifications are not observed in the simulations, but instead an amplification is measured.

Now, we examine the results obtained by simulating the events using

double-couple point sources. The sources are created as low-pass filtered versions of a Gaussian pulse with a flat spectrum between either 0 and 4 Hz or between 0 and 10 Hz.

First, we regard an arbitrarily oriented, inclined source with strike $= 260°$, dip $= 40°$ and rake $= 90°$ for the lower frequency spectrum. Comparing the amplification factors PGV^4_{double} for each event to synthetic data of explosive sources, we get improved results for event 3, worse amplification factors for event 2 and for event 1 it depends on the station whether the PGVs are closer to real data or not. Therefore, we conclude, that ground motion depends enormously on the source mechanism and orientation.

In order to estimate the range in which an amplification factor should lie comprising the possible orientations of double-couple sources, we perform two further simulations for event 2. Here, we use the maximum frequency of 10 Hz, as in this way, due to the different velocities, the P-wave arrival can clearly be separated from the S-wave arrival for the seismograms recorded at the stations. In one simulation, the source orientation is determined by strike $= 0°$, dip $= 90°$ and rake $= 90°$, which means, that the radiation in vertical direction is maximal for P-waves and minimal for S-waves. Therefore, we refer to the results of this simulation by PGV^{10p}_{double}. For the second simulation the source is rotated by $45°$ (strike $= 180°$, dip $= 45°$ and rake $= -90°$), leading to a maximum for S-waves and a minimum for P-waves in vertical direction. In this case, we denote the results as PGV^{10s}_{double}. As the station RTSH is located close to vertical above the source, it is well suited for this study. However, in order to exclude any other effects of directional characteristics, we discuss the absolute PGV values of the station RTSH directly without weighting the results by the reference station.

For both simulations we observe stronger P-waves than S-waves. We obtain $PGV^{10p}_{double} = 67.69 \,\mu m/s$ as an upper limit and $PGV^{10s}_{double} = 60.99 \,\mu m/s$ as a lower limit. However, we observe a value of $PGV^{10i}_{double} = 82.45 \,\mu m/s$ for an inclined source (as described above) of 10 Hz, which clearly lies beyond this range. On the one hand, this example shows, that the source orientation is important, but on the other hand, we see that topographic effects might dominate, as this last value exceeds the assumed upper limit. Hence, we conclude, that topography should not be neglected.

5.2.3　Discussion

In this section, we first confirmed the general observations for plane body waves arriving at the surface of the systematic parameter study of Sec. 5.1 for the region of Mt. Hochstaufen. Afterwards, we focused on surface waves. Depending on the frequency of the incoming Rayleigh waves, the area behind Mt. Hochstaufen can be shielded from ground shaking up to 90%. The area in front of the mountain suffers from reflections by the massif and thus PGVs get amplified in this part of the computational domain.

Our next study concentrated on three local events for which real data was available. In order to isolate topographic effects, we used homogeneous material parameters for the simulation of these events. Synthetic data was compared to real data by computing amplification factors of peak ground velocity between each station and a reference station in the valley.

We found out, that the observed amplification factors cannot be explained by topographic effects alone in general. For a few receivers we discover differences up to a factor of 4. However, some of the numerical results represent real observations quite well. Simulations of explosive sources show the best agreements to a large extent. Using double-couple sources the conformance to real measurements strongly depends on the source orientation. Therefore, we conclude, that also the source mechanism and orientation display a decisive role. The synthetic data of our study usually underestimate the effects observed in reality, which is a known problem in literature.

Summarizing, we have learnt, that topography should be taken into account when simulating seismic wave propagation, as its effects can drastically influence the results. However, also other parameterizations like e.g. material properties, a weathering layer and further site-effects can influence the results significantly and therefore should not be excluded.

Chapter 6

Conclusions

In this work we analyzed, further developed and applied the Discontinuous Galerkin (DG) method which uses an arbitrary high order of derivatives (ADER) for the time discretization. For this purpose, we first introduced the ADER-DG method as a numerical solver for the elastic wave equation on tetrahedral and hexahedral meshes in 3 dimensions.

A comprehensive accuracy analysis based on the time-frequency representation of the seismogram misfits was carried out. We found out, that the phase misfit is always lower than the amplitude misfit for the ADER-DG method. A further result is, that in general using higher approximation orders in combination with coarser meshes reduces the runtime for the same numerical accuracy. Moreover, computations on hexahedral meshes perform faster than on tetrahedral meshes. However, geometrical constraints often prohibit the use of very coarse or hexahedral meshes. Therefore, the study presents thorough relationships between the used mesh spacing, the expected number of propagated wavelengths and the chosen approximation order of the numerical scheme to reach a desired error level. We confirmed our results by two benchmark testcases of the *Seismic wave Propagation and Imaging in Complex media: a European network* (SPICE) code validation project. In this context, we clearly saw, that the major misfits follow from reflections at artificial boundaries.

According to the results of our accuracy study, we improved the performance of the ADER-DG method in consideration of two aspects. Firstly, we extended the scheme for non-conforming, hybrid meshes in two space-dimensions. This enables us to simultaneously use unstructured meshes in regions of complex geometry and regular meshes throughout the rest of the computational domain

125

which can lead to a clear reduction of runtime due to an optimal adaptation of the mesh spacing to the physical and geometrical properties of the problem. To verify our implementation we performed numerical convergence tests up to 9-th order and examined several test cases including different kinds of non-conforming interfaces, a strong material contrast between a thin surface layer and a homogeneous halfspace, and an application to a realistic scenario based on a modified benchmark for a 2-dimensional cross-section of the region of Grenoble. The parallel version of the code works satisfying. Nevertheless, it is part of future work to test various (or develop new) mesh partitioners with respect to their capabilities of partitioning non-conforming, hybrid meshes more efficiently. Moreover, due to the motivating results of this work, we are currently introducing the combination of tetrahedral and hexahedral meshes in 3 dimensions.

Secondly, we achieved a convolutional perfectly matched layer (CPML) surrounding the computational domain in order to reduce the spurious reflections at imperfect absorbing boundaries. In some test cases the CPML reduces artificial reflections by one order of magnitude. Admittedly, we discovered test cases for which instabilities emerge when using the CPML. As the behavior of the scheme cannot be predicted, we introduced an energy criterion, that controls the stability. In case of a growing divergence, the CPML is switched off and the system returns to common absorbing boundary conditions, which are stable but less efficient.

Finally, we performed an application of the ADER-DG method to a systematic parameter study of topographic effects on seismic wave propagation. For the first part of this analysis we examined the region of Grenoble, France, which includes valleys and plateaus, i.e., flat areas, as well as high mountains and steep slopes. We investigated ground motion characteristics for different frequencies of the input signals within a range of $0.25 - 2\,\mathrm{Hz}$, for variable resolutions of the underlying dataset which describes the surface, for varying strengths of the topographic relief and for diverse body wave types, i.e., compressional and shear waves.
The main results of this study are the following: Topography has a great impact on peak ground motion. Peak ground velocity (PGV) reaches highest values at mountain ridges or tops, whereas at the lower parts of steep slopes we observe a deamplification of PGV in general. The highest amplification of PGV in this study was a factor of 2.48. With increasing frequency the PGV pattern becomes more detailed and topographic features on a finer scale predominate the effects on ground motion. Therefore, the dataset resolution for topographic models should be adapted appropriately to the highest considered frequency, i.e. the shortest

considered wavelength. As a rough estimation, we suggest the user to take a dataset resolution of the eighth part of the shortest wavelength. A drastic over-sampling does not change the results. Regarding different amplification factors of the topography, it becomes even more evident how important it is, to comprise topography in numerical simulations. By increasing the strength of the topographic relief the extremal values of PGV are growing drastically. Body waves polarized in horizontal direction (SX- and SY-waves) are influenced much more by topography than vertically polarized waves (P-waves). SX-waves are primarily influenced by topographic structures elongated in y-direction and vice versa.

The second part of our topography study treated the region of Mt. Hochstaufen, Southern Bavaria, where seismograms of real recordings are available. Here, we used a fixed dataset resolution and only considered real topography. After confirming the results of the previous part for different body wave types and various frequencies in a range of $1 - 20\,\mathrm{Hz}$, we examined topographic effects on surface waves. We found out that, depending on the frequency of the incoming Rayleigh waves, the area behind Mt. Hochstaufen can be shielded from ground shaking up to 90%. Next, we simulated some local events in order to compare PGV amplification factors to real measurements. In order to isolate topographic effects, we assumed homogeneous material properties throughout the computational domain. Although the computed amplification factors resemble the amplification factors of real measurements for some selected stations and events, we conclude that the observed amplification factors cannot be explained by the mere topography effect itself.

Summarizing, we can say, that topography should be taken into account when simulating seismic wave propagation, as its effects can drastically influence the results. Our analysis leaves a lot of space for further investigations. The impact on surface waves, e.g., could be examined in more detail and a systematic study of different orientations of double-couple point sources as well as the investigation of source mechanisms in connection to topography in general is subject to further research.

Appendix A

Orthogonal Basis Functions

In our implementation, the ADER-DG method works with the orthogonal hierarchical Dubiner's basis functions (see [47]). Hierarchical means, that every set of basis functions of degree N includes all basis functions of all lower degrees as a subset. The basis functions are given in terms of the Jacobi polynomials $P_n^{\alpha,\beta}(x)$, which are solutions of the Jacobi differential equation

$$(1 - x^2)y'' + \left[\beta - \alpha - (\alpha + \beta + 2)x\right]y' + n(n + \alpha + \beta + 1)y = 0 \,. \qquad \text{(A.1)}$$

In the interval $[-1, 1]$ the polynomials read

$$P_n^{\alpha,\beta}(x) = \frac{(-1)^n}{2^n n!}(1 - x)^{-\alpha}(1 + x)^{-\beta}\frac{d^n}{dx^n}\left[(1 - x)^{\alpha+n}(1 + x)^{\beta+n}\right] \,. \qquad \text{(A.2)}$$

For $\alpha = \beta = 0$ the Jacobi polynomials $P_n^{0,0}(x)$ reduce to the Legendre polynomials. We construct the DG basis functions as products of up to the three primal functions

$$
\begin{aligned}
\theta_i^a(x) &= P_i^{0,0}(x) \,, \\
\theta_{ij}^b(x) &= \left(\frac{1 - x}{2}\right)^i P_j^{2i+1,0}(x) \,, \\
\theta_{ijk}^c(x) &= \left(\frac{1 - x}{2}\right)^{i+j} P_k^{2i+2j+2,0}(x) \,.
\end{aligned}
\qquad \text{(A.3)}
$$

A.1   Triangular Elements

For triangles the reference element $\mathcal{E}_{ref}$ is defined as

$$\mathcal{E}_{ref} = \left\{ (\xi, \eta) \in \mathbb{R}^2 \mid 0 \leq \xi \leq 1 \ \wedge \ 0 \leq \eta \leq 1 - \xi \right\} . \tag{A.4}$$

The basis functions $\Phi_k(\xi, \eta)$ on this reference element are given by the following product of primal functions:

$$\Phi_{k(p,q)}(\xi, \eta) = \Theta_p^a(\alpha) \cdot \Theta_{pq}^b(\beta) , \tag{A.5}$$

with

$$\alpha = \frac{2\,\xi}{1 - \eta} , \quad \beta = 2\,\eta - 1 . \tag{A.6}$$

The mono-index $k = k(p, q)$ is a function of the index couple (p, q). For a fourth order scheme (of polynomial degree $N = 3$) the two-dimensional basis functions read

$$\Phi_0 = 1 ,$$

$$\Phi_1 = -1 + 2\,\xi + \eta ,$$

$$\Phi_2 = -1 + 3\,\eta ,$$

$$\Phi_3 = 1 - 6\,\xi + 6\,\xi^2 - 2\,\eta + 6\,\xi\eta + \eta^2 ,$$

$$\Phi_4 = 1 - 2\,\xi - 6\,\eta + 10\,\xi\eta + 5\,\eta^2 ,$$

$$\Phi_5 = 1 - 8\,\eta + 10\,\eta^2 ,$$

$$\Phi_6 = -1 + 12\,\xi - 30\,\xi^2 + 20\,\xi^3 + 3\,\eta - 24\,\xi\eta + 30\,\xi^2\eta - 3\eta^2 + 12\,\xi\eta^2 + \eta^3 ,$$

$$\Phi_7 = -1 + 6\,\xi - 6\,\xi^2 + 9\,\eta - 48\,\xi\eta + 42\,\xi^2\eta - 15\,\eta^2 + 42\,\xi\eta^2 + 7\,\eta^3 ,$$

$$\Phi_8 = -1 + 2\,\xi + 13\,\eta - 24\,\xi\eta - 33\,\eta^2 + 42\,\xi\eta^2 + 21\,\eta^3 ,$$

$$\Phi_9 = -1 + 15\,\eta - 45\,\eta^2 + 35\,\eta^3 . \tag{A.7}$$

A.2   Quadrangular Elements

For quadrilaterals the reference element $\mathcal{E}_{ref}$ is defined as

$$\mathcal{E}_{ref} = \left\{ (\xi, \eta) \in \mathbb{R}^2 \mid 0 \leq \xi \leq 1 \ \wedge \ 0 \leq \eta \leq 1 \right\} . \tag{A.8}$$

The basis functions $\Phi_k(\xi, \eta)$ on this reference element are given by the following product of primal functions:

$$\Phi_{k(p,q)}(\xi, \eta) = \Theta_p^a(\alpha) \cdot \Theta_q^a(\beta) , \tag{A.9}$$

with

$$\alpha = 2\,\xi - 1, \quad \beta = 2\,\eta - 1 . \tag{A.10}$$

The mono-index $k = k(p, q)$ is again a function of the index couple (p, q). For a fourth order scheme (of polynomial degree $N = 3$) the two-dimensional basis functions read

$$
\begin{aligned}
\Phi_0 &= 1 , \\
\Phi_1 &= -1 + 2\,\xi , \\
\Phi_2 &= -1 + 2\,\eta , \\
\Phi_3 &= 1 - 6\,\xi + 2\,\xi^2 , \\
\Phi_4 &= 1 - 2\,\xi - 2\,\eta + 4\,\xi\eta , \\
\Phi_5 &= 1 - 6\,\eta + 6\,\eta^2 , \\
\Phi_6 &= -1 - 12\,\xi - 30\,\xi^2 + 20\,\xi^3 , \\
\Phi_7 &= -1 + 6\,\xi - 6\,\xi^2 + 2\,\eta - 12\,\xi\eta + 12\,\xi^2\eta , \\
\Phi_8 &= -1 + 2\,\xi + 6\,\eta - 12\,\xi\eta - 6\,\eta^2 + 12\,\xi\eta , \\
\Phi_9 &= -1 + 12\,\eta - 30\,\eta^2 + 20\,\eta^3 .
\end{aligned}
\tag{A.11}
$$

A.3   Tetrahedral Elements

For tetrahedrons the reference element $\mathcal{E}_{ref}$ is defined as

$$\mathcal{E}_{ref} = \left\{ (\xi, \eta, \zeta) \in \mathbb{R}^3 \mid 0 \le \xi \le 1 \wedge 0 \le \eta \le 1 - \xi \wedge 0 \le \zeta \le 1 - \xi - \eta \right\}. \tag{A.12}$$

The basis functions $\Phi_k(\xi, \eta, \zeta)$ on this reference element are given by the following product of primal functions:

$$\Phi_{k(p,q,r)}(\xi, \eta, \zeta) = \Theta_p^a(\alpha) \cdot \Theta_{pq}^b(\beta) \cdot \Theta_{pqr}^c(\gamma) , \tag{A.13}$$

with

$$\alpha = \frac{\eta - 1 + \zeta + 2\,\xi}{1 - \eta - \zeta}, \quad \beta = \frac{2\,\eta - 1 + \zeta}{1 - \zeta}, \quad \gamma = 2\,\zeta - 1. \tag{A.14}$$

The mono-index $k = k(p, q, r)$ is a function of the index triple (p, q, r). For a third order scheme (of polynomial degree $N = 2$) the three-dimensional basis functions read

$$
\begin{aligned}
\Phi_0 &= 1\,, \\
\Phi_1 &= -1 + 2\,\xi + \eta + \zeta\,, \\
\Phi_2 &= -1 + 3\,\eta + \zeta\,, \\
\Phi_3 &= -1 + 4\,\zeta\,, \\
\Phi_4 &= 1 - 6\,\xi + 6\,\xi^2 - 2\,\eta + 6\,\xi\eta + \eta^2 - 2\,\zeta + 6\,\xi\zeta + 2\eta\zeta + \zeta^2\,, \\
\Phi_5 &= 1 - 2\,\xi - 6\,\eta + 10\,\xi\eta + 5\,\eta^2 - 2\,\zeta + 2\,\xi\zeta + 6\,\eta\zeta + \zeta^2\,, \\
\Phi_6 &= 1 - 8\,\eta + 10\,\eta^2 - 2\,\zeta + 8\,\eta\zeta + \zeta^2\,, \\
\Phi_7 &= 1 - 2\,\xi - \eta - 7\,\zeta + 12\,\xi\zeta + 6\,\eta\zeta + 6\,\zeta^2\,, \\
\Phi_8 &= 1 - 3\,\eta - 7\,\zeta + 18\,\eta\zeta + 6\,\zeta^2\,, \\
\Phi_9 &= 1 - 10\,\zeta + 15\,\zeta^2\,.
\end{aligned}
\tag{A.15}
$$

A.4   Hexahedral Elements

For hexahedrons the reference element $\mathcal{E}_{ref}$ is defined as

$$\mathcal{E}_{ref} = \left\{ (\xi, \eta, \zeta) \in \mathbb{R}^3 \mid 0 \le \xi \le 1 \ \wedge \ 0 \le \eta \le 1 \ \wedge \ 0 \le \zeta \le 1 \right\}. \tag{A.16}$$

The basis functions $\Phi_k(\xi, \eta, \zeta)$ on this reference element are given by the following product of primal functions:

$$\Phi_{k(p,q,r)}(\xi, \eta, \zeta) = \Theta_p^a(\alpha) \cdot \Theta_q^a(\beta) \cdot \Theta_r^a(\gamma)\,, \tag{A.17}$$

with

$$\alpha = 2\,\xi - 1, \quad \beta = 2\,\eta - 1, \quad \gamma = 2\,\zeta - 1. \tag{A.18}$$

The mono-index $k = k(p, q, r)$ is again a function of the index triple (p, q, r). For a third order scheme (of polynomial degree $N = 2$) the three-dimensional basis functions read

$$
\begin{aligned}
\Phi_0 &= 1, \\
\Phi_1 &= -1 + 2\xi, \\
\Phi_2 &= -1 + 2\eta, \\
\Phi_3 &= -1 + 2\zeta, \\
\Phi_4 &= 1 - 6\xi + 6\xi^2, \\
\Phi_5 &= 1 - 2\xi - 2\eta + 4\xi\eta, \\
\Phi_6 &= 1 - 6\eta + 6\eta^2, \\
\Phi_7 &= 1 - 2\xi - 2\zeta + 4\xi\zeta, \\
\Phi_8 &= 1 - 2\eta - 2\zeta + 4\eta\zeta, \\
\Phi_9 &= 1 - 6\zeta + 6\zeta^2.
\end{aligned}
\tag{A.19}
$$

Appendix B

Coordinate Transformation

B.1 Triangular Elements

The transformation of a triangular in the global Cartesian $xy-$coordinate system to the local Cartesian $\xi\eta-$coordinate system of the reference triangular is defined by

$$\xi = \frac{1}{|\mathbf{J}|}\left((x_3y_1 - x_1y_3) + x(y_3 - y_1) + y(x_1 - x_3)\right),$$

$$\eta = \frac{1}{|\mathbf{J}|}\left((x_1y_2 - x_2y_1) + x(y_1 - y_2) + y(x_2 - x_1)\right), \tag{B.1}$$

where the $x_i, y_i\,(i = 1, \ldots, 3)$ are the vertex coordinates of the triangle. $|\mathbf{J}|$ is the determinant of the Jacobian matrix

$$|\mathbf{J}| = (x_2 - x_1)(y_3 - y_1) - (x_3 - x_1)(y_2 - y_1), \tag{B.2}$$

which is equal to twice the triangle's surface. The reverse transformation is given by

$$x = x_1 + (x_2 - x_1)\xi + (x_3 - x_1)\eta,$$

$$y = y_1 + (y_2 - y_1)\xi + (y_3 - y_1)\eta. \tag{B.3}$$

B.2 Quadrangular Elements

The transformation of a quadrilateral in the global Cartesian $xy-$coordinate system to the local Cartesian $\xi\eta-$coordinate system of the reference quadrilateral is

defined by

$$\xi = \frac{1}{|\mathbf{J}|}(x_1 - x)(y_3 - y_1),$$

$$\eta = \frac{1}{|\mathbf{J}|}(x_2 - x_1)(y - y_1), \tag{B.4}$$

where the x_i, y_i ($i = 1, \ldots, 4$) are the vertex coordinates of the quadrilateral. $|\mathbf{J}|$ is the determinant of the Jacobian matrix

$$|\mathbf{J}| = (x_2 - x_1)(y_3 - y_1). \tag{B.5}$$

The reverse transformation is given by

$$x = (1 - \xi)(1 - \eta)x_1 + \xi(1 - \eta)x_2 + \xi\eta x_3 + (1 - \xi)\eta x_4,$$

$$y = (1 - \xi)(1 - \eta)y_1 + \xi(1 - \eta)y_2 + \xi\eta y_3 + (1 - \xi)\eta y_4. \tag{B.6}$$

B.3   Tetrahedral Elements

The transformation of a tetrahedron in the global Cartesian $xyz-$coordinate system to the local Cartesian $\xi\eta\zeta-$coordinate system of the reference tetrahedron

is defined by

$$\xi = \frac{1}{|\mathbf{J}|}\Big[x_1(y_4z_3 - y_3z_4) + x_3(y_1z_4 - y_4z_1) + x_4(y_3z_1 - y_1z_3) +$$

$$\Big(y_1(z_3 - z_4) + y_3(z_4 - z_1) + y_4(z_1 - z_3)\Big)x +$$

$$\Big(x_1(z_4 - z_3) + x_3(z_1 - z_4) + x_4(z_3 - z_1)\Big)y +$$

$$\Big(x_1(y_3 - y_4) + x_3(y_4 - y_1) + x_4(y_1 - y_3)\Big)z\Big],$$

$$\eta = \frac{1}{|\mathbf{J}|}\Big[y_1(x_4z_2 - x_2z_4) + y_2(x_1z_4 - x_4z_1) + y_4(x_2z_1 - x_1z_2) +$$

$$\Big(y_1(z_4 - z_2) + y_2(z_1 - z_4) + y_4(z_2 - z_1)\Big)x +$$

$$\Big(x_1(z_2 - z_4) + x_2(z_4 - z_1) + x_4(z_1 - z_2)\Big)y +$$

$$\Big(x_1(y_4 - y_2) + x_2(y_1 - y_4) + x_4(y_2 - y_1)\Big)z\Big],$$

$$\zeta = \frac{1}{|\mathbf{J}|}\Big[z_1(x_3y_2 - x_2y_3) + z_2(x_1y_3 - x_3y_1) + z_3(x_2y_1 - x_1y_2) +$$

$$\Big(y_1(z_2 - z_3) + y_2(z_3 - z_1) + y_3(z_1 - z_2)\Big)x +$$

$$\Big(x_1(z_3 - z_2) + x_2(z_1 - z_3) + x_3(z_2 - z_1)\Big)y +$$

$$\Big(x_1(y_2 - y_3) + x_2(y_3 - y_1) + x_3(y_1 - y_2)\Big)z\Big], \tag{B.7}$$

where the x_i, y_i and z_i $(i = 1, \ldots, 4)$ are the vertex coordinates of the tetrahedron. $|\mathbf{J}|$ is the determinant of the Jacobian matrix:

$$|\mathbf{J}| = x_1\Big[y_2(z_4 - z_3) + y_3(z_2 - z_4) + y_4(z_3 - z_2)\Big] +$$

$$x_2\Big[y_1(z_3 - z_4) + y_3(z_4 - z_1) + y_4(z_1 - z_3)\Big] +$$

$$x_3\Big[y_1(z_4 - z_2) + y_2(z_1 - z_4) + y_4(z_2 - z_1)\Big] +$$

$$x_4\Big[y_1(z_2 - z_3) + y_2(z_3 - z_1) + y_3(z_1 - z_2)\Big]. \tag{B.8}$$

The reverse transformation is given by

$$
\begin{aligned}
x &= x_1 + (x_2 - x_1)\xi + (x_3 - x_1)\eta + (x_4 - x_1)\zeta \,, \\
y &= y_1 + (y_2 - y_1)\xi + (y_3 - y_1)\eta + (y_4 - y_1)\zeta \,, \\
z &= z_1 + (z_2 - z_1)\xi + (z_3 - z_1)\eta + (z_4 - z_1)\zeta \,.
\end{aligned}
\tag{B.9}
$$

B.4 Hexahedral Elements

The transformation of a hexahedron in the global Cartesian $xyz-$coordinate system to the local Cartesian $\xi\eta\zeta-$coordinate system of the reference hexahedron is defined by

$$
\begin{aligned}
\xi = \frac{1}{|\mathbf{J}|}\Big[& x_1(y_5 z_3 - y_3 z_5) + x_3(y_1 z_5 - y_5 z_1) + x_5(y_3 z_1 - y_1 z_3) + \\
& \Big(y_1(z_3 - z_5) + y_3(z_5 - z_1) + y_5(z_1 - z_3) \Big) x + \\
& \Big(x_1(z_5 - z_3) + x_3(z_1 - z_5) + x_5(z_3 - z_1) \Big) y + \\
& \Big(x_1(y_3 - y_5) + x_3(y_5 - y_1) + x_5(y_1 - y_3) \Big) z \Big] \,, \\
\eta = \frac{1}{|\mathbf{J}|}\Big[& y_1(x_5 z_2 - x_2 z_5) + y_2(x_1 z_5 - x_5 z_1) + y_5(x_2 z_1 - x_1 z_2) + \\
& \Big(y_1(z_5 - z_2) + y_2(z_1 - z_5) + y_5(z_2 - z_1) \Big) x + \\
& \Big(x_1(z_2 - z_5) + x_2(z_5 - z_1) + x_5(z_1 - z_2) \Big) y + \\
& \Big(x_1(y_5 - y_2) + x_2(y_1 - y_5) + x_5(y_2 - y_1) \Big) z \Big] \,, \\
\zeta = \frac{1}{|\mathbf{J}|}\Big[& z_1(x_3 y_2 - x_2 y_3) + z_2(x_1 y_3 - x_3 y_1) + z_3(x_2 y_1 - x_1 y_2) + \\
& \Big(y_1(z_2 - z_3) + y_2(z_3 - z_1) + y_3(z_1 - z_2) \Big) x + \\
& \Big(x_1(z_3 - z_2) + x_2(z_1 - z_3) + x_3(z_2 - z_1) \Big) y + \\
& \Big(x_1(y_2 - y_3) + x_2(y_3 - y_1) + x_3(y_1 - y_2) \Big) z \Big] \,,
\end{aligned}
\tag{B.10}
$$

where the x_i, y_i and z_i ($i = 1, \ldots, 8$) are the vertex coordinates of the hexahedron. $|\mathbf{J}|$ is the determinant of the Jacobian matrix:

$$
\begin{aligned}
|\mathbf{J}| \quad = \quad & x_1 \Big[y_2(z_5 - z_3) + y_3(z_2 - z_5) + y_5(z_3 - z_2) \Big] + \\
& x_2 \Big[y_1(z_3 - z_5) + y_3(z_5 - z_1) + y_5(z_1 - z_3) \Big] + \\
& x_3 \Big[y_1(z_5 - z_2) + y_2(z_1 - z_5) + y_5(z_2 - z_1) \Big] + \\
& x_5 \Big[y_1(z_2 - z_3) + y_2(z_3 - z_1) + y_3(z_1 - z_2) \Big] .
\end{aligned}
\tag{B.11}
$$

The reverse transformation is given by

$$
\begin{aligned}
x \quad = \quad & x_1 + (x_2 - x_1)\xi + (x_3 - x_1)\eta + (x_5 - x_1)\zeta + \\
& (x_1 - x_2 + x_4 - x_3)\xi\eta + (x_1 - x_2 + x_6 - x_5)\xi\zeta + \\
& (x_1 - x_3 + x_7 - x_5)\eta\zeta + \\
& (x_2 - x_1 + x_3 - x_4 + x_5 - x_6 + x_8 - x_7)\xi\eta\zeta , \\
y \quad = \quad & y_1 + (y_2 - y_1)\xi + (y_3 - y_1)\eta + (y_5 - y_1)\zeta + \\
& (y_1 - y_2 + y_4 - y_3)\xi\eta + (y_1 - y_2 + y_6 - y_5)\xi\zeta + \\
& (y_1 - y_3 + y_7 - y_5)\eta\zeta + \\
& (y_2 - y_1 + y_3 - y_4 + y_5 - y_6 + y_8 - y_7)\xi\eta\zeta , \\
z \quad = \quad & z_1 + (z_2 - z_1)\xi + (z_3 - z_1)\eta + (z_5 - z_1)\zeta + \\
& (z_1 - z_2 + z_4 - z_3)\xi\eta + (z_1 - z_2 + z_6 - z_5)\xi\zeta + \\
& (z_1 - z_3 + z_7 - z_5)\eta\zeta + \\
& (z_2 - z_1 + z_3 - z_4 + z_5 - z_6 + z_8 - z_7)\xi\eta\zeta .
\end{aligned}
\tag{B.12}
$$

Appendix C

Equivalent Formulations for the CPML

Having derived a different formulation for the CPML than Komatitsch and Martin [73], we want to proof the equivalence of both approaches. We recall Eq. (4.7)

$$\frac{\partial \phi_{pi}}{\partial t} = -\frac{d_i}{\kappa_i^2} \frac{\partial Q_p}{\partial i} - \left(\frac{d_i}{\kappa_i} + \alpha_i \right) \phi_{pi} , \qquad (C.1)$$

which describes the time evolution of the memory variables ϕ_{pi}, and define

$$\beta_i \equiv \frac{d_i}{\kappa_i} + \alpha_i . \qquad (C.2)$$

The general solution of this first-order linear differential equation is given by

$$\phi_{pi} \, e^{\beta t} = -\frac{d_i}{\kappa_i^2} \int_{-\infty}^{t} e^{\beta \tau} \frac{\partial Q_p}{\partial i} \, d\tau , \qquad (C.3)$$

where we neglect a potential, additional, constant term. We discretize Eq. (C.3) using $t = (n+1)\Delta t$ and presume ∂_i to be constant within the interval $[n, n+1]\Delta t$ now. Like Komatitsch and Martin we set this derivative equal to $\partial_i^{n+1/2}$. In order to distinguish between different time levels, we attach a superscript to the memory variables. We can split the time integral into

$$\phi_{pi}^{n+1} \, e^{\beta(n+1)\Delta t} =$$

$$-\frac{d_i}{\kappa_i^2} \int_{-\infty}^{n\Delta t} e^{\beta \tau} \frac{\partial Q_p}{\partial i} \, d\tau - \frac{d_i}{\kappa_i^2} \int_{n\Delta t}^{(n+1)\Delta t} e^{\beta \tau} \frac{\partial^{n+1/2} Q_p}{\partial i} \, d\tau . \qquad (C.4)$$

The first term of Eq. (C.4) is equal to the solution of the previous time level and after integrating the second term, we arrive at

$$\phi_{pi}^{n+1}\, e^{\beta(n+1)\Delta t} = \phi_{pi}^{n}\, e^{\beta n \Delta t} - \frac{d_i}{\beta \kappa_i^2} \left(e^{\beta(n+1)\Delta t} - e^{\beta n \Delta t} \right) \frac{\partial^{n+1/2} Q_p}{\partial i}\,. \tag{C.5}$$

Dividing both sides by $e^{\beta(n+1)\Delta t}$ and using the identities like [73]

$$a_i = -\frac{d_i}{\beta \kappa_i^2} \left(1 - e^{\beta \Delta t} \right) \quad \text{and} \quad b_i = 1 - e^{\beta \Delta t}\,, \tag{C.6}$$

leads to

$$\phi_{pi}^{n+1} = b_i \phi_{pi}^{n} + a_i \frac{\partial^{n+1/2} Q_p}{\partial i}\,, \tag{C.7}$$

which is the evolution equation for the staggered FD scheme derived by Komatitsch and Martin. We want to mention that their main assumption is the constant derivative ∂_i within one timestep whereas the ADER-DG scheme provides high-order solutions due to the polynomial description of the degrees of freedom for this time interval.

References

[1] R. Madariaga, *Dynamics of an expanding circular fault, Bull. Seism. Soc. Am.* **66**, 639–666 (1976).

[2] J. Virieux, *SH-wave propagation in heterogeneous media: Velocity-stress finite-difference method, Geophysics* **49**, 1933–1942 (1984).

[3] J. Virieux, *P-SV wave propagation in heterogeneous media: Velocity-stress finite-difference method, Geophysics* **51**, 889–901 (1986).

[4] P. Moczo, J. Kristek, M. Galis, P. Pazak, and M. Balazovjech, *The finite-difference and finite-element modeling of seismic wave propagation and earthquake motion, Acta physica slovaca* **57(2)**, 177–406 (2007).

[5] P. Moczo, J. O. A. Robertsson, and L. Eisner, *The finite-difference time-domain method for modeling of seismic wave propagation*, vol. 48. Elsevier - Academic Press, 2007.

[6] B. Fornberg, *On a fourier method for the integration of hyperbolic equations*, vol. 12. Soc. Industr. Appl. Math., J. Num. Anal., 1975.

[7] J. M. Carcione, *The wave equation in generalised coordinates, Geophysics* **59**, 1911–1919 (1994).

[8] B. Fornberg, *A Practical Guide to Pseudospectral Methods.* Cambridge University Press, 1996.

[9] K. Marfurt, *Accuracy of finite-difference and finite-element modeling of the scalar and elastic wave equations, Geophysics* **49**, 533–549 (1984).

[10] C. Yoshimura, J. Bielak, Y. Hisada, and A. Fernández, *Domain reduction method for three-dimensional earthquake modeling in localized regions. Part II: Verification and applications, Bull. Seism. Soc. Am.* **93**, 825–84 (2003).

[11] Y. H. J. Bielak, K. Loukakis and C. Yoshimura, *Domain reduction method for three-dimensional earthquake modeling in localized regions. part I: Theory*, Bull. Seism. Soc. Am. **93**, 817–824 (2003).

[12] K. Koketsu, H. Fujiwara, and Y. Ikegami, *Finite-element simulation of seismic ground motion with a voxel mesh*, Pure appl. geophys. **161**, 2183–219 (2004).

[13] G. Seriani and E. Priolo, *Spectral element method for acoustic wave simulation in heterogeneous media*, Finite Element in Analysis and Design **16**, 337–348 (1994).

[14] D. Komatitsch and J. P. Vilotte, *The spectral-element method: an efficient tool to simulate the seismic response of 2D and 3D geological structures*, Bull. Seism. Soc. Am. **88**, 368–392 (1998).

[15] D. Komatitsch, Q. Liu, J. Tromp, P. Süss, C. Stidham, and J. H. Shaw, *Simulations of ground motion in the Los Angeles basin based upon the spectral element method*, Bull. Seism. Soc. Am. **149**, 390–412 (2004).

[16] E. Chaljub, Y. Capdeville, and J.-P. Vilotte, *Solving elastodynamics in a fluid-solid heterogeneous sphere: a parallel spectral element approximation on non-conforming grids*, J. Comput. Phys. **187(2)**, 457–491 (2003).

[17] E. Chaljub, D. Komatitsch, J.-P. Vilotte, Y. Capdeville, B. Valette, and G. Festa, *Spectral-Element Analysis in Seismology*, Advances in Geophysics **48**, 365–419 (2007).

[18] M. Bouchon and F. J. Sánchez-Sesma, *Boundary integral equations and boundary elements methods in elastodynamics*, Advances in Geophysics **48**, 157–189 (2007).

[19] M. Käser and M. Dumbser, *An Arbitrary High Order Discontinuous Galerkin Method for Elastic Waves on Unstructured Meshes I: The Two-Dimensional Isotropic Case with External Source Terms*, Geophys. J. Int. **166(2)**, 855–877 (2006).

[20] M. Dumbser and M. Käser, *An Arbitrary High Order Discontinuous Galerkin Method for Elastic Waves on Unstructured Meshes II: The Three-Dimensional Case*, Geophys. J. Int. **167(1)**, 319–336 (2006).

144

[21] M. Kristeková, J. Kristek, P. Moczo, and S. Day, *Misfit Criteria for Quantitative Comparison of Seismograms*, Bull. Seism. Soc. Am. **96(5)**, 1836–1850 (2006).

[22] T. Ichimura, M. Hori, and H. Kuwamoto, *Earthquake Motion Simulation with Multiscale Finite-Element Analysis on Hybrid Grid*, Bull. Seism. Soc. Am. **97**, 1133–1143 (2007).

[23] T. Ichimura, M. Hori, and J. Bielak, *A hybrid multiresolution meshing technique for finite element three-dimensional earthquake ground motion modelling in basins inclding topography*, Geophys. J. Int. **177**, 1221–1232 (2009).

[24] J.-P. Berenger, *A Perfectly Matched Layer for the absorption of electromagnetic waves*, J. Comput. Phys. **114**, 185–200 (1994).

[25] J. Roden and S. Gedney, *Convolution PML (CPML): an efficient FDTD implementation of the CFS-PML for arbitrary media*, Microw. Opt. Technol. Lett. **27**, 334–339 (2000).

[26] M. Bouchon, *Effect of topography on surface motion*, Bull. Seism. Soc. Am. **63(3)**, 615–632 (1973).

[27] D. W. Griffiths and G. A. Bollinger, *The effect of Appalachian Mountain topography on seismic waves*, Bull. Seism. Soc. Am. **69(4)**, 1081–1105 (1979).

[28] S. Ma, R. J. Archuleta, and M. T. Page, *Effects of Large-Scale Surface Topography on Ground Motions, as Demonstrated by a Study of the San Gabriel Mountains, Los Angeles, California*, Bull. Seism. Soc. Am. **97(6)**, 2066–2079 (2007).

[29] S.-J. Lee, Y.-C. Chan, D. Komatitsch, B.-S. Huang, and J. Tromp, *Effects of Realistic Surface Topography on Seismic Ground Motion in the Yangminshan Region of Taiwan Based Upon the Spectral-Element Method and LiDAR DTM*, Bull. Seism. Soc. Am. **99(2A)**, 681–693 (2009).

[30] A. R. Levander, *Fourth-order finite difference P-SV seismograms*, Geophysics **53**, 1425–1436 (1988).

[31] P. Mora, *Modeling anisotropic seismic waves in 3-D*, 59th Ann. Int. Mtg Exploration Geophysicists, expanded abstracts 1039–1043 (1989).

[32] P. Moczo, J. Kristek, V. Vavrycuk, R. J. Archuleta, and L. Halada, *3D Heterogeneous Staggered-Grid Finite-Difference Modeling of Seismic Motion with Volume Harmonic and Arithmetic Averaging of Elastic Moduli and Densities*, Bull. Seism. Soc. Am. **92**, 3042–3066 (2002).

[33] H. Igel, P. Mora, and B. Riollet, *Anisotropic wave propagation through finite-difference grids*, Geophysics **60**, 1203–1216 (1995).

[34] E. Tessmer, *3-D Seismic modelling of general material anisotropy in the presence of the free surface by a Chebyshev spectral method*, Geophys. J. Int. **121**, 557–575 (1995).

[35] O. C. Zienkiewicz and R. L. Taylor, *The Finite Element Method*, vol. 1. McGraw Hill, New York, 1989.

[36] E. Priolo, J. M. Carcione, and G. Seriani, *Numerical simulation of interface waves by high-order spectral modeling techniques*, J. acoust. Soc. Am. **95**, 681–693 (1994).

[37] G. Seriani, *3-D large-scale wave propagation modeling by a spectral-element method on a Cray T3E multiprocessor*, Comput. Methods Appl. Mech. Eng. **164**, 235–247 (1998).

[38] E. F. Toro, R. C. Millington, and L. A. M. Nejad, *Towards very high order Godunov schemes*, in *Godunov methods; Theory and applications*, E. F. Toro, ed., pp. 907–940. Kluwer Academic Plenum Publishers, Oxford, 2001. International Conference.

[39] V. A. Titarev and E. F. Toro, *ADER: Arbitrary high order Godunov approach*, J. Sci. Comput. **17**, 609–618 (2002).

[40] T. Schwartzkopff, C. D. Munz, and E. F. Toro, *ADER: A High-Order Approach for Linear Hyperbolic Systems in 2D*, J. Sci. Comput. **17**, 231–240 (2002).

[41] T. Schwartzkopff, M. Dumbser, and C. D. Munz, *Fast high order ADER schemes for linear hyperbolic equations*, J. Comput. Phys. **197**, 532–539 (2004).

[42] M. Dumbser and C. D. Munz, *ADER Discontinuous Galerkin Schemes for Aeroacoustics*, Comptes Rendus Mécanique **333**, 683–687 (2005).

[43] M. Dumbser and C. D. Munz, *Arbitrary High Order Discontinuous Galerkin Schemes*, in *Numerical Methods for Hyperbolic and Kinetic Problems*, S. Cordier, T. Goudon, M. Gutnic, and E. Sonnendrucker, eds., IRMA series in mathematics and theoretical physics, pp. 295–333. EMS Publishing House, 2005.

[44] J. de la Puente, *Seismic Wave Simulation for Complex Rheologies on Unstructured Meshes*. PhD thesis, LMU Munich, Department für Geo- und Umweltwissenschaften, 2008.

[45] K. Aki and P. G. Richards, *Quantitative Seismology*. University Science Books, 2002.

[46] A. Bedford and D. S. Drumheller, *Elastic Wave Propagation*. Wiley, 1994.

[47] B. Cockburn, G. E. Karniadakis, and C. W. Shu, *Discontinuous Galerkin Methods*. Lecture Notes in Computational Science and Engineering. Springer, 2000.

[48] R. LeVeque, *Finite Volume Methods for Hyperbolic Problems*. Cambridge University Press, Cambridge, 2002.

[49] E. Toro and V. Titarev, *Solution of the generalized Riemann problem for advection-reaction equations*, *Proc. Roy. Soc. London* 271–281 (2002).

[50] R. Courant, K. Friedrichs, and H. Lewy, *Über die partiellen Differenzialgleichungen der mathematischen Physik*, *Mathematische Annalen* **100**, 32–74 (1928).

[51] M. Dumbser, *Arbitrary High Order Schemes for the Solution of Hyperbolic Conservation Laws in Complex Domains*. PhD thesis, Universität Stuttgart, Institut für Aerodynamik und Gasdynamik, 2005.

[52] G. Karypis and V. Kumar, *Multilevel k-way partitioning scheme for irregular graphs*, *J. Parallel Distrib. Comput.* **48**, 96–129 (1998).

[53] J. Pujol, *Elastic wave propagation and generation in Seismology*. Cambridge University Press, Cambridge, UK, 2003.

[54] J. Kristek and P. Moczo, *On the accuracy of the finite-difference schemes: The 1d elastic problem*, *Bull. Seism. Soc. Am.* **96(6)**, 2398–2414 (2006).

[55] R. J. Geller and N. Takeuchi, *Optimally accurate second-order time-domain finite difference scheme for the elastic equation of motion: one-dimensional case*, Geophys. J. Int. **135**, 48–62 (1998).

[56] B. Fornberg, *The pseudospectral method: Comparisons with finite differences for the elastic wave equation*, vol. 52(4). Geophysics, 1975.

[57] J.-P. Ampuero and T. Nissen-Meyer, *High order conservative time schemes in spectral element methods for seismic wave propagation*, in preparation (2010).

[58] S. Day, J. Bielak, D. Dreger, R. Graves, S. Larsen, K. Olsen, and A. Pitarka, *Tests of 3D elastodynamic codes , Final report for Lifelines Project 1A02*, Tech. rep., Pacific Earthquake Engineering Research Center (2003).

[59] P. Goupillaud, A. Grossman, and J. Morlet, *Cycle-Octave and Related Transforms in Seismic Signal Analysis*, Geoexploration **23**, 85–102 (1984).

[60] M. Holschneider, *Wavelets: An Analysis Tool*, Oxford Science Publications (1995).

[61] M. Käser, P. Mai, and M. Dumbser, *On the accurate treatment of finite source rupture models using ADER-DG on tetrahedral meshes*, Bull. Seism. Soc. Am. **97(5)**, 1570–1586 (2007).

[62] R. Apsel and J. Luco, *On the Green's functions for a layered half-space, part II*, Bull. Seism. Soc. Am. **73**, 931–951 (1983).

[63] P. Moczo, E. Bystricky, J. Kristek, J. Carcione, and M. Bouchon, *Hybrid modeling of P-SV Seismic Motion at Inhomogeneous Viscoelastic Topographic Structures*, Bull. Seism. Soc. Am. **87**, 1305–1323 (1997).

[64] V. Hermann, M. Käser, and C. Castro, *Improved Flexibility and Efficiency of Seismic Wave Propagation Modeling using the Discontinuous Galerkin Scheme on Non-conforming Hybrid Meshes*, submitted.

[65] G. Karypis and V. Kumar, *Multilevel k-way partitioning scheme for irregular graphs*, J. Parallel Distrib. Comput. **48**, 96–129 (1998).

148

[66] M. Käser, V. Hermann, and J. de la Puente, *Quantitative Accuracy Analysis of the Discontinuous Galerkin Method for Seismic Wave Propagation*, Geophys. J. Int. **173(3)**, 990–999 (2008).

[67] Y. Capdeville and J. Marigo, *Shallow layer correction for Spectral Element like methods*, Geophys. J. Int. **172**, 1135–1150 (2008).

[68] E. Chaljub, P. Moczo, S. Tsuno, P.-Y. Bard, J. Kristek, M. Käser, M. Stupazzini, and M. Kristekova, *Quantitative Comparison of Four Numerical Predictions of 3D Ground Motion in the Grenoble Valley, France*, Bull. Seism. Soc. Am. **100 (4)**, 1427–1455 (2010).

[69] S. Abarbanel and D. Gottlieb, *A Mathematical Analysis of the PML Method*, J. Comput. Phys. **134**, 357–363 (1997).

[70] M. Kuzuoglu and R. Mittra, *Frequency dependence of the constitutive parameters of causal perfectly matched anisotropic absorbers*, IEEE Microwave and Guided Wave Letters **6(12)**, 447–449 (1996).

[71] W. Chew and W. Weedon, *A 3d perfectly matched medium from modified Maxwell's equaitons with stretched coordinated*, Microwave and Optical Tech. Lett. **7(13)**, 599–604 (1994).

[72] D. Komatitsch and J. Tromp, *A perfectly matched layer absorbing boundary condition for the second-order seismic wave equation*, Geophys. J. Int. **154**, 146–153 (2003).

[73] D. Komatitsch and R. Martin, *An unsplit convolutional perfectly matched layer improved at grazing incidence for the seismic wave equation*, Geophysics **72(5)**, 155–167 (2007).

[74] I. Laakso, S. Ilvonen, and T. Uusitupa, *Performance of convolutional PML absorbing boundary conditions in finite-difference time-domain SAR calcultaions*, Phys. Med. Biol. **52**, 7138–7192 (2007).

[75] R. Martin, D. Komatitsch, and A. Ezziani, *An unsplit convolutional perfectly matched layer improved at grazing incidence for seismic wave propagation in poroelastic media*, Geophysics **73(4)**, T51–T61 (2008).

[76] C. Marcinkovich and K. Olsen, *On the implementation of perfectly matched layers in a three-dimensional fourth-order velocity-stress finite difference scheme*, J. Geophys. Res. **108(B5)**, 2276 (2003).

149

[77] G. Festa, E. Delavaud, and J.-P. Vilotte, *Interaction between surface waves and absorbing boundaries for wave propagation in geological basins: 2D numerical simulations, Geophys. Research Letters* **32**, L20306 (2005).

[78] F. Hu, *A Stable, Perfectly Matched Layer for Linearized Euler Equations in Unsplit Physical Variables, J. Comput. Phys.* **173**, 455–480 (2001).

[79] A. Simone and S. Hestholm, *Instabilities in applying absorbing boundary conditions to high-order seismic modeling algorithms, Geophysics* **63(3)**, 1017–1023 (1997).

[80] H. Quasimov and S. Tsynkov, *Lacunae based stabilization of PMLs, J. Comput. Phys.* **227**, 7322–7345 (2008).

[81] M. Pischiutta, G. Cultrera, A. Caserta, and L. Luzi, *Topographic effects on the hill of Nocera Umbra, central Italy, Geophys. J. Int.* in press (2010).

[82] M. Bouchon and J. S. Barker, *Seismic response of a hill: the example of Tarzana, California, Bull. Seism. Soc. Am.* **86**, 66–72 (1996).

[83] B. L. Brun, D. Hatzfeld, and P. Y. Bard, *Experimental study of the ground motion on a large scale topographic hill at Kitherion (Greece), Journal of Seismology* **3(1)**, 1–15 (1999).

[84] P.-Y. Bard and B. E. Tucker, *Underground and ridge site effects: a comparison of observation and theory, Bull. Seism. Soc. Am.* **75(4)**, 905–922 (1985).

[85] L. Geli, P.-Y. Bard, and B. Jullien, *The effect of topography on earthquake ground motion: a review and new results, Bull. Seism. Soc. Am.* **78 (1)**, 42–63 (1988).

Acknowledgment

It's a great pleasure to thank those who contributed to the success of this work:

- Dr. Martin Käser, who provided me the interesting topic, brought in many expedient ideas and promoted the progressing of my work.

- Prof. Dr. Heiner Igel, who enabled me to pass my PhD thesis in his group and continuously made me think outside my own box.

- Dr. Josep de la Puente, Dr. Cristobal E. Castro and Christian Pelties for being me helpful enlighteners.

- Prof. Dr. Bettina Reichenbacher for coaching me as my mentor in the LMUexcellent Program.

- Prof. Dr. Valerian Bachtadse, who presented me a scientific view beyond my computer screen.

- Dr. Jens Oeser, Alex Hornung and Alex Fischl for the excellent IT-service and the coffee provision.

- Dr. Joachim Wassermann for providing the elevation dataset of Mt. Hochstaufen.

- My office mates Julia Linder, Annika Ferk, Florian Stark, Dr. Thomasz Gorka, Dr. Nguyen Dinh Pham, Dr. Josep de la Puente, Tobias Megies, Christian Pelties and Simon Stähler for inspiring conversations and the pleasant atmosphere.

- My colleagues for many interesting discussions and their efforts to help me with any problem I had. Amongst others I want to emphasize: Dr. Gilbert Brietzke, Dr. Andreas Fichtner, Dr. Marcus Mohr, Dr. Bernhard Schubert, Dr. Karin Sigloch and Dr. Michael Winkelhofer.

- Marion Bachhäubl, Yvonne Neßler, Amanda Steininger, Veronika Strachwitz and Veronika Weber from the secretary for taking over all the bureaucratic necessities.

- Günter Reichardt for encouraging me whenever I got stuck and for his belief in me.

- And last but not least my parents, who were backing me all the way, supported me unconditionally and who I always could rely on.

Traunstein, August 2010

Curriculum Vitae

Verena Kristina Hermann

Personal Information

Date of Birth	February 24, 1982
Place of Birth	Traunstein

Education

1988 - 1993	**Elementary School**, Volksschule Surberg
1993 - 2001	**High School**, Chiemgau-Gymnasium Traunstein
2001 - 2005	**Diploma Studies of Physics**, Universität Regensburg
08/2003	**Intermediate Diploma in Physics** (1.09), Universität Regensburg
2005 - 2006	**Diploma Thesis**, Karl-Franzens-Universität, Graz, Austria
10/2006	**Diploma in Physics**, Universität Regensburg
since 2007	**Ph.D. Student**, Ludwig-Maximilians-Universität (LMU), München

Professional Experience

1998 - 2002	**Internships in Management**, KATEK GmbH, Grassau
2002	**Conference Organization**, Deutsche Physikalische Gesellschaft, Regensburg
2003 - 2006	**Teaching Assistant in Physics**, Universität Regensburg
2005 - 2006	**Lectures on the Typographic Composition Program LaTeX**, Universität Regensburg
2007 - 2009	**Teaching Assistant in Geophysics**, LMU, München
2009 - 2010	**Expedition to Antarctica**, LMU, München